Anisotropic Magnetoresistance Magnetometer for inertial navigation systems

Kaveh Mohamadabadi

ECOLE POLYTECHNIQUE

Anisotropic Magnetoresistance Magnetometer for inertial navigation systems

by

Kaveh Mohamadabadi

A thesis submitted in partial fulfillment of the
degree of Doctor of Philosophy

Ecole Doctorale de l'Ecole Polytechnique

November 2013

Committe

Prof. Ing. Pavel RIPKA ..... Referee
Dr. Werner MAGNES ..... Referee
Prof. Hamid KOKABI ..... Examiner
Prof. Stephane FLAMENT ..... Examiner
Prof. Laurence REZEAU ..... Examiner
Dr. Yvan BONNASSIEUX ..... Examiner
Dr. Christophe COILLOIT ..... Supervisor
Dr. Mathieu HILLION ..... Co-supervisor

Kaveh MOHAMADABADI

Plasma Physics Laboratory (LPP), Ecole POLYTECHNIQUE,
Route de saclay,
F-91128 PALAISEAU CEDEX,
France.

SYSNAV,
57,
rue de Montigny,
27200 Vernon,
France

E-mail : kaveh.mohamadabadi@lpp.polytechnique.fr

Key words. - Vector magnetometer, anisotropic magnetoresistance magnetometer, cross-field error, flipping, magnetometer calibration, indoor magnetometer calibration system.

"If you can't explain it to a six year old, you don't understand it yourself."

Albert Einstein

ECOLE POLYTECHNIQUE

Abstract

Faculty Name
Ecole Doctorale de l'Ecole Polytechnique

Doctor of Philosophy

by **Kaveh Mohamadabadi**

This work addresses the relevant errors of the anisotropic magnetoresistance sensor for inertial navigation systems. The manuscript provides resulting guidelines and solution for using the AMR sensors in a robust and appropriate way relative to the applications. New methods also are proposed to improve the performance and, reduce the power requirements and cost design of the magnetometer. The new compensation method is proposed by developing an optimization algorithm. The necessity of the sensor calibration is shown and the source of the errors and compensating model are investigated. Two novel methods of indoor calibration are proposed and examples of operating systems are presented.

Acknowledgements

I would like to thank my supervisor and co-supervisor Dr. Christophe Coillot and Dr. Mathieu Hillion for their advice, guidance and support.
I would also like to thank Dr. David Vissire, CEO of SYSNAV, for his support and encouragement.

I would like to acknowledge the help of Dr. Antoine Rousseau for his support in the first year of my PhD program.

I owe my thanks to my colleagues in LPP and SYSNAV groups, specially Mr. Alexis Jeandet.

Finally, I am greatly thankful to my parents for their love and continued support throughout my life.

This work was sponsored by the CNRS (National Center for Scientific Research) and SYSNAV.

Contents

List of Figures

List of Tables

Dedicated to my parents...

Chapter 1

Introduction

For many years, travelers and sailors recognized that they needed more precise instruments for finding their position. Perhaps they used some landmarks for traveling from one point to others that they discovered before, but in the case of crossing the ocean and discovering new world, such could not be relied on. Therefore, they always has the desire to find an instrument or solution.

For these reasons, one of the most ancient sensors that have been used by the human is the magnetic sensor beyond any doubt. The magnetic compass was a vital instrument for sailors to navigate at sea and it was developed by the Chinese in the 11^{th} century and the Europeans in the 12^{th} [1] [2]. This navigation instrument was worked in any weather condition, anywhere in the world. However, the magnetic compass was only accurate as long as there were no additional magnetic influences and it aligned itself with the Earth's magnetic lines of force. Several years later, sailors discovered that the north direction indicated by the magnetic compass was usually not the same as the North Star. Although, today it is clear that the true North Pole and the magnetic north pole are not in the same place, at that time the size of declination was particularly large and it caused significant navigation errors [3].

Navigation was one of the main challenges facing scientists for several centuries, especially in the age of exploration, with the need to find more precise solutions and instruments. Although, by that time several good instruments had been built such as the compass, sextant, Persian astrolabe and octant, they were not accurate enough to navigate over long periods of time.

In 1957, the first spark of the notable invention of the 20th century was made by tracking a Russian satellite and measuring the Doppler effect of the signals that were received from it [4]. At that time the variation of the frequency of measured signals on one point on the Earth were used to identify the orbit of the satellite around the Earth.

Then, they used this effect to carry out reverse measurement using the orbit of the

satellite to detect an unknown point on the Earth [5], [6], [7]. After that, the United Stated Government spent tens of billion dollars to support and develop GPS in order to use for military purposes.
The primary concept of GPS included by 21 operational satellites and three as spares. It took 17 years from launch to the first satellite becoming an operational system. These satellites are placed into a very precise orbit, approximately 20,200 Km from the Earth's surface, and they orbit around the Earth every 12 hours at speed of 11.500 Km/h. To identify any position, the GPS receiver needs signal reception from at least four GPS satellites, and then it computes the exact position of each satellite and the delay time of the signal traveling from the satellite to the receiver. It is clear today that GPS provides various facilities and safety for human life and it has been successfully integrated into many military and civilian applications. However, this space-based navigation system suffers from some drawbacks. The main weakness of GPS is its inability to transfer signals and navigate in an indoor area. Moreover, in an open-door area some sources of error also exist, such as signal multipath that happens by reflection from tall building or any other large objects; atmospheric disturbances that distort the GPS signals among the satellites and receivers; errors of receiver clock when it is not synchronized with the atomic clock of satellites, etc.
Using an inertial navigation system (INS) as a backup solution has been considered for several years. The INS is based on the universal laws of motion that were expressed by Isaac Newton. These laws illustrate the exact relation between an object's mass, its acceleration and the applied force.
Before the Second World War, several inertial navigation systems were built, but at that time the performances of the inertial sensors were not good enough to implement them in a system. During the Second World War, the German scientists developed an inertial guidance system for the rockets. Very soon after, the competition started in order to improve the sensor performances and develop a new type of system.
The INS contains accelerometers and gyroscopes to continuously calculate the position and orientation of an object from a known initial point. They have several significant advantages over other navigation systems, such as independence from any external aids or data, ability to operate in any indoor area such as tunnels, buildings, etc. The main disadvantages of these kinds of systems are:

- Size and weight
- Power requirements
- Heat dissipation
- Cost

In general, inertial navigation systems can be divided into two categories: stable platform systems and strapdown systems. However, they are both based on the same principles. *Stable platform systems* consist of inertial sensors such as accelerometer and gyroscope that are mounted on the same platform. The accelerometers data are used solely to estimate the position and velocity. In parallel, the gyroscopes are used to detect any external forces that may cause the platform to rotate. This measurement is used to maintain the platform position at the correct attitude compared to the global frame. To achieve this aim, the stable platform systems incorporate gimbals and torque motors, to rotate the platform base on the correction signals sent by the gyroscopes. Figure 1.1 shows a model of a stable platform.

Strapdown systems also consist of combination of accelerometers and gyroscopes. How-

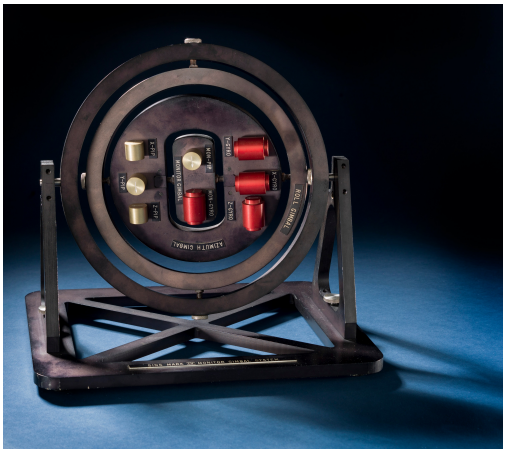

FIGURE 1.1: Model of Ship's Inertial Navigation stable platform made by Charles Stark Draper Laboratories.

ever, in this case there are no rotating parts and motors. For strapdown systems, the rigid body frame is used to estimate the position. Consequently, the orientation data provided by the gyroscopes should be integrated directly into the computation. Strapdown systems reduce the cost, mechanical complexity and size. However, the computation is more costly than that of stable platform systems.

Recently, MEMS (Micro electro mechanical system) technology has been developed very quickly and merged with many other technologies and applications. This revolution has resulted in the fabrication of a high volumes of low-cost sensors such as accelerometers, gyro and magnetometers with acceptable performance, power consumption, size, weight, etc. The results of these changes are well-known to everybody simply through the use of smartphones. As a result, nowadays, strapdown technology has become dominant compared to the stable platform for inertial navigation systems.

For this reason, today any modern navigation system utilizes a combination of GPS and INS technology to improve performance. In this case, an INS can function alone when

the GPS signal is not available.
Generally, as stated earlier, the INS contains inertial sensors such as accelerometers and gyroscopes. However, with low-cost sensors, drift and error are too high and additional sensors have to be added to reduce errors. Magnetometers, barometers and temperature sensors can be mentioned as examples of such.
The main aim of using a magnetic sensor in INS is as a magnetic compass for heading. In this case, when the magnetic sensors are leveled in a horizontal plane compared to the Earth's gravity vector (roll and pitch angles equal zero), heading is defined as:

$$heading = \arctan(\frac{H_y}{H_x}) + \delta \tag{1.1}$$

Where H_x and H_y are two orthogonal components of the magnetic field vector that is measured by a two-axis magnetometer. In addition, δ is the declination angle that represents the difference between true and magnetic north.
Moreover, in such a high performance navigation system, these sensors can be used in a different way to measure the gradient of the magnetic field. This gradient can then be used to estimate the velocity and to compensate the accelerometers errors [8] [9]. In this case, considering Equation (1.2), the variation of the sensed field that may be caused by device movement can be used to calculate the velocity.

$$\frac{dB(x(t))}{dt} = \frac{dB(x(t))}{dx}\frac{dx(t)}{dt} \tag{1.2}$$

where $\frac{dB(x(t))}{dt}$ represents the variation of the magnetic field in time due to the movement, $\frac{dB}{dx}(x(t))$ illustrates the gradient of the magnetic field among at least two sensors and, finally, the velocity of the rigid body can be found by computing $\frac{dx(t)}{dt}$. Note that, this type of system is known as Magneto-inertial Navigation system (MINAV) [10] [9].
Considering this new approach, it is desirable to take a deeper look at the magnetic sensors and their performances. Our focus in this thesis is on low-cost available magnetometer and methods to calibrate and improve the sensor performances.

Thesis organization

This thesis contains seven chapters and two appendices.
Chapter 2 reviews the vector magnetometers that have the potential to measure the Earth's magnetic field for such low-cost modern navigation systems. Our aim in this chapter is to deal with the principle and performances of the available magnetometers. They are discussed in terms of advantages, disadvantages and applications.
Chapter 3 describes the principle of anisotropic magnetoresistance (AMR) sensors

selected for inertial navigation systems in detail. This chapter continues with more advanced explanations of their typical errors to detect the Earth's magnetic field. In addition, in this chapter the solutions and techniques are investigated with theoretical and experimental results to reduce the error reading of the AMR sensors.

Chapter 4 deals with error modeling of three axis magnetometer in a typical inertial navigation system. The errors such as scale factors, misalignment, soft and hard iron effect will be discussed in this chapter. Meanwhile, the solutions for compensating and calibrating the magnetometers are proposed.

Chapter 5 addresses the cross-axis effect (or error) problem in three-axis AMR magnetic sensors. This chapter focuses on magnetometer calibration in the Earth's magnetic field for low-cost sensors. We propose a self-consistent and practical method based on the cross-axis effect modeling, to compensate this error without using any high precision magnetic sensors for comparing the results. This method does not depend on other instruments to provide and measure the magnetic field. The compensation method is implemented in two configurations: direct amplification of an AMR signal and magnetization flipping.

Chapter 6 presents two novel methods for indoor calibration purposes. The first method can be used for all three axis vector magnetometers by using the three-dimensional Helmholtz coil. In this method, in order to use the calibration algorithm instead of rotating the sensor in a constant magnetic field vector, the vector of magnetic field rotates around the magnetometer. The results of this calibration method will be compared with the classical scalar calibration method in the Earth's magnetic field as well. We also present evidence that the magnetometer does not need to align with the Helmholtz coil axis; instead, it can be calibrated with any arbitrary direction of the Helmholtz coil. Furthermore, the second indoor calibration method is limited for AMR sensors. The implemented circuit is designed to calibrate AMR sensors using integrated coils. We show the similarity of the results for residual calibration norm by using this method compared with the calibration of the sensor in a free perturbation of Earth's magnetic field. Meanwhile, this method does not require any other instruments, such as Helmholtz coils or a platform for rotating the sensor.

Chapter 7 contains the conclusion.

Chapter 2

Review of magnetic sensors

Recently, magnetic sensors have come to play a key role in many applications. They permeate more and more of our life and work in nearly all engineering and industrial sectors. Thanks to several decades of research, today, the diversity of magnetic sensors give us the ability to measure a wide range of magnetic fields at levels even below several tens of femtotesla. There is a high dependency on magnetic sensors in new technologies, such as military, security, magnetic recording, space research, navigation, bio-medical, geometric measurement, car industry, cell phones, etc.

Magnetic sensors can be sorted into three basic categories: high sensitivity; medium sensitivity and low sensitivity[11]. High sensitivity are those that are able to measure magnetic fields lower than nanotesla level. Low sensitivity are those that are appropriate for detecting magnetic fields greater than tens of millitesla. Finally, the boundaries of these two categories are allocated to those that are appropriate for measuring the medium range of magnetic field. Apart from this, magnetic sensors can also be split into two other main groups: scalar and vector magnetic sensors. Scalar magnetic sensors are those that measure the total magnitude of the field and vector magnetic sensors measure the magnitude of the field only in their sensitive direction.

In a chapter of this length, it is not possible to cover all the magnetic sensors and relative applications. Our aim is to focus on the vector magnetic sensors that can be used to measure the Earth's magnetic field for such modern navigation systems. However, some recently developed sensors can perform out of their ordinary range. For instance, although the Hall sensor is dedicated to the low sensitive magnetic sensor, it can also reach the resolution of the medium sensitivity group.

Several articles and books have been published for different types of magnetic sensors. In general, books such as [12] and [13] cover almost all types of magnetic sensors (except for some modern ones). Magnetoresistance sensors such as AMR and GMR have been well described in [14] and GMI in [15], [16] and [17]. Hall effect sensors have also been

explained in [18]. Note that our review of the magnetic sensor is based mainly on these mentioned references.

2.1 Hall sensors

Hall sensors are the magnetic sensor most widely used nowadays in several applications. The car industry is a heavy user of Hall magnetic sensors for such applications as anti-lock braking systems (ABS), wheel speed, crankshaft, etc.
The Hall Effect was discovered by Edwin Hall in 1879 while he was a doctoral candidate. Hall sensors work on the basis of Lorentz force. In this case, when a current-carrying conductor is exposed to the magnetic field density, a Lorentz force deviates electrons from their initial directions and creates a voltage as output (see Figure 2.1). However,

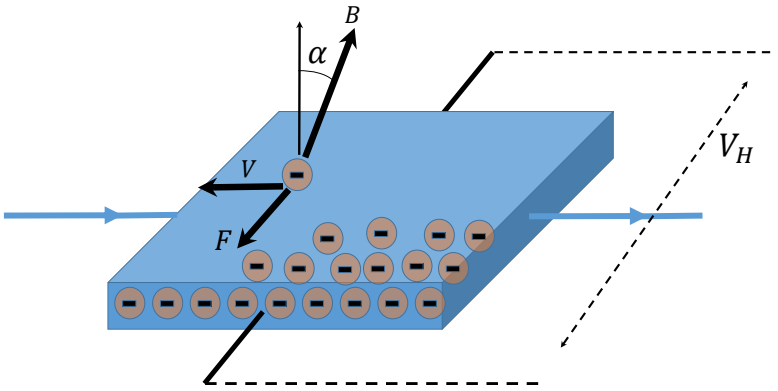

FIGURE 2.1: Schematic of thin wafer of Hall effect sensor.

this voltage is a low-level signal, and it needs to be equipped with a low noise electronic design to amplify the signal. Equation (2.1) presents the proportionality of this voltage to the other parameters:

$$V_H = \frac{R_H}{t}.I.B\cos\alpha \tag{2.1}$$

Where R_H is the Hall coefficient, I is the current passing through the strip, t is the thickness of the strip and $B\cos\alpha$ is the perpendicular component of the magnetic field intensity.
The sensitivity of Hall sensors is dependent on the mobility of electrons which can be given by Equation (2.2).

$$E_H = -\mu_{Hn}[E_e \times B] = -R_H[J \times B] \tag{2.2}$$

Where E_e is an external electrical field, B is the magnetic flux density, E_H is the Hall electric field, J is the current density and μ_{Hn} is the Hall mobility of electrons. The frequency limitation of Hall Effect sensor is about 1Mhz [11] and their resolution can be extended to several hundred micro Gauss. However, using a technique known as magnetic field amplification, can improve the Hall sensor sensitivity to close to 200 pT [19].

2.2 Search coil

Induction coils or search coils are based on Faradays law of induction. Any variation of the magnetic flux environment of a coiled conductor will cause a voltage. Generally, in order to improve the search coil performances, a rod of ferromagnetic material that so called core is used inside the coil. Sometimes this effect is called magnetic amplification. Since the coil has a high permeability material, the surrounding magnetic fields are concentrated through the core and the senor provides more signals. Moreover, as depicted in Figure 2.2, some methods proposed using additional flux concentrators to increase the magnetic amplification inside the coil [20].

The frequency response of the search coil magnetometer may be limited by the ratio of

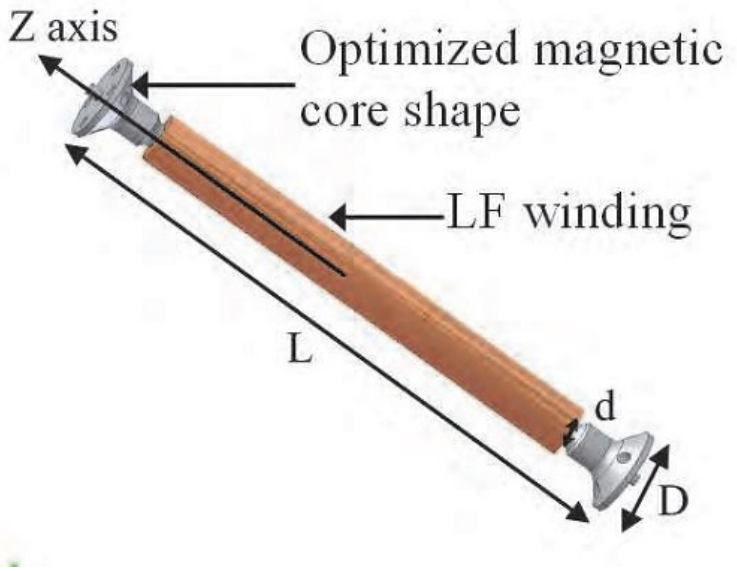

FIGURE 2.2: Ferromagnetic core using flux concentrator.

the inductance of the winding coil to its resistance. In addition, the sensitivity depends on the turn number of winding coils, the dimensions of the coil and the permeability

of the core material. The induced voltage of a search coil can be expressed by Equation (2.3).

$$V = -NS\mu_e(\frac{dB}{dt}) \tag{2.3}$$

where S is the cross-sectional area of the core, N is number of turns, μ_e is the permeability of the core, and $\frac{dB}{dt}$ represents the time variation of the magnetic field along the sensitive direction of the sensor.

Because of the winding coil, a capacitance exists between the conductors that causes a resonance on the sensor output. This resonance can be considered a drawback, as it saturates the output of electronics and limits the frequency response. Due to this effect, depending on application, feedback flux can be used to suppress the resonance of the search coil magnetometer. Finally, apart from the search coil's size, these sensors can be used in numerous applications due to their wide sensitivity range and frequency response, from 1Hz to 1Mhz. However, the sensitivity is reduced by decreasing the frequency, and even by using the integrator the DC magnetic field can not be measured.

2.3 Flux-gate

Flux-gate sensors measure weak magnetic fields in the range of 0.01nT to 1mT and they are the most widely used sensor for navigation systems. The most common type of flux-gate magnetometer is called the second harmonic device. This flux-gate magnetometer is based on using two coils around a common high permeability ferromagnetic core. A premagnetization winding or excitation coil produces an alternative field in order periodically to saturate the core of the flux-gate and then a pick-up winding or sensing coil is used to measure an external magnetic field. (see Figure 2.3)

In the absence of the external field, the sensor reading only relates to the magnetic field induced by the excitation coil at a frequency of f. To be more precise, the sensor output is a voltage that corresponds to the sum of different odd harmonics of the excitation frequency. Once the external field is applied, the even harmonics are added to the sensor reading as well (pick-up coil). Thus, the amplitude of these even harmonics can be used to identify the intensity of the external magnetic field.

The frequency responses of the flux-gate magnetometers are limited by the excitation field that is provided by the excitation coil and the response time of the ferromagnetic material. Their operating frequency is limited to a range from DC field measurement to about a few tens of kHz.

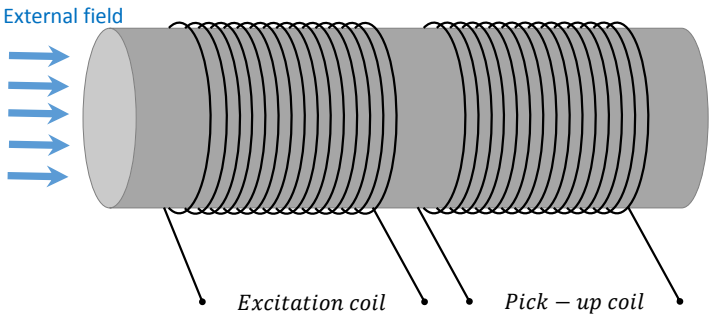

FIGURE 2.3: Basic configuration of a flux-gate magnetometer.

However, the flux-gate magnetometers are basically big because of the large ferromagnetic materials, and they suffer from a limited operating range and high power requirement. Due to this, recently several efforts have been made to miniaturize the flux-gate sensor for the sake of reducing the size, weight, cost and power consumption [21]. This type of flux-gate sensor can be considered comparable (in term of resolution, size and power consumption) to anisotropic magnetoresistance (AMR) sensors.

2.4 Magnetoresistance and Magnetoimpedance magnetometer

2.4.1 AMR

The principle and functionality of AMR (anisotropic magnetoresistance) sensor will be detailed in the next chapter. Here, we limit ourselves to presenting some advantages of this type of magnetometer. AMR magnetometers have a simple fabrication process regarding the number of layers and materials used. They are widely available nowadays and several companies participate in this segment, such as Honeywell, Philips, Sensitec, Memsic, etc. Compared to other magnetometers, AMR sensors are also the most stable magnetoresistance sensor in term of bias and sensitivity. Because of MEMS technologies, triple axes of this type of sensor are available in a tiny package. These are the reasons that AMR sensors are still mostly used for low-cost inertial navigation systems.

2.4.2 GMR and TMR

GMR

Gain Magneto Resistance (GMR) was discovered in 1980s [22]. This phenomenon is based on the principle of spin dependent scattering. The most frequently used type of GMR is a spin-valve sensor that exhibits magnetoresistance of 8-20%. The simple spin-valve GMR structure contains four-layers with different specifications (see Figure 2.4). Two layers of ferromagnetic thin layer material are separated by conducting non-ferromagnetic interlayer. The forth layer is an antiferromagnetic field that is used to pin the magnetization of the ferromagnetic layers. The main key point of GMR performances is the thickness of the layers. This thickness causes different electrical resistance as a functionality of external magnetic field.

Typically, the layers should be thinner than the mean free path of the electrons (less

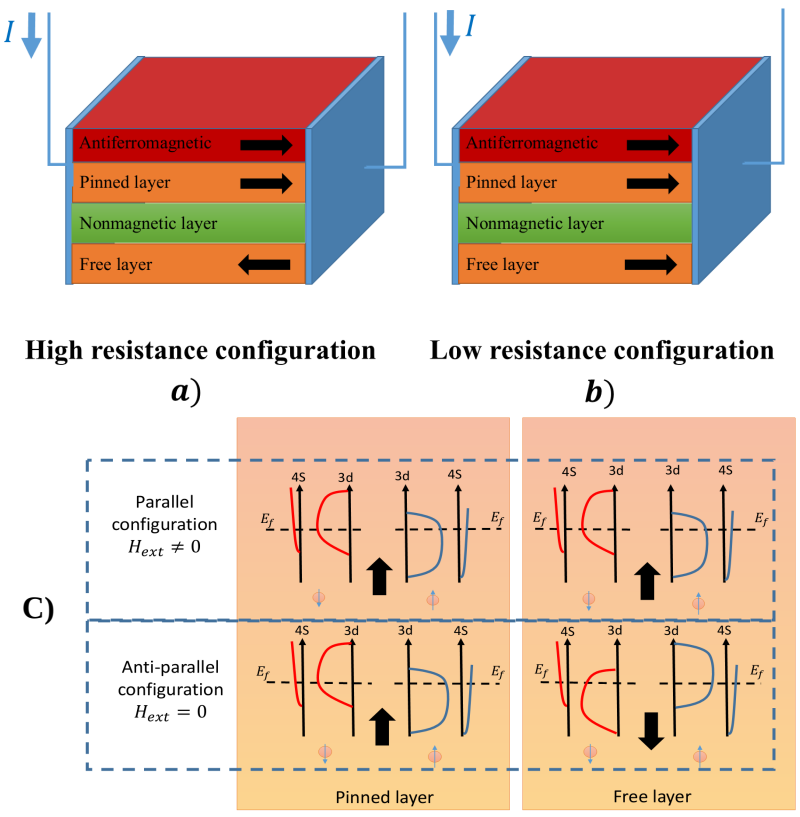

FIGURE 2.4: Spin-Valve GMR resistivity effect: a) anti-parallel layer moment, b) parallel layer moment.

than 10nm). The antiferromagnetic layer of GMR structure is used to fix the magnetization direction of one of the ferromagnetic layers that is called the pinned layer. In contrast, the highly conducting nonmagnetic layer separates the other ferromagnetic layer that is called the free layer. Then, by assuming that the magnetic moment of the

pinned layer is fixed with the help of the antiferromagnetic layer, the magnetic moments of the free layer only change with the external magnetic field. Figure 2.4 (c) depicts a schematic illustration of the density of electron states in two ferromagnetic layers. Here the current contains spin down and spin up elements and as a consequence of the ferromagnetic material the density of states at the Fermi level is asymmetric. Meanwhile, assuming that the spin down electrons are scattered more strongly than the spin up electrons. In this case, when the magnetization of the two ferromagnetic layers is in an aligned state the spin down electrons as mentioned are scattered in both ferromagnetic layers and the spin up electrons can pass from one ferromagnetic layer to another almost without scattering. Therefore, the total resistance of the multilayer appears to be low (Figure 2.4 (c) top).
In contrary, in the absence of the external magnetic field, the two ferromagnetic layers have antiparallel magnetization direction. In this case, both spin up and down electrons are scattered with one of the ferromagnetic layers and then the total resistance appears to be high. (Figure 2.4 (c) bottom).
The GMR sensor can provide high sensitivity and temperature stability. However, the sensor output is basically unipolar and they have a hysteresis. They can also be destroyed easily in a strong magnetic field.

TMR

Tunneling Magnetoresistance (TMR) has a similar structure to the spin valve GMR sensors. They also consist of two ferromagnetic layers separated by an ultra-thin interlayer. An antiferromagnetic layer also helps to hold the magnetization of the adjacent ferromagnetic layer fixed in direction. (see Figure 2.5)
However, compared to the GMR sensor, there are two main differences. First, the ultra-thin insulating metal oxide material (also called tunnel barrier), is replaced between the ferromagnetic layers. Second, in the TMR sensor electrons pass from one layer to the other through the insulator layer. This is also why this sensor is called tunneling magnetoresistance, because of the behavior of electrons when they can apparently pass across some sort of a barrier.
The resistance of TMR sensor changes in a manner similar to what we have discussed for GMR sensors due to the spin-valve effect. In the absence of an external magnetic field, the two ferromagnetic layers have anti-parallel magnetization. This configuration causes low tunneling probability and consequently a higher resistance value for TMR sensor. In contrast, parallel magnetization leads to a higher tunneling probability and lower resistance for TMR sensor.

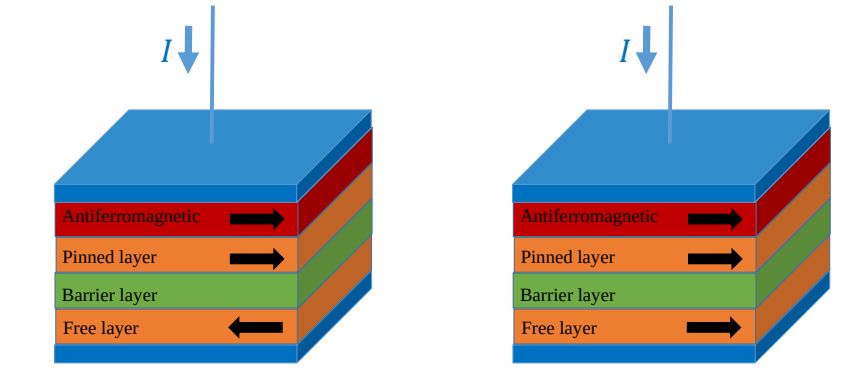

High resistance configuration

a)

Low resistance configuration

b)

FIGURE 2.5: TMR sensor structure.

In this case the change in resistance over the TMR junction can be expressed by Equation (2.4).

$$\Delta R = \frac{TRA}{2Wh} cos\alpha \tag{2.4}$$

Where $T = (R_{max} - R_{min})/R_{min}$ is the TMR ratio, R is the sensor resistance, A is the aria of the junction, h and W are the sensor height and width respectively and α is the angle between the magnetization vectors of free layer and pinned layer.
The TMR magnetic sensors are much more sensitive than GMR sensors and they have a big resistance element. The MR ratio ($\Delta R/R$) of TMR sensor is very high compared to any other MR sensors. This type of sensor with its high output signals allows for sampling without additional amplifiers, which also leads to a reduction in the power consumption, noise and improves the sensor resolution. However, it has drawbacks such as hysteresis and manufacturing complexity.

2.4.3 GMI

Giant magnetoimpedence (GMI) sensors provide a strong dependence of the impedance of a conductor on the external magnetic field. Compared to other magnetoresistance sensors, GMI can be described by a simple impedance element (see Figure 2.6). A soft ferromagnetic conductor plays a role as a complex impedance when a high frequency AC current is driven through it. This impedance can be defined as $Z = R + j\omega L$, where R, ω and L are respectively resistance, AC current frequency and inductance. In addition, this alternating current causes the skin depth on the conductor and then the current is restricted to flow over a small thickness of the conductor.

In the presence of an external magnetic field, the transverse permeability of the soft

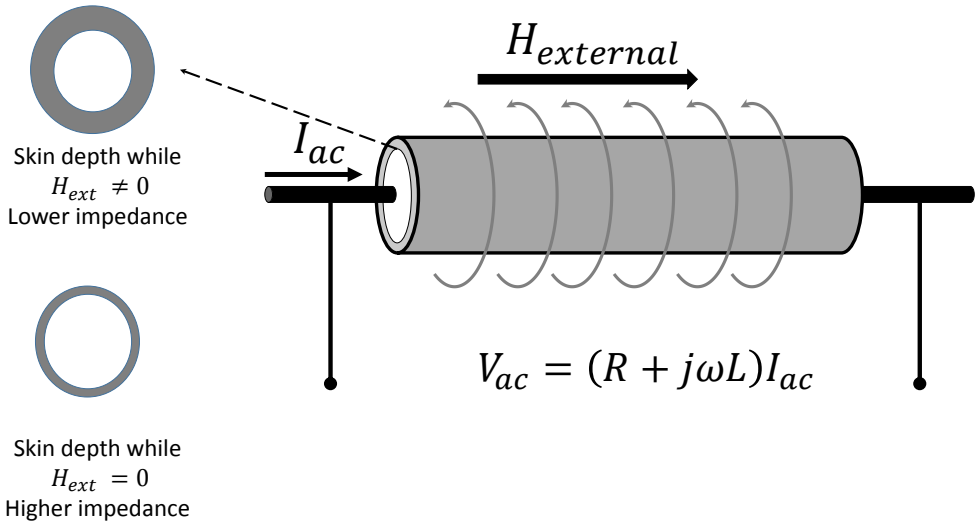

FIGURE 2.6: Schematic of GMI sensor.

ferromagnetic material changes and will modify then the impedance by changing the skin depth. Typically, the range of excitation frequency of AC current can vary from several tens of kHz to several Mhz.

In term of magnetic field resolution, GMI sensors can be considered a competitor of the flux-gate sensor. However, they do not need the exciting and sensing coils. Moreover, the sensor output is unipolar and has hysteresis error as well. Although, it should be noted that in some cases an auxiliary coil can be used to improve the linearity response of the sensor or for alternative biasing [23] [24].

2.5 Magneto-Electric sensor

The magneto-electric (ME) effect was first introduced by Pierre Curie in 1894. Basically, the magneto-electric effect is characterized by the appearance of an electric polarization to an applied magnetic field or by the appearance of a magnetization to an applied electric field [25].

The magneto-electric effect can occur in single phase material or in composite materials with several layers to improve the sensor sensitivity. Figure 2.7 shows a typical prototype of magnetostrictive/piezoelectric composite sensor. A simple structure of this type of sensor would consist of an inner layer of piezoelectric material sandwiched by two magnetostrictive layers. In this case, when an AC magnetic field is applied along the longitudinal direction, magnetostrictive layers are excited. Consequently, because the layers are stress coupled, the piezoelectric layer is excited as well and then a voltage is induced on the two faces of the piezoelectric layer. Meanwhile, when a DC magnetic field is applied, a ME sample creates an electric field as a function of the applied field.

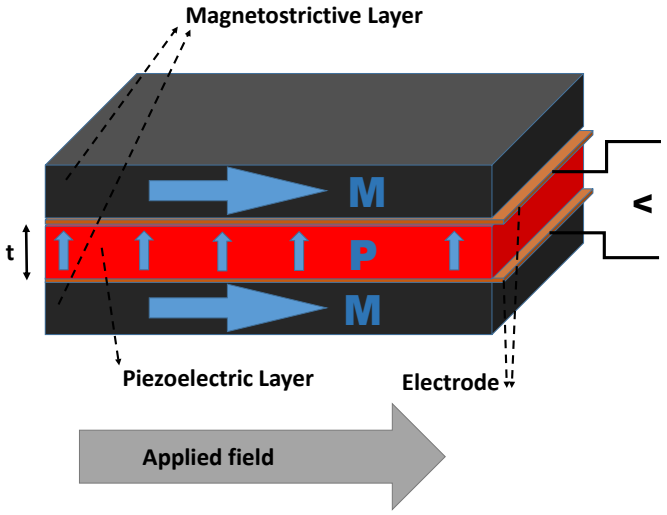

FIGURE 2.7: Schematic diagram of magneto-electric sensing element.

Equation (2.5) represents an induced electric field (E) in response to an applied magnetic field (H_{dc}) where α_E is a ME field coefficient.

$$E = \alpha_E . H_{dc} \tag{2.5}$$

Moreover, the induced electric voltage that appears between the surfaces of the piezoelectric layer with a thickness of t can be written as follows:

$$V_{ME} = tE = \alpha_E t H_{dc} \tag{2.6}$$

In order to detect the DC magnetic field with a magneto-electric sensor and improve the sensor sensitivity an AC magnetic field ($h_{ac} = h_0 sin(2\pi f_0 t)$) is needed to excite the materials into vibration along its length axis. This AC magnetic field is generally driven by an auxiliary coil. Then, small variations in the DC field can be detected by induced voltage due to the magneto-electric coupling.
The magnetic sensor based on ME effect have several advantages such as small size, simple structure and low cost. They can also have an equivalent input magnetic noise as low as 10^{-15}Tesla/$\sqrt{Hz}$ at 78kHz for detecting the AC field at room temperature [26].

2.6 Application

In this part, most of the common magnetic sensors that can be a candidate for the navigation applications have been described in brief. Using magnetic sensors for different navigation applications always require a trade-off between sensitivity, accuracy, linearity

response, size, power requirement and cost. In other words, using the advantage of one sensor may lead to the loss of the other advantages that can be achieved by using other sensors. For instance, where the cost is not a concern, the flux-gate magnetometers can be replaced with magnetoresistance sensors. In other cases, if the power consumption needs to be lower, the GMI sensors can be employed.

As stated in the previous chapter the magneto-inertial navigation systems use the combination of magnetometers to estimate the heading and velocity of rigid body. The second estimation can be performed by measuring the gradient of the magnetic field. The typical prototype of this system developed by SYSNAV uses five magnetometers in a 10 cm by 10 cm square (4 in the corners and one in the center of the board). Meanwhile, the magnetometer that we are seeking should have a resolution of less than 200 μG, low power requirement, small size and be stable in terms of bias and sensitivity after the calibration.

Originally, Hall sensors had a low sensitivity. However, recently, by using better material properties, they have achieved better performances. These kinds of sensors can also be used as an electronic compass with heading errors lower than 1° [27]. Apart from sensitivity, other significant weak points of these sensors is the zero offset. The spinning current technique can be used to compensate this error. In this case, the output current is measured separately for each current direction and then the averaged signal is used to detect the applied field. Today, some of the commercially-available of these sensors (CSA-1VG from GMW) can be found with a linear range of 7mT, non-linearity of 0.2 % and offset temperature drift of 0.2 mV/°C.

Their power consumption is between 100 and 200 mW. Hall sensors are very cheap and they can operate over an extremely wide temperature range [28]. They have also been used in several low cost position sensor applications, such as mobile phones and wrist watches.

Flux-gate magnetometers are popular devices for navigation applications such as aircraft [29], vehicles [30] and submarines. They are also a suitable instrument for space research [31] and to detect ferromagnetic objects [32]. They provide better resolution than MR sensors. However, they have an upper cut-off frequency response of a few Hz to a kHz. Moreover, in order to increase the precision and stability of the fluxgate sensors, a magnetic field feedback should be used instead of open loop structure. In this case, the linearity error can be as low as 10^{-5}. The temperature stabilities of the fluxgate sensors can be around 0.1nT/°C for the offset drift [21]. Although, they are suitable for the application regardless of size, cost and power consumption that is not usually the case for the low cost strapdown technologies. As stated earlier, several efforts have already been made in order to reduce the size and power consumption by implementing the coils and complex construction of the core within planar technologies (PCB and CMOS technology). However, this process usually brings many difficulties and causes

to reduce the sensor sensitivity [33].

The search coil is one of the oldest magnetometer that still used widely in many applications. The search coil can detect a magnetic field as weak as 20 ft. Their operating frequency range is typically from 1 Hz to 1MHz. Meanwhile, there is no upper limit to their sensitivity range. Their power requirement can be limited to between 1 and 10mW, even with the readout electronics in the passive mode [11]. Perhaps one of the main advantages of this type of sensor is that they can be fabricated directly by the users. Nevertheless, the search coil signal will appear if it is either in a varying magnetic field or moving through a constant magnetic field. As a result, they are not appropriate for navigation application. The search coils are well-known for applications such as space research [34] [35], eye motion tracking [36] [37], and so on.

The magneto-electric sensors are introduced as extremely low power and high sensitive magnetometers that can operate at room temperature. Their sensitivity for detecting the DC magnetic field can reach to several tens of picotesla and they have a wide range of magnetic field measurement [38]. The ME coefficient of this type of sensor has been reported to several hundreds of mV/cm/Oe at room temperature [39]. They have mostly been developed in recent years by discovering new materials and structures. However, they are not yet widely available. The main drawback that can be noted for these type of sensors is their poor accuracy in detecting a weak DC and low frequency AC magnetic fields [40] [38].

The GMI sensors have the same sensitivity and measurement range as the currently used fluxgate. However, they do not have an excitation coil. Moreover, they can have smaller size and lower power compensation than the fluxgate magnetometer. They are able to measure the magnetic field resolution of 100pt/ at 1 Hz [41]. Their power requirement is comparable to the magnetoresistance sensors such as AMR and GMR. The main drawbacks of the GMI sensors are hysteresis, size (compared to MR sensors) and perming effect due to their core.

The GMI sensors can be used in various applications such as space research, electronic compass [42], biological detection [43][44], etc.

So far, the GMR sensors have mostly been used in read heads for magnetic hard disk drivers [45]. Their power requirement is lower than the AMR sensors; however, they have more sensitivity. Although, in contrast to AMR sensors, the GMR sensors have more hysteresis and nonlinearity [46]. Moreover, compared to the AMR sensors, they have also a poor signal to noise ratio at low frequencies. The best utilization of GMR sensors is in a full Wheatstone bridge configuration to improve the signal level and linearity of the sensor. Today, some of these sensors are available with maximum Non-linearity of 2 % in a linear range of 10 Oe and hysteresis of 4 % [47]. Meanwhile, after the Hall sensors they are the cheaper sensor in our sensor group.

The TMR magnetometers are predicted to be the most interesting candidate among

other MR sensors. They are still under development and are not at present widely available. As mentioned, their power consumption is extremely low as a consequence of the sensor resistance (typically 1MΩ). Moreover, their signal output can be much higher than the other magnetic sensors [48] [49] (reported 200% for MR ratio). As a result, the read-out electronic cost can also be reduced by eliminating the amplification part. The TMR barrier resistance also estimated to be very stable over the time [50]. The TMR sensors offer these significant advantages with a very low cost technology. Recently, these sensors were priced by NVE Corp at 2$ each in 1000 quantities [51]. The disadvantage of the TMR sensors compared to the AMR is the hysteresis and commercial availability. To sum up we believe that the AMR sensors still have a priority to be selected for the low cost strapdown navigation system. They can provide resolution of 0.1 degrees, which is enough for almost all the navigation applications in the Earth's magnetic field. They are available in various packaging options for prices lower than 10$ for three-axis sensors. Most of modern AMR sensors are also equipped with two different internal coils to ensure robust performances in terms of bias and sensitivity over time. Meanwhile, they can be calibrated on-board by using these internal coils. Today some of the AMR sensors are available with the ASIC integrated for reducing the front-end electronic size and cost. Moreover, this kind of AMR sensor can be more reliable for use in space applications and they show a high robustness for total irradiation dose (TID) of up to 200 krad [52]. Their power requirement can be limited to between 10mW and 40mW for the normal operation.

Table 2.1 below presents the comparison of these magnetic sensors.

Type	Sensitivity	Size	Power consumption	Advantage	Disadvantage	Cost
Hall	$Medium - low$	μm	*Medium*	*Linear*	*Low sensitivity*	*Very low*
Search coil	$Very\ high$	cm	*Very low*	*Wide range*	*Size – feedback field – time dependent magnetic field*	*Medium*
Flux-gate	$High$	cm	*High*	*Robustness*	*Size-power requirement*	*High*
GMR	$High$	μm	*Low*	*Small size*	*Low frequency noise-hysteresis*	*Low*
TMR	$High$	μm	*Low*	*Very high MR ratio*	*Hysteresis*	*Low*
AMR	$medium$	μm - cm	*Medium*	*Stability of bias and sensitivity*		*Low*
GMI	$High$	cm	*Low*		*Hysteresis - size*	*Low*
ME	$Very\ high$	mm - cm	*Very low*	*Wide range – Small size -*	*Poor accuracy for measuring weak magnetic field*	*Very low*

TABLE 2.1: Different characterization of magnetometers.

Chapter 3

Anisotropic Magnetoresistance Sensor

3.1 Principle

In 1857, William Thomson (or Lord Kelvin) published a paper entitled "Effect of magnetization on the electric conductivity of nickel and iron". He claimed that the changes of resistance were different in direction compared to the magnetizing field direction and, because of that, this effect has been called anisotropic magnetoresistance (AMR). However, this discovery had to wait more than 100 years before thin film technology could make a practical sensor for application use. AMR sensors are made of nickel-iron or permalloy material in a thin film layer shape. This layer has a magnetization vector in a specific direction and it rotates when an external field is applied to the layer. Therefore, depending on the external field direction and its magnitude, the magnetization vector deviates by an angle. This magnetization vector is created by applying a strong magnetic field along the strip's length to magnetize it, and then as depicted in Figure 3.1 (a) all the magnetic domains in the permalloy layer align together in a unique direction. This alignment will theoretically cause a change in the state of the magnetic domains in the thin film material to a single domain state [53], [14].
In addition, as has been shown in Figure 3.1 (b), the sensor output depends on the angle (φ) between the magnetization vector ($\overrightarrow{M}$) and the anisotropy or easy axis direction. The external magnetic field ($\overrightarrow{H}$) surrounding the sensor, modifies this angle by rotating the magnetization vector.

Now, in order to find the relation between the angle and the external magnetic field, we should refer to the magnetic energy in a ferromagnetic layer by considering the single

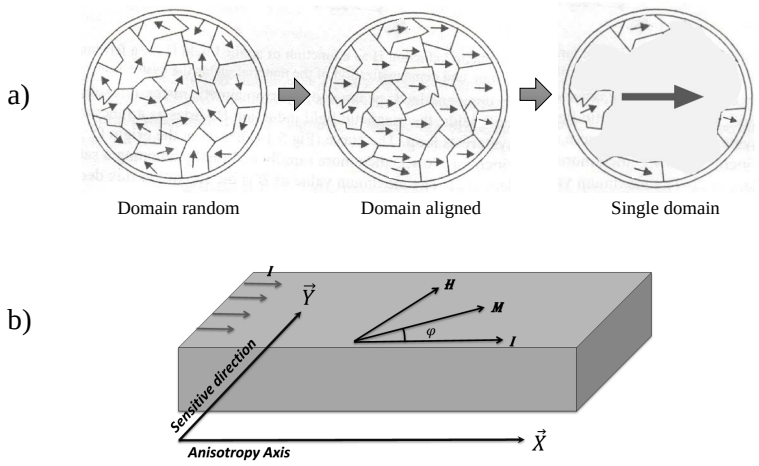

FIGURE 3.1: Magnetic field and magnetization vector in AMR sensor.

domain assumption [14]. This equation can be written as follows:

$$E = E_{mag} + E_k = -\overrightarrow{H}.\overrightarrow{M} + K_u \sin^2 \varphi \tag{3.1}$$

Where E_{mag} and E_k are the magnetostatic and anisotropy energy, respectively. Moreover, H is an external magnetic field, M is the magnetization vector, K_u is an anisotropy constant and φ is the magnetization vector angle with the anisotropy axis as depicted in Figure 3.1. Then, Equation (3.1) can be expanded to Equation (3.2), where $M_s = (\|\overrightarrow{M}\|)$ is the saturation magnetization, H_k is the anisotropy field ($H_k = \frac{2K_u}{M_s}$) and H_y and H_x are external field components.

$$E = -\mu_0 M_s(H_y sin\varphi + H_x cos\varphi) + 1/2\mu_0 M_s H_k sin^2\varphi \tag{3.2}$$

Now, in order to obtain the angle φ, the minimum magnetic energy can be considered as following equation:

$$\frac{\partial E}{\partial \varphi} = 0$$

This gives the following solution from Equation (3.2):

$$H_k sin\varphi cos\varphi = H_y cos\varphi - H_x sin\varphi \tag{3.3}$$

Assuming $\varphi \ll 1$, one has sin $\varphi \approx \varphi$ and cos $\varphi \approx 1$. Equation (3.3) becomes:

$$\varphi = \frac{H_y}{H_k + H_x} \tag{3.4}$$

Equation (3.4) indicates that if the external field is applied in the sensitive direction of

the sensor (H_y), the magnetization vector rotates. Due to this rotation, the permalloy layer resistance changes with variation in the angle.
Based on $Voigt - Thomson$ formula, the anisotropic magnetoresistance effect can be expressed as a relation between the current direction and the resistivity.

$$\rho(\varphi) = \rho_{\parallel} \cos^2 \varphi + \rho_{\perp} \sin^2 \varphi = \rho_{\parallel} - \Delta\rho \sin^2 \varphi \tag{3.5}$$

Where $\rho_{\parallel}$ and $\rho_{\perp}$ are the parallel and perpendicular components of the resistivity, $\Delta\rho$ is the difference between these two mentioned parameters ($\Delta\rho = \rho_{\parallel} - \rho_{\perp}$) and φ is the angle between the magnetization vector and the current direction. Finally, by assuming that the current direction is parallel to the sensor anisotropy axis and taking into account Equations (3.4) and (3.5), the variation in the resistance due to the external field is presented as Equation (3.6). Where $R_{H=0}$ is the resistance in a null field and ΔR is the maximum variation in the resistance.

$$R_{\varphi} = R_{H=0} - \Delta R sin^2 \varphi \tag{3.6}$$

By assuming a small value for angle φ, then,

$$\sin^2 \varphi = \varphi^2 \tag{3.7}$$

therefore, by considering Equation (3.4), Equation (3.6) can be rewritten as follows:

$$R_{\varphi} = R_{H=0} - \Delta R \left[\frac{H_y}{H_k + H_x} \right]^2 \tag{3.8}$$

This equation is true when $|H_y| < H_k$, otherwise the resistivity approaches its maximum value and remains constant. As depicted in Figure 3.2 (a), the resistance changes as a function of the external field that is measured by the sensor. However, the sensor

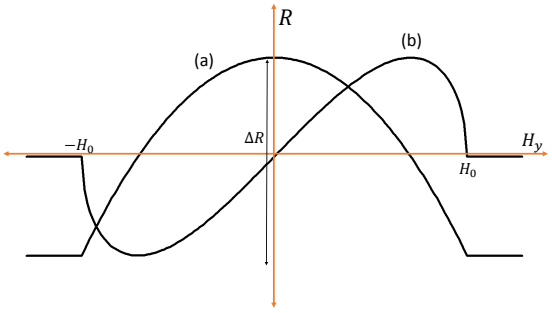

FIGURE 3.2: a) AMR sensor output b) AMR sensor output using barberpole structure.

response is not linear and the bias should be shifted to the linear region of the sensor response. Thus, one simple solution is forcing the current to flow at a 45° angle compared to the easy axis by using the barber pole structure. In this structure as depicted in

Figure 3.3, the permalloy strip is covered with the aluminum stripes, and because of the much higher conductivity of the aluminum the current orients with this angle.

Therefore, implementing this new design in the AMR sensor changes the sensor output

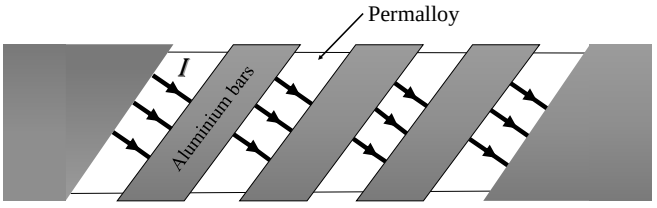

FIGURE 3.3: Barber pole design.

from Equation 3.6 to Equation 3.9 (see Figure 3.2 (b)).

$$R_{\varphi+45^\circ} = R_{H=0} - \Delta R \left[\frac{1}{2} + \underbrace{\frac{H_y}{H_k + H_x}}_{K1} \underbrace{\sqrt{1 - (\frac{H_y}{H_k + H_x})^2}}_{K2} \right] \tag{3.9}$$

This equation contains a linear ($K1$) and nonlinear part ($K2$), which changes with an

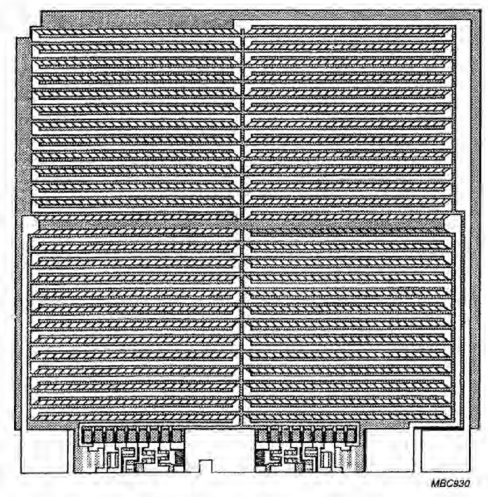

FIGURE 3.4: AMR sensor layout.

external magnetic field. However, since the anisotropy field should intrinsically be much bigger than the applied field ($H_k \gg H_y$) in the sensor range measurement, the nonlinear part can be considered as negligible.

Moreover, this equation is validated for a single permalloy element. For an AMR Wheatstone bridge as depicted in Figure 3.4, the two series elements of the bridge have a contrary angle for the barber pole design. Now, similar to Equation (3.9), for the other two elements of the Wheatstone bridge we can write:

$$R_{\varphi-45^\circ} = R_{H=0} - \Delta R \left[\frac{1}{2} - \frac{H_y}{H_k + H_x} \sqrt{1 - (\frac{H_y}{H_k + H_x})^2} \right] \tag{3.10}$$

Therefore, the sensor output in a bridge configuration supplied with the voltage source can be expressed as follows:

$$V_{out} = V_{supply} \frac{R_{\varphi+45} - R_{\varphi-45}}{R_{\varphi+45} + R_{\varphi-45}} \tag{3.11}$$

By using Equation (3.9) and Equation (3.10),

$$V_{out} = V_{supply} \frac{\Delta R}{R} \frac{H_y}{H_k + H_x} \sqrt{1 - (\frac{H_y}{H_k + H_x})^2} \tag{3.12}$$

Generally, this equation can be simplified by replacing the a parameter that contributes to the sensitivity of the sensor.

$$V_{out} = a \frac{H_y}{H_k + H_x} \sqrt{1 - (\frac{H_y}{H_k + H_x})^2} \tag{3.13}$$

The bridge configuration causes two main advantages for the AMR sensors. First, compared to the single element sensor, the sensitivity of the bridge sensor improves by factor two. Second, since for each side of the AMR Sensor bridge, the equivalent resistance of $R_{\varphi+45} + R_{\varphi-45}$ is constant regardless of the sensed magnetic field, consequently, the whole bridge performs as a constant resistance. This helps to have a better sensor linearity response as a consequence of the stable current through the permalloy layers even if the resistance changes.

For ($H_k^2 \gg H_y^2$ & H_x^2), Equation (3.13) can be simplified as follows:

$$V_{out} \approx a \frac{H_y}{H_k + H_x} \tag{3.14}$$

3.2 Temperature effect.

There are two sources of thermal variation in the AMR sensor behavior. First, the bridge resistances that increase linearly with the temperature. Second, the sensitivity of the AMR material also varies due to the magnetic domain behavior. This sensitivity

in this case often decreases with the temperature increment.
In the following part we investigate the comparison of using a voltage and then current supply for driving the AMR bridge. Assume that the AMR Wheatstone bridge has a nominal resistance as depicted in Figure 3.5. Here we consider that the bridge has

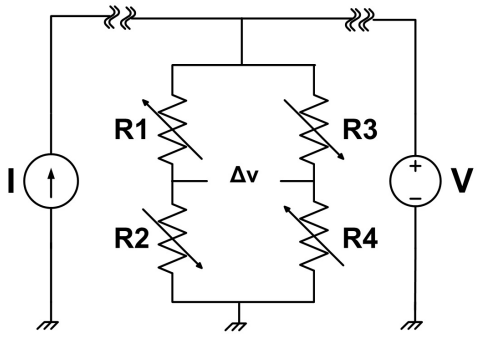

FIGURE 3.5: Simple schematic of AMR bridge

unbalance resistances with the same thermal coefficient $(1 + \alpha\Delta\theta)$ due to the unique material properties (α is the temperature coefficient and $\Delta\theta$ represents the temperature variation). Therefore, by driving the AMR bridge with a constant voltage, we can easily write:

$$\Delta v = V\left(\frac{R_2}{R_1 + R_2} - \frac{R_4}{R_3 + R_4}\right) \tag{3.15}$$

and then by adding a thermal coefficient:

$$\Delta v(\theta) = V\left(\frac{R_2(1 + \alpha\Delta\theta)}{(R_1 + R_2)(1 + \alpha\Delta\theta)} - \frac{R_4(1 + \alpha\Delta\theta)}{(R_3 + R_4)(1 + \alpha\Delta\theta)}\right) \tag{3.16}$$

Consequently,

$$\frac{d\Delta v(\theta)}{d\theta} = 0 \tag{3.17}$$

This result leads us to believe that, theoretically, the bridge offset should be independent of the temperature variation by using a constant voltage. Although, when the voltage source is fixed, the current varies intrinsically with the temperature, and so then, the sensor sensitivity varies with the thermal coefficient.
Now let us examine the temperature effect on the sensitivity. As remarked earlier a represents the sensitivity properties of the sensor ($a = V_{supply}\frac{\Delta R}{R}$). In other words, a is proportional to the supply voltage as well as the current supply (Equation (3.19)). Therefore, first we introduce,

$$\begin{cases} R_{eq} = (R_1 + R_2) \parallel (R_3 + R_4) \\ R_{eq}(\theta) = (1 + \alpha\Delta\theta)R_{eq} \end{cases} \tag{3.18}$$

then by using a constant voltage ($V = V_{supply}$),

$$a(\theta) \propto I(\theta) = \frac{V}{R_{eq}(1 + \alpha\Delta\theta)} \tag{3.19}$$

since we can assume $(\alpha\Delta\theta)^2 < 1$, then by using the Taylor series,

$$\frac{V}{R_{eq}(1 + \alpha\Delta\theta)} = \frac{V}{R_{eq}} \sum_{0}^{n} (-\alpha\Delta\theta)^n = \frac{V}{R_{eq}}[1 - \alpha\Delta\theta + (\alpha\Delta\theta)^2 + \dots] \tag{3.20}$$

by considering that,

$$\sum_{3}^{n} (-\alpha\Delta\theta)^n \approx 0 \tag{3.21}$$

finally,

$$\frac{da(\theta)}{d\theta} \propto V[-\alpha + 2\alpha^2 d\theta] \tag{3.22}$$

It is apparent from Equation (3.22) that using the constant voltage source causes additional thermal drift to the sensor measurement. This equation presents a nonlinear relation as a function of temperature. However, since α has a small value, the nonlinear part can be considered negligible.
In another case using the current source in Figure 3.5 leads to have following equations for the bias of the bridge.

$$\Delta v = I\frac{R_2(R_3 + R_4) - R_4(R_1 + R_2)}{R_1 + R_2 + R_3 + R_4} = IR_{total} \tag{3.23}$$

Where as a function of the temperature yields:

$$\Delta v(\theta) = IR_{total}(1 + \alpha\Delta\theta) \tag{3.24}$$

Therefore, according to this equation, the sensor bias varies with the thermal coefficient of the resistance and the supplying current.

$$\frac{d\Delta v(\theta)}{d\theta} = \alpha I R_{total} \tag{3.25}$$

Finally, as the current is constant, the proportion of the sensitivity remains fixed regardless of resistance variation. As mentioned earlier, the permalloy resistance of the AMR sensor changes with magnitude and direction of the applied field compared to the current that flows to the permalloy layers.

$$\frac{dI}{d\theta} \propto \frac{da}{d\theta} = 0 \tag{3.26}$$

To conclude this part of the subject, therefore, using a current source is more appropriate for driving the AMR bridge in order to obtain a more linear response [54]; and also to reduce the low frequency noise of the sensor [55]. However, in this case, the sensor bias varies with the temperature. This drawback can be compensated effectively using the flipping method as will be explained in section 3.4.
As noted earlier, several studies have proposed using more current or voltage for supplying the bridge to improve the sensor resolution [56]. However, it is apparent from Equation (3.22) and Equation (3.24) that this method causes more thermal drift of the sensor measurement.

3.3 Cross-field effect

As illustrated in Figure 3.13, the AMR sensor is generally sensitive to a magnetic field vector in its sensitive axis. However, all the magnetoresistive sensors have an inherent sensitivity to the perpendicular field to the sensitive axis. This effect is the so called cross-field effect or cross-field error is represented by H_x in Equation (3.13). This effect mostly comes from the dimensional characteristics of the sensor layout and has an inverse relation to the sensor sensitivity [57]. By increasing H_k, obviously, the cross-field effect will be reduced, but on the other hand, the sensitivity also behaves the same way. In order to investigate the dependency of the anisotropy field with the geometry of the sensor or strip, we need to consider an additional component to the free energy of the system in the Equation (3.1). This parameter is usually known as shape anisotropy field $H_d = NM_s$ (where N is the demagnetizing factor) [58]. Almasi and co-workers [59] proposed to use the shape anisotropy as a method to decrease the anisotropy field of a thin film material by the following equation:

$$H_k = \left(\frac{t}{w} - \frac{t}{l}\right) M - H_{ko} \tag{3.27}$$

where H_{ko} is the anisotropy of material, l is the dimension of the sensing element in its long direction, w is the dimension of the sensing element in its short direction and t is the thickness.
Using negative feedback loop or flipping methods also greatly improves the sensor measurement that will be discussed in sections 3.4.1 and 5.1.1.2. Figure 3.6 presents the sensor measurement in different situations due to the cross axis effect. On the left, the simulation result of the sensor error measurement has been plotted when the sensor is exposed in the different perpendicular fields to its sensitive axis. Moreover, the right figure shows the cross-field error on the sensor measurement when the sensor has different anisotropy fields (H_k).

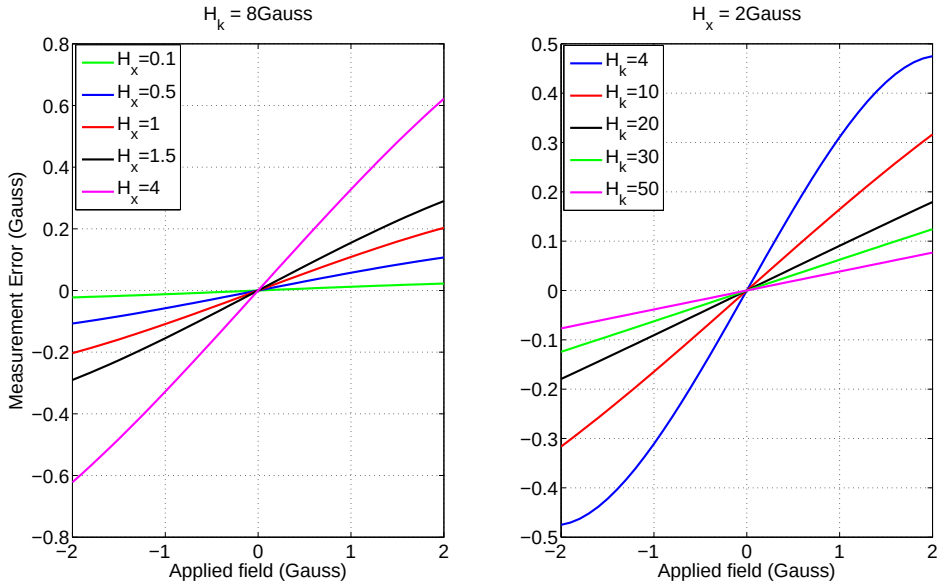

FIGURE 3.6: Simulation results of the error field measurement due to the different cross-field and anisotropy field.

3.4 Flipping

The most commonly used method for improving the AMR sensor performance is flipping or set/reset method [60][61][62]. This method provides better sensor precision, noise performances and sensitivity. However, among other advantages, the most outstanding one, is to obtain sensor bias stability. In this section, we explain how this method will improve sensor performances.

Nowadays most available AMR sensors include a set/reset strap that consists of a spiral conductor for each AMR bridge. This strap provides a sufficiently strong corresponding magnetic field into the sensor to recover the magnetic domain and change the sensor magnetization periodically. Therefore, even if the sensor is exposed to an externally applied magnetic field that may disturb the magnetic domains and consequently changes the sensor bias, the set/reset strap can be used to refresh the sensor.

Figure 3.7 illustrates the behavior of a Wheatstone bridge and the magnetic domains while the flipping method is used. In this case, in part *a*, the magnetic domains have been damaged due to the sensor vicinity by a strong magnetic field. Thus, the sensor has uncommon sensitivity and bias. This unusual behavior has been presented with different parameters (ΔR, $\Delta R'$, $\Delta R''$ and $\Delta R'''$). Furthermore, to simplify the equations, the original bridge offset of the sensor is uniquely presented by ϵ on one leg of the bridge. Part *b* presents the magnetic domains when the SET field is applied and therewith the effect of RESET field is presented in part *c*. After RESET pulse, the magnetization of the permalloy layers are reversed, corresponding to the current direction through the strap. Hence, as has been depicted in Figure 3.7, the bridge resistances vary with

different polarities related to the same applied field after each SET and RESET.
The maximum sensor sensitivity appears when all the magnetic domains align in one direction. Therefore, any distortion of these domains will reduce the sensor sensitivity. On the other hand, another problem may arise due to the self-noise of the sensor. This noise will increase due to the thermal energy of the sensor over time. Consequently, by employing the flipping method to realign these domains, the sensitivity and the self-noise of the sensor remain at its highest and lowest possible values respectively [60].

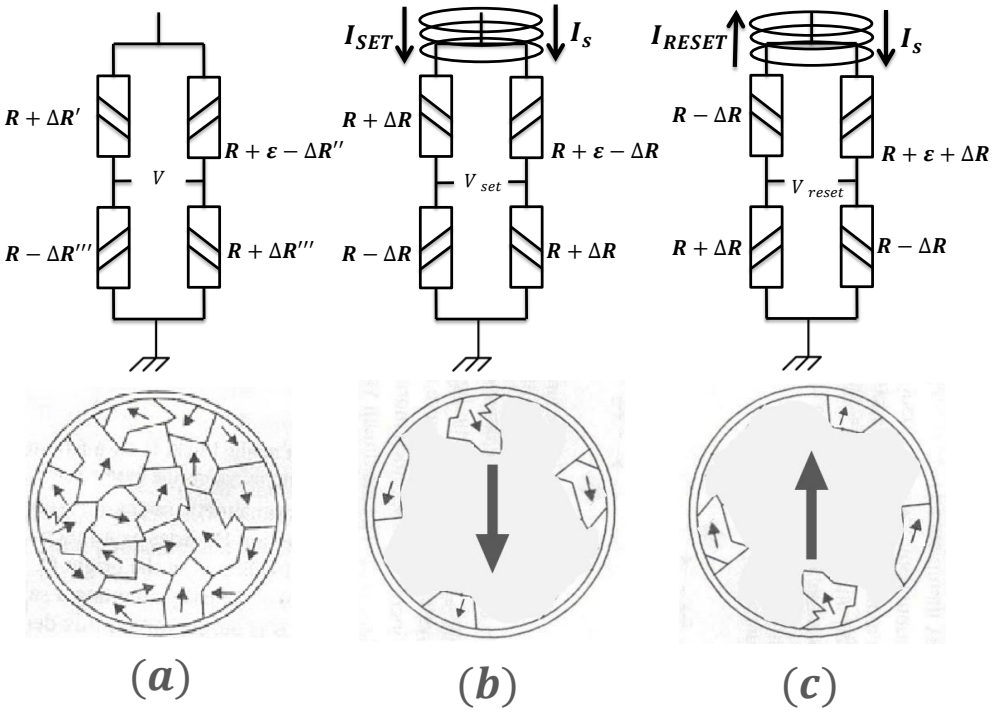

FIGURE 3.7: *a*) presents random domain orientations of permalloy layer when it exposed to a magnetic disturbing field; *b*) depicts magnetic domain direction after a set pulse and *c* after a reset pulse .

3.4.1 Cross-field error compensation

The origin of the cross axis error was explained earlier. It has also been stated that this error can be reduced by using the flipping method. In order to verify this, we turn back to Equation (3.13), and take a simplifying assumption to avoid complex calculation.

$$x_1 = \frac{H_y}{H_x + H_k} \tag{3.28}$$

$$x_2 = \frac{H_y}{H_x - H_k} \tag{3.29}$$

Now, according to Taylor series, two following equations can be written:

$$V_{set} = ax_1\left(1 - \frac{1}{2}x_1^2 + \dots\right) \tag{3.30}$$

$$V_{reset} = ax_2\left(1 - \frac{1}{2}x_2^2 + \dots\right) \tag{3.31}$$

Then,

$$\frac{V_{set} - V_{reset}}{2} = a\left(\frac{1}{2}\left[x_1 - x_2\right] + \frac{1}{4}\left[x_2^3 - x_1^3\right]\right) \tag{3.32}$$

$$= \frac{a}{4}\left(x_1 - x_2\right)\left(2 - x_2^2 - x_1^2 - x_1x_2\right) \tag{3.33}$$

$$= \frac{a}{4}\left[\left(\frac{H_y}{H_x + H_k} - \frac{H_y}{H_x - H_k}\right)\left(2 - \left(\frac{H_y}{H_x - H_k}\right)^2 - \left(\frac{H_y}{H_x + H_k}\right)^2 - \left(\frac{H_y}{H_x - H_k}\right)\left(\frac{H_y}{H_x + H_k}\right)\right)\right] \tag{3.34}$$

Now assume that $H_k^2 \gg H_x^2$, then, $(H_x + H_k)^2 \cong H_k^2$ and $H_k^2 - H_x^2 \cong H_k^2$. Therefore, the last equation yields:

$$V_{out} \approx \frac{aH_y}{2H_k}\left(2 - \left(\frac{H_y}{H_k}\right)^2\right) \tag{3.35}$$

By adding one more assumption ($H_k^2 \gg H_y^2$), Equation (3.35) can be rewritten as:

$$V_{out} \approx \frac{aH_y}{H_k} \tag{3.36}$$

To conclude, if the flipping method is used, a comparison of two equations (Equation (3.14) and Equation (3.36)), reveals that the linear response of AMR sensor will be improved according to Equation (3.36). In other words, Equation (3.34) is less sensitive to the cross-field effect than Equation (3.13).

Figure 3.8 illustrates the simulation results of the cross-field effect on the sensor measurement using Equation (3.34) in red and Equation (3.13) in blue. In this case, we have considered an applied magnetic field along the sensitivity axis ($Hy = 1G$), a perpendicular magnetic field (Hx) that varies from $-3G$ to $3G$, and the anisotropy field with a value of $8G$. As evidenced here, the flipping method compensates the non-linearity error of the sensor output that is caused by the cross-field effect.

3.4.2 Temperature drift on the bias measurement

According to the AMR bridge configuration in Figure 3.7 we can easily write:

$$V_{set} = I_s\left[R\left(\frac{\epsilon}{4R + \epsilon}\right) - \Delta R\right] \tag{3.37}$$

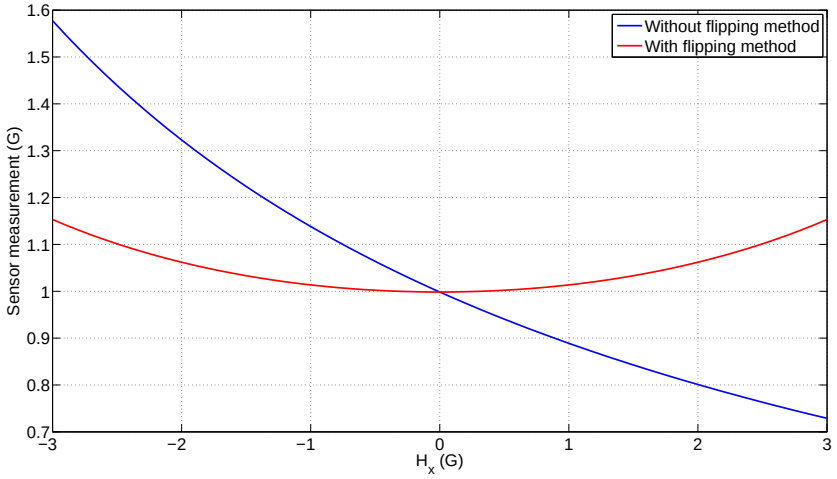

FIGURE 3.8: Comparison of the sensor measurement error due to the cross-field effect with and without using flipping method. The true reading of the sensor should be equal to one Gauss.

$$V_{reset} = I_s \left[R \left(\frac{\epsilon}{4R + \epsilon} \right) + \Delta R \right] \tag{3.38}$$

$$V_{S/R} = \frac{V_{set} - V_{reset}}{2} \tag{3.39}$$

Assume now that the AMR bridge has been supplied with a constant current. The resistances have the same thermal coefficient $(1 + \alpha\Delta\theta)$ for R and ϵ, and ΔR varies solely due to the applied magnetic field. Then,

$$V(\theta)_{set} = I_s \left[R \left(\frac{\epsilon}{4R + \epsilon} \right) (1 + \alpha\Delta\theta) - \Delta R \right] \tag{3.40}$$

$$V(\theta)_{reset} = I_s \left[R \left(\frac{\epsilon}{4R + \epsilon} \right) (1 + \alpha\Delta\theta) + \Delta R \right] \tag{3.41}$$

Therefore,

$$\frac{dV_{set}(\theta)}{d\theta} = \frac{dV_{reset}(\theta)}{d\theta} = \frac{I_s R \epsilon \alpha}{4R + \epsilon} \tag{3.42}$$

Then,

$$\frac{dV_{S/R}}{d\theta} = 0 \tag{3.43}$$

As evidence in this equation, theoretically, the temperature drift of the sensor bias can be compensated using the flipping method.

To investigate and validate the functionality of the flipping method, an AMR sensor (HMC102X) with a driving current of 5mA has been selected. The schematic of this circuit has been shown in Figure 3.9. Figure 3.10 represents the variation of the sensor sensitivity with respect to the temperature. The red color depicts the obtained result

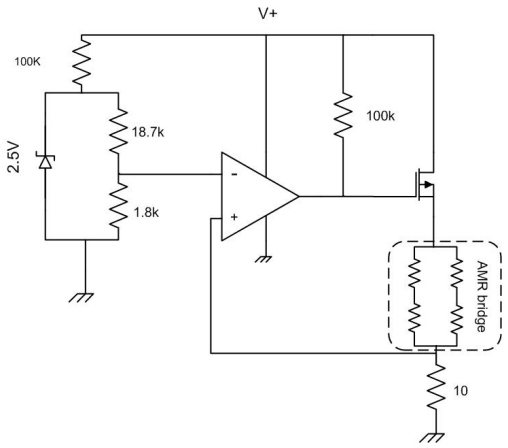

FIGURE 3.9: Schematic of the current source design for driving the AMR bridge.

when the flipping method is used and the blue color is that without using the method. Moreover, the bias variation as a consequence of the temperature is reported separately in Figure 3.11 and 3.12. According to these results, the sensor sensitivity has the same coefficient as a function of temperature in both cases. For the sensor bias, as expected from the theoretical results, the results show that using the flipping method improves the bias thermal drift of the sensor by more than 20 times.

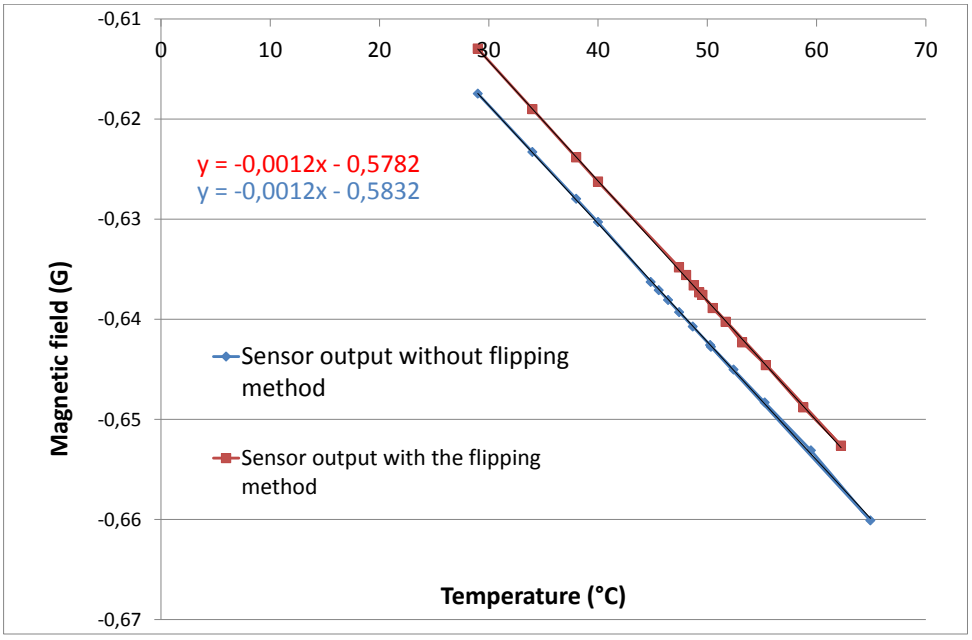

FIGURE 3.10: Comparison of thermal drift of the flipped sensor in red and in the normal operation in blue.

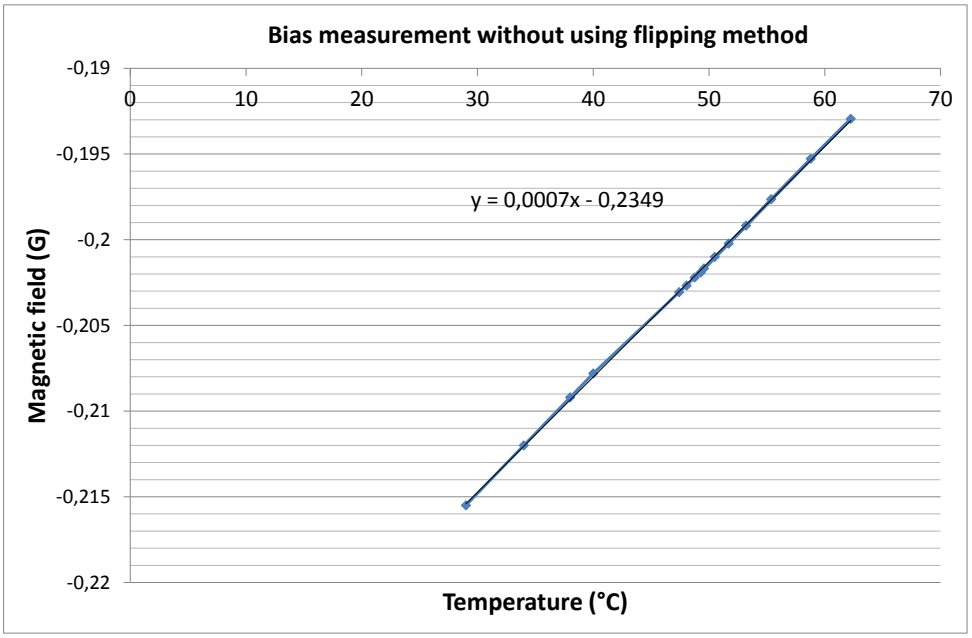

FIGURE 3.11: Bias thermal drift of non-filliped sensor.

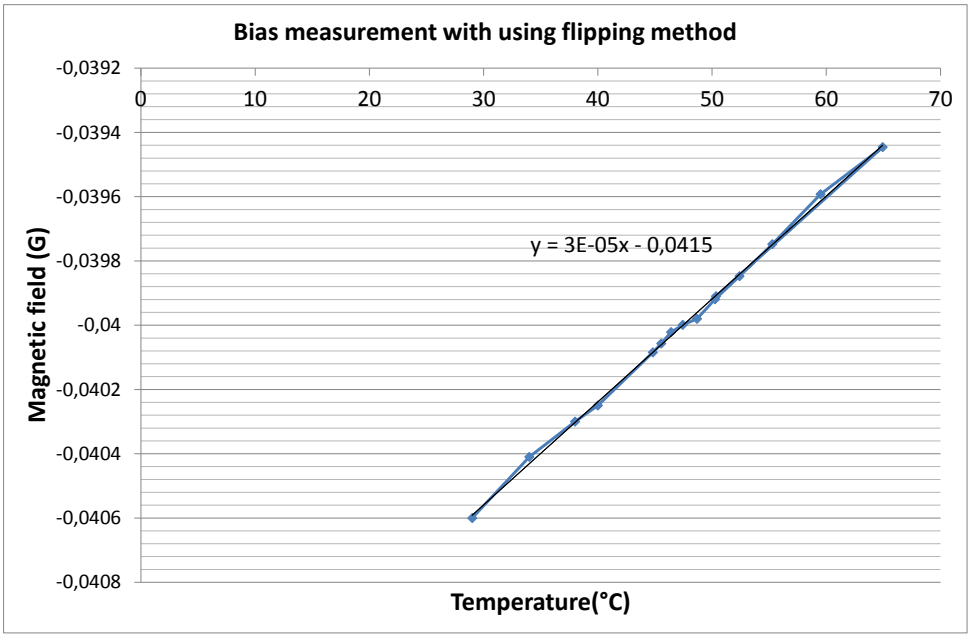

FIGURE 3.12: Bias thermal drift of flipped sensor.

3.4.3 Power consumption of flipping method

In general, the typical flipping frequency is about 100-200 Hz for low frequency measurement. However, in some cases the flipping frequency can be exceeded to tens of kilohertz in order to achieve the maximum resolution of the sensor. In low frequency application, low frequency noise is the main critical problem. In all front end electronic design this noise exists in power supplies, sensors, amplifiers, resistors, etc. Chopper stabilization is one of the effective methods that can be employed to remove the low frequency noise of the amplifiers [63]. This method is based on the modulation and demodulation technique (Figure 3.13 (a)). As depicted in Figure 3.13 (b), first, the sensor output that contains of signal and noise is modulated by a carrier to higher frequencies where the low frequency noise of the amplifier is less (c). Note that the modulation frequency should be greater than the corner frequency of the amplifier noise. In addition, due to this modulation, the odd harmonics of the sensor signal appear as well. After the amplification and adding the amplifier noise (d), the signal is demodulated by the same frequency as modulation and turn back to its previous frequency. This new operation converts the signal harmonics to even harmonics, and since the amplifier noise is modulated once, its odd harmonics will appear. Finally, in order to recover the clean output signal from the modulation noise and harmonics, a low pass filter is implemented at the end of the chain (e). In AMR sensors, flipping method operates as a modulation. Consequently, as mentioned earlier, this modulation helps to shift the sensor signal to a higher frequency to improve the sensor resolution. Meanwhile the flipping frequency depends on the corner frequency of the electronic low frequency noise.
However, one should not forget that using the flipping method increases the power consumption of the sensor and this can be viewed as a serious problem in most of the applications. In order to apply the pulse magnetic field, a simple RC circuit can be used consisting of half or full-bridge of transistors with a low drain source resistance. Moreover, to reduce the thermal drift of the sensor measurement, the power dissipated should be much lower via the set/reset strap compared to the sensor power consumption. Although, this strap needs a high current (few amps) to re-align the magnetic domains, the pulse duration is quite small. For instance, the HMC102X from Honeywell needs at least a pulse width current of around five micro seconds.
An example of an electronic design for flipping circuit has been presented in Figure 3.14. The two pair complementary power MOSFETs (IRF7509) are used to provide a fast switching performance with a low drain source resistance (less than 1Ω). The charge-pump (MAX662) converter is used to provide 12V for supplying the bridge. For each edge of the clock, the pulse current flows through one p-channel, n-channel MOSFET transistors and the flipping coil to charge and discharge the series capacitor.

The dynamic power dissipated of RC circuit can be formulated easily by the energy

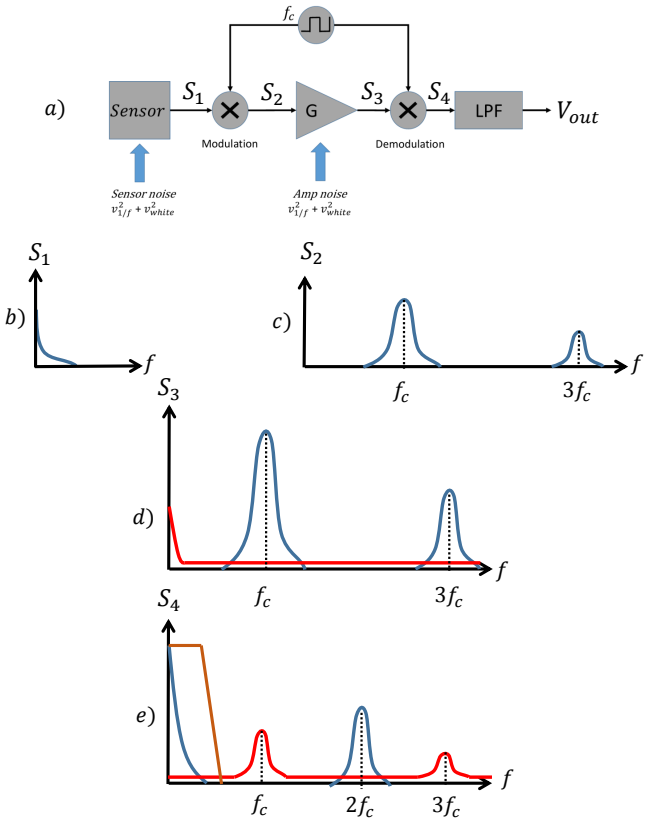

FIGURE 3.13: Principle of Chopper Stabilization technique. b) Spectrum of sensor signal. c) Spectrum of modulated sensor signal at chopping or flipping frequency. d) Spectrum of modulated signal after amplification and amplifier noise. e) Spectrum of demodulated signal and amplifier noise. LPF eliminates most of the flicker noise.

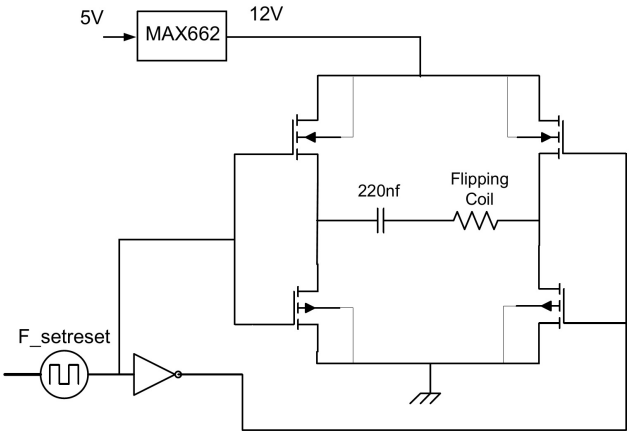

FIGURE 3.14: Schematic of switching circuit for driving set/reset pulse for AMR sensors.

equation:

$$P(f) = CV^2 f$$

Due to this equation, the power dissipated of RC circuit by substituting 220nf for capacitor and 12V for charging voltage is close to 32mW at 1 kHz frequency for charging and discharging the capacitor. However, the finding of the experimental test shows that the power consumption by using the flipping method may be greater than expected because of the power dissipated in other components. Figure 3.15 illustrates the power consumption of an electronic design as a function of flipping frequency. The set/reset straps of three sensors (HMC1021 & HMC1022) are connected as series with 220nF ceramic capacitor, and a microcontroller (STM32F4) from ARM families has been used to drive the H-bridge design.

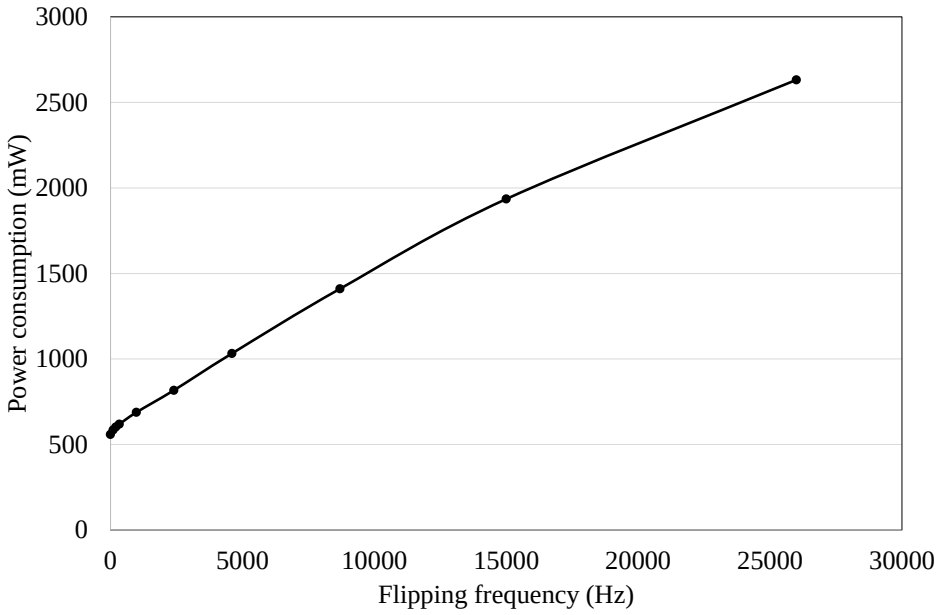

FIGURE 3.15: Power consumption of sensor board (HMC102X) as a function of flipping frequency.

3.5 Low-cost electronic design

Because of MEMS technologies, low-cost AMR magnetometers with considerable performances are now available for a few dollars. Thus, it is also a good idea to investigate low-cost solutions for electronic design. One possible solution is to reduce the number of

channels in the case of having multiple sensors. For instance, as depicted in Figure 3.16 for triple sensor axis, only one electronic channel can be designed by implementing an analog multiplexer before amplification part. This configuration results in a saving on

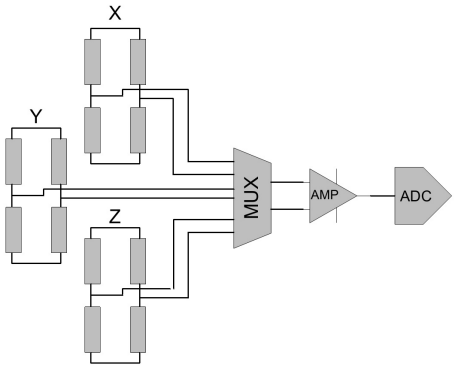

FIGURE 3.16: Typical low-cost design for three-axis AMR sensors using a analog multiplexer.

cost and PCB size. However, this may not always be the case in terms of power consumption for keeping the same sampling rate per sensor axis. Although, on the one hand, the number of components and the power consumption are reduced by using the multiplexer, on the other, the digital part needs more power as a consequence of operating at a higher frequency. Likewise, due to the same reason, if the sensor is used in the flipping mode, the power dissipated of the analog part will increase as well.
Using the classical amplifier also helps to save costs compared to the instrumentation one. However, in this case two buffers should be connected to the sensor output to provide a high input impedance (Figure 3.17).

Before presenting any experimental results, we analyze the noise model of the circuit design illustrated in Figure 3.17.

Sensor noise model

First, we analyze the resistance noise of the sensor by grounding the bridge supply (see Figure 3.18). In this case, each input of the first stage sees the half of the bridge resistances. Then, the thermal noise of the sensor can be expressed as:

$$Eth_1 = Eth_2 = \sqrt{4kT\frac{R}{2}} \tag{3.44}$$

Where k is the Boltzmann's constant and T is the temperature in Kelvin. Meanwhile, the current noise of the amplifiers also participates in resistance noise of the bridge and

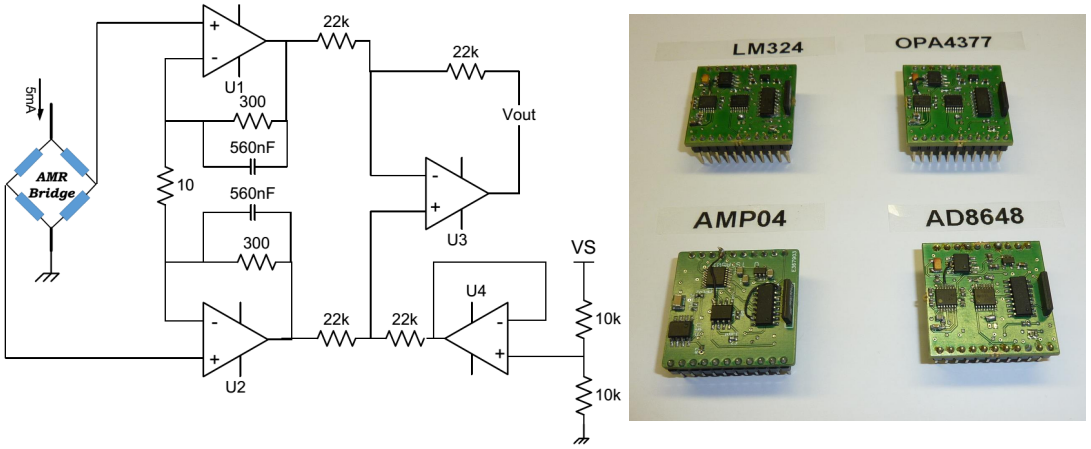

FIGURE 3.17: Schematic of an instrumental amplifier using a combination of three operational amplifiers. The input signal is amplified by two buffers (U1 & U2) and then the output signals from the buffers are connect to a subtractor (U3). Meanwhile, a 2.5 V reference voltage is added by U4.

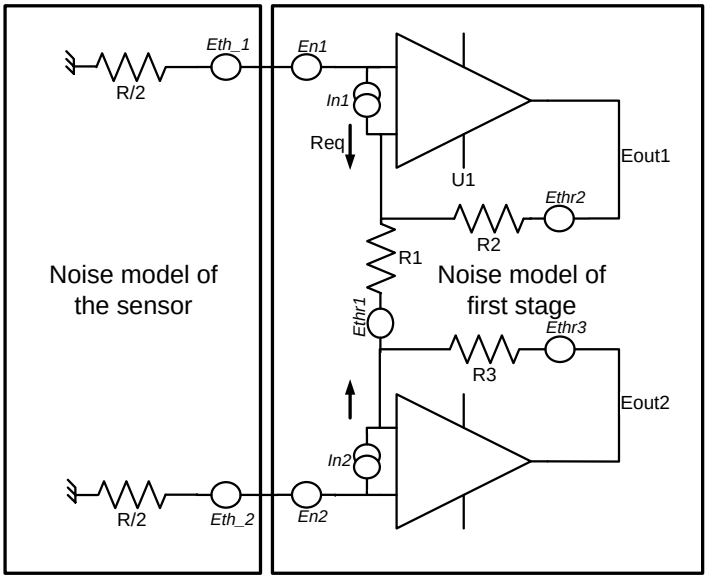

FIGURE 3.18: Noise equivalent circuit for typical bridge sensor and the first stage of instrument amplifier.

appears as a voltage noise. By assuming $In1 = In2$ in Figure 3.18 we can write:

$$Ei = In1\frac{R}{2} = In2\frac{R}{2} \tag{3.45}$$

Finally the total resistance noise of the sensor for each input of the amplifiers is:

$$E_{sen1} = E_{sen2} = \sqrt{Ei^2 + Eth_1^2} \tag{3.46}$$

First stage noise model of amplifier

The first (input) stage normally has the total gain of the instrument amplifier. Moreover, since the design can be considered as a symmetric circuit, finding the noise parameter of one amplifier (see Figure 3.18) could be sufficient. To calculate the thermal noise we can write:

$$R_{eq} = R2\|(R1 + R3) \tag{3.47}$$

Therefore, the current noise Ei_{u1} can be written as follows:

$$Ei_{u1} = In1.R_{eq} \tag{3.48}$$

The total noise contribution at the output of U1 due to the thermal resistances noise is:

$$Eth_{u1} = \sqrt{(E_{thr2})^2 + ((E_{thr1})^2 + (E_{thr3})^2).(\frac{R2}{R1})^2} = \sqrt{4kTR2 + 4kT(R1 + R3)(\frac{R2}{R1})^2} \tag{3.49}$$

Then, the total output noise is:

$$E_{out1} = \sqrt{(Ei_{u1}.\frac{R2}{R1})^2 + (Eth_{u1})^2 + ((En1)^2 + (E_{sen1})^2)(\frac{1 + 2\frac{R2}{R1}}{2})^2} \tag{3.50}$$

Reference buffer noise contribution

Figure 3.19 illustrates the noise model of the reference buffer circuit. This design allows one to use the instrument amplifier with a single supply by adding the reference voltage to the output. This reference voltage can be provided easily by using the voltage divider and should be isolated with a buffer by creating a high impedance. Considering the introduced parameters in Figure 3.19, the equations below present the noise contribution due to the thermal noise (E_{thr9}), current amplifier noise (Ei_{buffer}), input voltage noise (E_{in4}) and finally the total noise at the output of the buffer (E_{ref}).

$$R_{eq} = R9\|R10 \tag{3.51}$$

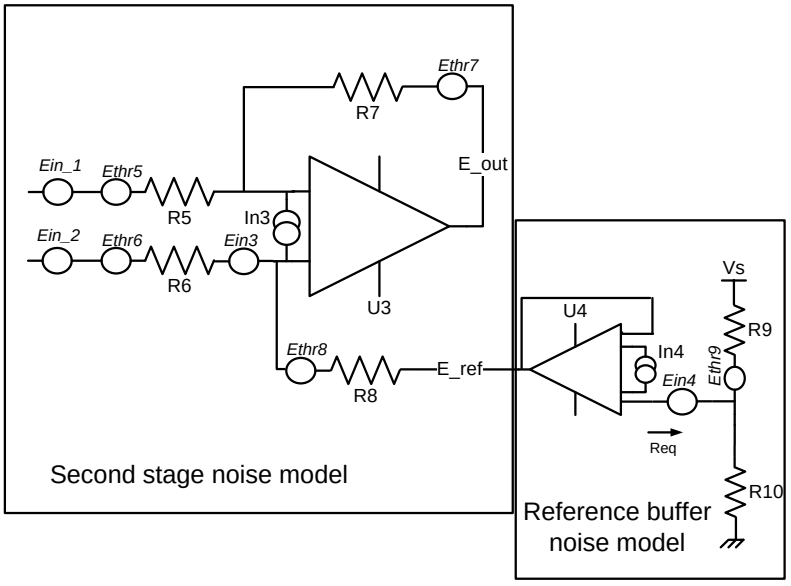

FIGURE 3.19: Noise equivalent circuit for typical reference buffer circuit and the second stage of instrument amplifier.

$$E_{thr9} = \sqrt{4kTR_{eq}} \tag{3.52}$$

$$Ei_{buffer} = In4.Req \tag{3.53}$$

$$E_{ref} = \sqrt{E_{thr9}^2 + E_{in4}^2 + Ei_{buffer}^2} \tag{3.54}$$

Second stage noise model of amplifier

Now, by turning back to Figure 3.19 and using the superposition low, the contribution of each input noise source can be computed separately at the output of the second stage amplifier. Thus, for the thermal noises we can write:

$$E_{out-thermal}^2 = \Bigg((E_{thr5}(\frac{R7}{R5}))^2 + (E_{thr6}(\frac{R8}{R6+R8})(\frac{R5+R7}{R5}))^2 + \\ + (E_{thr8}(\frac{R6}{R6+R8})(\frac{R5+R7}{R5}))^2 + (E_{thr7})^2 \Bigg) \tag{3.55}$$

Then, for the output noise caused by the first stage we have,

$$E_{out-input}^2 = (E_{out1}(\frac{R8}{R6+R8})(\frac{R5+R7}{R5}))^2 + (E_{out2}(\frac{R7}{R5}))^2 \tag{3.56}$$

and the contribution of the current noise can be written as:

$$E^2_{out-current} = (In3(\frac{R5R7}{R5+R7})(\frac{R5+R7}{R5}))^2 + (In3(\frac{R6R8}{R6+R8})(\frac{R5+R7}{R5}))^2 \quad (3.57)$$

Then, the intrinsic voltage input noise of U3 will appear at the output by,

$$E_{out-u3} = (E_{in3}(\frac{R5+R7}{R5})(\frac{R6}{R6+R8})) \quad (3.58)$$

Finally, the noise contribution of the reference buffer circuit from Equation (3.54) at the output of the second stage is:

$$E_{out-buffer} = (E_{ref}(\frac{R6}{R6+R8})(\frac{R5+R7}{R5})) \quad (3.59)$$

Now, by assuming a gain of one ($R5 = R6 = R7 = R8 = R$) for the second stage amplifier, the above equations change to:

$$E^2_{out-thermal} = E^2_{thr5} + E^2_{thr6} + E^2_{thr7} + E^2_{thr8} \quad (3.60)$$

$$E^2_{out-input} = E^2_{out1} + E^2_{out2} \quad (3.61)$$

$$E^2_{out-current} = (In3.R)^2 + (In3.R)^2 \quad (3.62)$$

$$E_{out-u3} = E_{in3} \quad (3.63)$$

Therefore the total noise at the output of the second stage amplifier can be expressed as:

$$E_{out-total} = \sqrt{E^2_{out-thermal} + E^2_{out-input} + E^2_{out-current} + E^2_{out-u3} + E^2_{out-buffer}} \quad (3.64)$$

Moreover to compute the total rms noise in the noise bandwidth, we can write:

$$E_{total-rms} = E_{out-total}\sqrt{BW} \quad (3.65)$$

and,

$$BW = K_n.f \quad (3.66)$$

where f is the cut-off frequency (frequency response) and K_n is the brick wall correction factor that depends on the type of the filtering or number of poles in filter (see Table 3.1).

To conclude this part of the discussion, we summarize with some remarks for this type of design.

First, replacing the resistance with lower values can significantly reduce the thermal

Number of poles	K_n
1	1.57
2	1.22
3	1.16
4	1.13
5	1.12

TABLE 3.1: Brick wall correction factor with different number of poles in filter.

noise. This is a critical point especially in the first stage amplifier where the gain is high. However, it must be observed that, this method of improving the noise can increase the power consumption, especially in the reference buffer part.

Second, the current noise of the amplifiers varies widely. This parameter can be from around $0.1fA/\sqrt{Hz}$ to several $pA/\sqrt{Hz}$. Essentially, the effect of the current noise depends on the impedance around it. Therefore, if the gain resistors or the sensors have a big value, the current noise of the amplifier can play a significant role in the total noise. In some cases the amplifier may only have a good performance for the input voltage noise but not for the current noise. For instance, LT1028 from the Linear Technologies has the input voltage noise density around $1nV/\sqrt{Hz}$ but quite high current noise around $4.7pA/\sqrt{Hz}$. Consequently, using this amplifier with a high value of the gain and equivalent input resistors may result in unexpected noise performances.

Third, it is important to identify the dominant noise components. In other words, the noise contribution of the other components can be neglected compared to the dominant one. Therefore, from the cost point of view, we only need to optimize the components that make a dominant noise contribution. In general, the first stage amplifiers that have a significantly higher gain than the others can be considered the dominant noise contribution parts.

To give an example, we compute the noise parameters illustrated in Figure 3.17 by using OPA4377 as an operational amplifier. From the datasheet we obtain $2fA/\sqrt{Hz}$ and $7.5nV/\sqrt{Hz}$ for the current noise and voltage noise at 1 kHz respectively. By using the proposed equations, the noise parameters have been calculated in Table 3.2. Note that the rms noise has been obtained by implementing a single pole low pass filter at 1kHz. As stated earlier, here we can see clearly that the first stage of the amplifier is the dominant contribution to the total output noise.

In order to investigate the performances of the low cost classical amplifiers, three have been chosen from among those of lower prices. Although, they have a poor datasheet (especially for LM324) and it is not possible to compute their noise performances with a good accuracy. As a result, each classical amplifier has been tested separately (see Figure 3.17). However, here the only difference is the component that is used as an amplifier and all the remaining components, such as sensor, flipping circuit, power supplies,

Noise parameter	$nV/\sqrt{Hz}$
$E_{out-thermal}$	37
$E_{out-input}$	329
$E_{out-current}$	31
E_{out-u3}	7.5
$E_{out-buffer}$	20
$E_{out-total}$	334
$E_{total-rms}$	1.32×10^4

TABLE 3.2: Computation of the noise parameters for OPA4377.

ADC and also the PCB layout are the same.
According to our experimental finding, LM324 can be selected as a suitable candidate for this aim at an unbelievable cost of only 0.1 $ (price each in 1000 quantities) for a quad - amplifier. Figure 3.20, compares the noise performance results for using an AMR magnetometer (HMC102X) when it is amplified by several of the chosen low-cost classical amplifiers (see Table 3.3). We compared the performances of these amplifiers with an instrumentation one (AMP04, which is originally used by Honeywell in HMR2300). Note that, all the amplifiers are set to have the same gain (60) and cut of the frequency at 1 kHz. A 16 bit ADC (CS5509) is used to convert the analog voltage of the magnetometer when it flipped at 150Hz. As discussed earlier, the amplifiers have not been characterized precisely in the datasheets. Consequently, the output noise obtained experimentally shows more value than by calculation from the given parameter in the datasheet. Moreover, the power supply noise, and the magnetic noise of the sensor are part of this additional noise value.

Amplifier	Cost
LM324	0.1$ @1000
OPA4377	1.25$ @1000
AD8648	1.3$ @1000
AMP04	10$ @1000

TABLE 3.3: List of tested amplifiers and their prices.

3.6 Sensor performances and equivalent magnetic noise

Most of the AMR sensors available today do an excellent job of sensing magnetic field within the Earth's magnetic fields, and they can measure both linear and angular positions. Furthermore, the AMR sensors are the most stable of the magnetoresistance sensors and their bias remains constant during the sensor life. However, these advantages can only be obtained by using some techniques for improving the sensor performances that will be explained in the following sections.

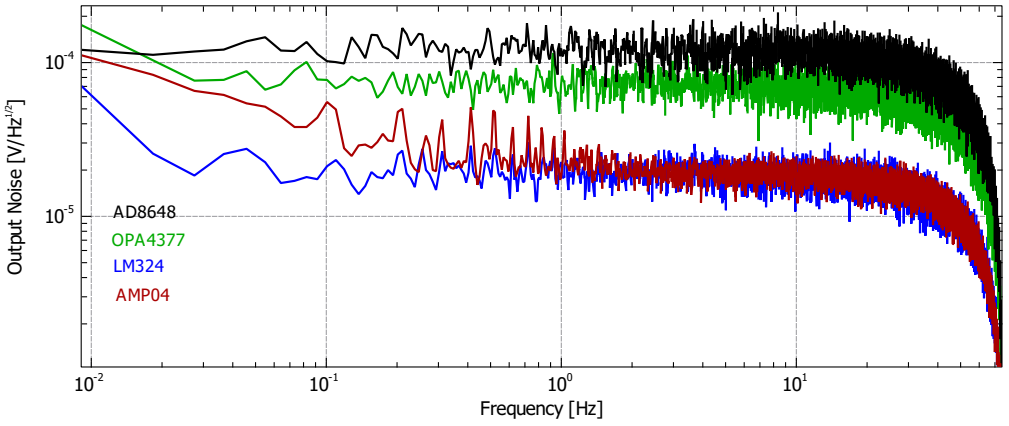

FIGURE 3.20: Noise comparison of Low-cost classical amplifier with an instrumentation one (AMP04).

As discussed earlier, during the fabrication the permalloy layer is deposited in a strong magnetic field to generate the easy axis of the sensor and to align the magnetic domains. This process creates the anisotropy field (H_k), and consequently the sensitivity and non-linearity specifications for the sensor. According to Equation (3.13), a greater value of H_k (compared to H_x and H_y), provides more linear response (Equation (3.14)) and, in contrast less sensitivity for the sensors.

For typical AMR sensor, the bandwidth is in the range of $DC-5MHz$ and its resolution is limited to the noise level of the AMR Wheatstone bridge. This noise is caused by the contribution of the resistance thermal noise ($4kTR\Delta f$), and a Barkhausen noise that happens by changing the size and direction of the magnetic domains ($\approx 4pT/\sqrt{Hz}$ in the best case) (see [13]). We refer to Figure 3.21 from [64] to exhibit the noise level of some available AMR sensors. Note that, the typical sensor sensitivity for HMC1021 and HMC1001 from Honeywell is $1mV/V/G$ and $3.2mV/V/G$ respectively, and similarly, $1.2mV/V/G$ for KMZ51 from Philips.

The results show that because of lower noise density of HMC1001 and its higher sensitivity compared to others, it has better equivalent magnetic noise behavior. Moreover, driving the AMR bridge with more value of supply will increase the signal to noise ratio of the sensor at higher frequencies and, then, will reduce the thermal noise level. According to [64], noise level of HMC1001 with a bridge voltage of 10 V is lower than $50pT/sqrtHz$ in 10-100Hz frequency range. The same result has been reported by using a bridge voltage of 24 V and resolution of $20pT/sqrtHz$ at 100 Hz (see [56]).

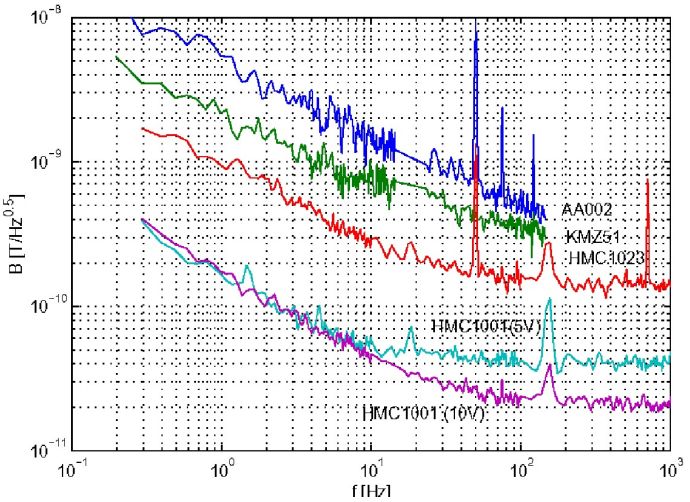

FIGURE 3.21: Comparison of equivalent magnetic noise for different magnetoresistive sensors. $KMZ51$ (AMR type), from Philips; $HMC100X$ and $HMC102X$ (AMR type), from Honeywell; and $AA002$ (GMR type), from NVE

Chapter 4

Calibration algorithm and sensor error modeling

4.1 Vector magnetometer error modeling

The microelectromechanical systems (MEMS) type magnetometer is commonly used nowadays in many applications. Inertial navigation systems use a magnetometer as a digital compass for heading, with the combination of the accelerometer and the gyroscope. However, these sensors have drawbacks in terms of noise, different sensitivities, bias drift and nonlinearity response. Hence, much research and additional efforts have been devoted to enhancing the performances of motion sensors such as accelerometers, gyroscopes, magnetic sensors and barometers. Signal processing, estimation algorithms, special electronic design and sensor calibration can be mentioned. Compared to other motion sensors, calibrating the DC magnetometer needs more effort and experiences because this process is always subject to perturbation of the magnetic field.

Several methods and algorithms have been proposed for calibrating magnetometers. Most of them have the same fundamental and use a scalar calibration algorithm that needs to rotate the magnetometer in all possible directions in a constant uniform magnetic field [65], [66], [67], [68], [69].

Generally, the main source of errors can be separated into two categories: those caused by disturbances in the magnetic fields surrounding the sensor, and those due to the manufacturing defects and limitation in the sensors. These errors for three-axis sensors are detailed below.

4.1.1 Scale factor

Even by assuming that the same process fabricates the triple axis magnetometers, in reality they still have different specifications. Scale factor error relates to the different sensitivities of each magnetometer to an identical magnetic field. To give an example we can refer to the three-axis magnetometer from Honeywell (HMC100X): they are made by the same process and materials, but in our experience, the one that contains a single AMR element (HMC1001) always has a different sensitivity than the one in two-axis.
In order to calibrate the scale factor error, a well-known magnetic field in terms of magnitude and direction should be applied to the sensor. In this case, the errors will be compensated to the same value, corresponding to an applied magnetic field. Meanwhile, since the magnetometer needs an electronic design for amplification, this error may partly arise as a consequence of the gain errors, mismatch resistors, etc.
For a three-axis magnetometer, scale factor error can be represented as a diagonal 3×3 matrix:

$$S_f = \begin{pmatrix} S_{fx} & 0 & 0 \\ 0 & S_{fy} & 0 \\ 0 & 0 & S_{fz} \end{pmatrix} \tag{4.1}$$

Note that another origin of the scale factor error depends on how the sensors are supplied. Using a supply for three parallel AMR bridges may result in different currents for each axis and thus different sensitivities. Moreover, the total bridge resistance of each axis must be constant regardless of the magnitude of the applied field. However, in reality this is not the case and it may change for a few ohms, which then causes the non-linearity of the scale factors. Hence, for better performances, each AMR bridge should be supplied separately (see Figure 4.1). In addition, if the temperature and consequently the resistance varies between the bridges, for each bridge the current does not remain constant and another non-linearity problem will appear.

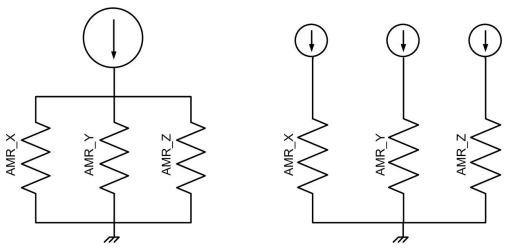

FIGURE 4.1: Schema of different types of supplying a three axis sensor. Right, by using a single current source for three axis sensor and left by using a current source for each sensor axis.

4.1.2 Misalignment error

This error occurs when the three-axis magnetometer does not have a perpendicular position to each other. Commonly, this error happens with the sensor installation and soldering into the circuit board. However, it may also happen for a compact three-axis sensor due to the housing error during the fabrication. This error is also called "non-orthogonality error" and it can be modeled by a 3×3 upper-triangular matrix on the magnetometer reading.

$$S_m = \begin{pmatrix} 1 & \alpha & \beta \\ 0 & 1 & \gamma \\ 0 & 0 & 1 \end{pmatrix} \tag{4.2}$$

4.1.3 Soft iron error

In general, materials that have a high permeability such as ferromagnetic, are able to attract magnetic lines of flux. In other words, they can generate a magnetic field as a function of the external field. Consequently, if an externally applied field exists, then these materials change the uniformity of it by concentrating the magnetic field lines without adding any extra field to the total value of the applied field. Therewith, they will be neutral while the externally applied field disappears.
This is also the reason why this material is called soft-iron. The soft iron effect is complex, nonlinear and depends on the direction and magnitude of the applied field. It is also the most common error and problem of calibrating the magnetometers.
Ideally, by assuming a free perturbation applied magnetic field, the sensor reading should be a circle centered on the zero coordinates, rotating in the field plain. However, due to the mentioned error and because of distortion of the magnetic field in a vicinity of the soft iron material, the circle deforms to produce an ellipse (see Figure 4.2).
Due to the sensor movement in the magnetic field, the soft iron error for the strapdown systems can be compensated for those soft iron materials that are only installed on the sensor board. In contrast, for those materials that are external, compensating the distortion effect is not possible. Figure 4.3 illustrates a typical simulation result of the soft iron error on the sensor reading. The soft iron material, such as the connector on the PCB, perturbs the uniformity of the magnetic field. However, since they rotate with the sensor, the sensor reading changes to an elliptical shape. The soft-iron error can be

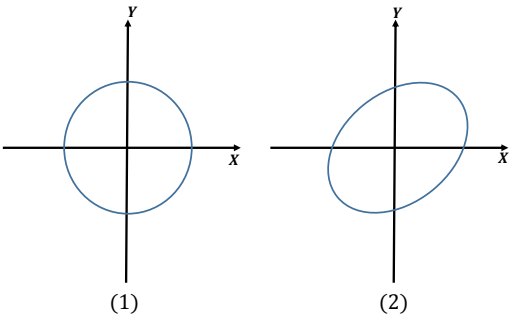

FIGURE 4.2: The profile of the magnetic field due to the soft iron effect presented in (2) and (1) shows the sensed magnetic field without the soft iron effect.

modeled as a 3x3 full rank matrix on the magnetometer reading.

$$S_{si} = \begin{pmatrix} \psi_{xx} & \psi_{xy} & \psi_{xz} \\ \psi_{yx} & \psi_{yy} & \psi_{yz} \\ \psi_{zx} & \psi_{zy} & \psi_{zz} \end{pmatrix} \tag{4.3}$$

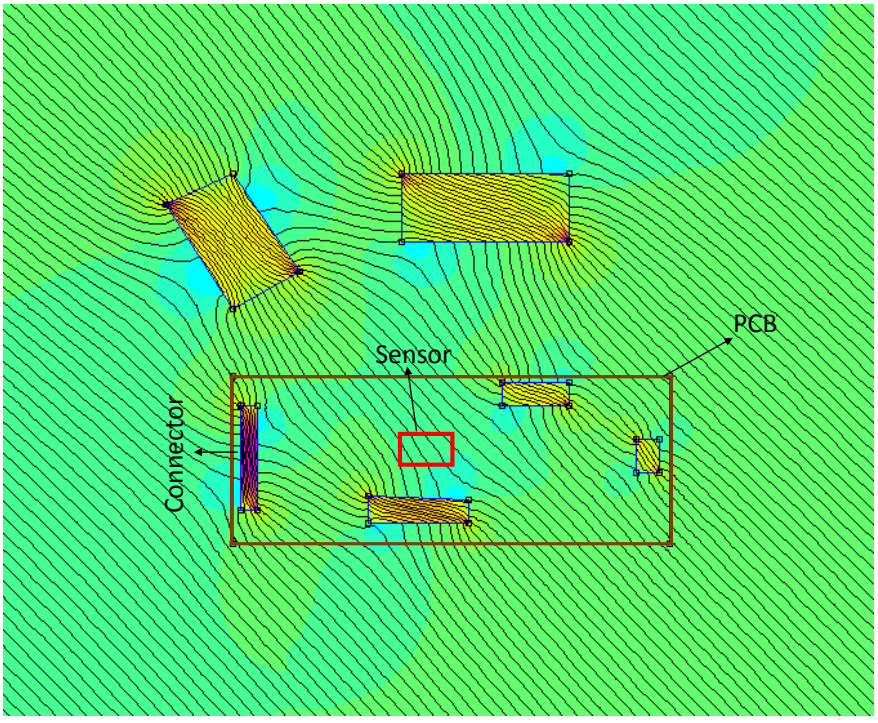

FIGURE 4.3: Simulation result of the magnetic field perturbation proximate to the ferromagnetic materials.

4.1.4 Hard iron error

Hard iron error relates to a permanent magnet that is fixed in the proximity of the sensor frame. Contrary to the soft iron error, in this case, a permanent magnet generates a constant magnetic field regardless of an externally applied magnetic field. Consequently, even if the applied field is null, the sensor measures this additive magnetic field vector (see Figure 4.4). For this functionality, the corresponding error is the so-called "hard-iron" effect. The hard-iron effect acts directly on sensor bias measurement and it can

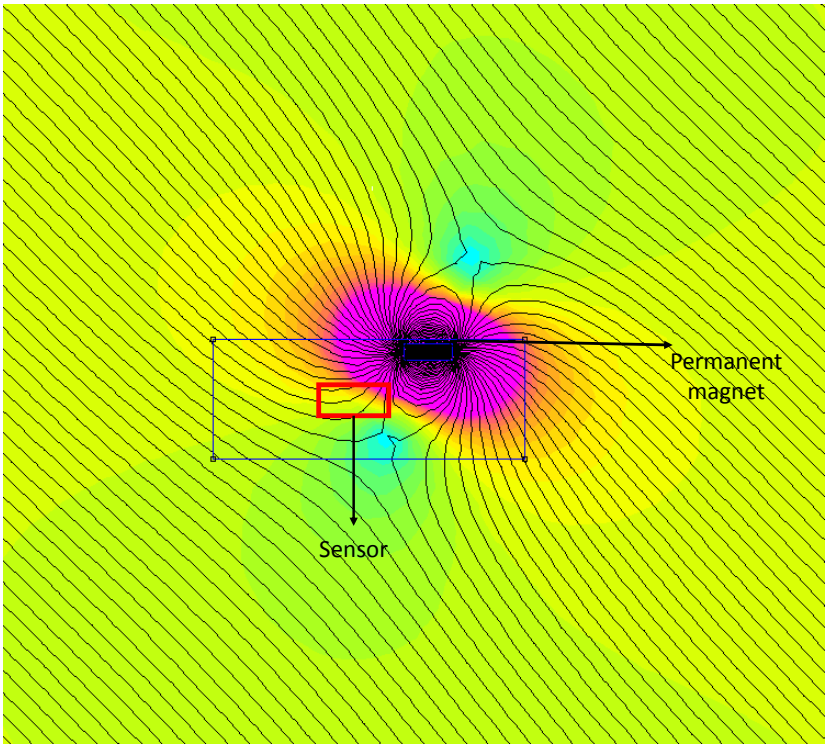

FIGURE 4.4: Simulation result of the magnetic field perturbation proximate to the ferromagnetic materials.

be compensated much more easily than the soft-iron effect. Considering the deforming of the sensor reading error due to the soft-iron material, the hard-iron materials do not deform the shape of the sensor reading. Due to this error, the field sensed by the magnetometer will be a circle with a shifted center (see Figure 4.5). The most common sources of this error are speakers in cell phones, mini DC motors and constant current carrying wires.

The hard iron effect can be modeled as a constant 3x1 vector as follows:

$$B_{hi}^{T} = \begin{pmatrix} b_{hx} & b_{hy} & b_{hz} \end{pmatrix} \tag{4.4}$$

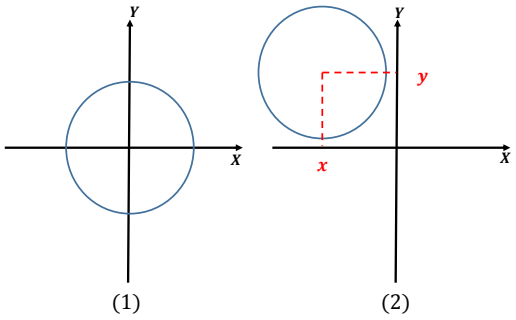

FIGURE 4.5: The profile of the magnetic field due to the hard iron effect presented in (2) and (1) shows the sensed magnetic field without the hard iron effect.

4.1.5 Sensor bias

Sensor bias is caused by the Wheatstone bridge offset in MR magnetometers. Since the Earth's magnetic field is everywhere and it can be perturbed easily by other sources of the magnetic field such as the effects mentioned above, the sensor bias is difficult to identify. An expensive multilayer shielding box, with a desire attenuation factor for canceling the external magnetic field, is perhaps the most accurate method to calculate the sensor bias. In this case, since the residual of the field is zero inside, the sensor reading will be the offset itself. Some other methods also propose canceling the Earth's magnetic field using a Helmholtz coil. Here, the Helmholtz coil provides a reverse magnetic field proportional to an external magnetic field to cancel it out and produce a region with the zero field inside [70].
As reported earlier in Chapter 3, recently, AMR sensors have been equipped with an internal coil periodically to excite the permalloy layers with a strong magnetic field. While, the main aim of using this method (flipping method) is to keep the sensor sensitivity at its best performance, this method additionally maintains the sensor bias constant at a constant temperature for the entire life of its operation.

4.2 Calibration process

Thus far, the different errors of the magnetometers (especially low cost sensors) have been described. We now go into further detail about how these errors can be formulated, and then how they will be estimated to compensate the sensor measurement.
In order to formulate the overall calibration error model of the magnetic sensor, we

compile all the matrices in the following equation:

$$H_k = A.h_k + B \tag{4.5}$$

Where A, is the combination of misalignment, soft iron and scale factor errors; B is the combination of the hard iron errors, misalignment and sensor bias; k is the number of sample measurement; h (3×1 vector), is the three-axis un-calibrated sensor measurement and H (3×1 vector), is the real value of the magnetic field after the calibration. The matrices of A and B are defined using Equation (4.1), (4.2), (4.3), (4.4) respectively as 3×3 matrix and 3×1 vector as below:

$$A = S_f S_m S_{si} \tag{4.6}$$

and by introducing B_s as a sensor bias in a zero magnetic field:

$$B = B_s + S_f S_m B_{hi} \tag{4.7}$$

Therefore, now the calibration problem consists in estimating the two general matrices. However, in order to solve the linear model of the magnetometer, an external reference is needed to compare the sensor reading.
A considerable amount of literature has been published on magnetometer calibration algorithm. All methods rely on the fact that the total magnetic field that is sensed by the sensor is constant. This method is also called scalar calibration or scalar checking. In a perturbation free environment, the norm of the magnetic field is constant and equal to the magnitude of the field. This magnitude can be found from the geomagnetic model [71].

$$h_{tot}^2 = h_x^2 + h_y^2 + h_z^2 \tag{4.8}$$

where h_{tot} represents the norm of the magnetic field measured by the three-axis sensor. From Equation (4.5) we can write:

$$H_k = A(h_k - b) \tag{4.9}$$

where $b = -A^{-1}B$. Assume that the magnetic field norm sensed by a perfect sensor ($\|H_k\|$) is equal to a constant (K),

$$\| H_k \|^2 = H_k^T H_k = (A(h_k - b))^T (A(h_k - b)) = K^2 \tag{4.10}$$

this equation can be expanded to

$$\| H_k \|^2 = h_k^T A^T A h_k - h_k^T A^T A b - b^T A^T A h_k + b^T A^T A b \tag{4.11}$$

by defining a new parameter

$$D = A^T A = D^T \tag{4.12}$$

then we can write

$$h_k^T A^T A b = h_k^T D b = h_k^T (b^T D^T)^T = b^T D^T h_k \tag{4.13}$$

Therefore, the Equation (4.11) can be defined as:

$$f(h_k, D, b) = h_k^T D h_k - 2 h_k^T D b + b^T D b \tag{4.14}$$

Based on two-step calibration algorithm [67], if a three axis sensor rotates in the perturbation free magnetic field, ideally, the magnetic field sensed by the sensor is located on a spherical shape. However, this is not the case for the low cost magnetometer due to the aforementioned errors. Indeed, the sensor reading can be considered as an ellipsoid. Consequently, it is sought to determine the matrix A and the vector B to transform and compensate the sensor reading to a spherical shape. Since the sensor needs to be rotated in a constant magnetic field, the matrix A consists of a rotation matrix as well.

$$A = R.S \tag{4.15}$$

For any rotation matrix we then have $R^{-1} = R^T$, therefore,

$$R R^T = R^T R = I \tag{4.16}$$

consequently,

$$D = A^T A = (RS)^T (RS) = S^T (R^T R) S = S^T S \tag{4.17}$$

In other words, from Equation (4.17) and Equation (4.14), we can observe that there are infinite solutions for matrix A. To overcome this problem, we address to use the Cholesky decomposition solution to find a unique upper triangular matrix after leaving out any rotation matrix. Then, this change will be defined by the new following matrices :

$$L = \begin{pmatrix} L11 & L12 & L13 \\ 0 & L22 & L23 \\ 0 & 0 & L33 \end{pmatrix} b' = \begin{pmatrix} b1 & b2 & b3 \end{pmatrix} \tag{4.18}$$

Now, by substituting the new parameters in Equation (4.14) and considering the quadratic

form of ellipse equation [72], a two-step calibration algorithm using a least squares method, can be performed to estimate the matrix elements in Equation (4.19)[1].

$$(L, b') = \underset{A,B}{\operatorname{argmin}} \sum_{k=1}^{n} (f(h_k, L, b') - 1))^2 \tag{4.19}$$

Finally, the calibration data from the sensor measurement can be extracted by using Equation (4.20),

$$H_k = L(h_k - b') \tag{4.20}$$

Another approach to the calibration algorithm is suggested in [73] by following the same idea of a two step calibration algorithm. However, in this case, the cost function has been developed considering the Equation 4.5, as follows:

$$(A_{i+1}, B_{i+1}) = \underset{A,B}{\operatorname{argmin}} \sum_{k=1}^{n} \|(A_i h_{k,i} + B_i) - \frac{h_{k,i}}{\|h_{k,i}\|}\|^2 \tag{4.21}$$

which first converts a quartic cost function in Equation (4.19) to quadratic form. Then, to extract the general matrix of A and B, an iteration method is used to update the equations and estimate the calibration parameter recursively. Note that here i represents the number of iteration steps.
In this case, for each step, Equation (4.22) is used to determine the new vector of h_k of a sequence, using the preceding matrix of A and vector of B.

$$h_{k,i+1} = A_{i+1} h_{k,i} + B_{i+1} \tag{4.22}$$

Then this new data will be replaced again in Equation (4.21) to update the calibration parameters. Finally, the calibration parameters will be obtained after i such iterations. According to what is discussed in this article, using this iteration method solves a sequence of equations with a least square method in order to calibrate each step and finally provide the better calibration parameters compared to the previous method.
Figure 4.6 shows the comparison between calibrated and un-calibrated measurement of the total magnetic field with this calibration algorithm while the sensor has rotated in a perturbation free Earth's magnetic field. Moreover, Figure 4.7 shows the results of the sensor reading where both the calibrated measurement as well as the un-calibrated one are plotted in 3D.

[1] $\underset{x}{\operatorname{argmin}} f(x) := \{x \mid \forall y : f(x) \leq f(y)\}$

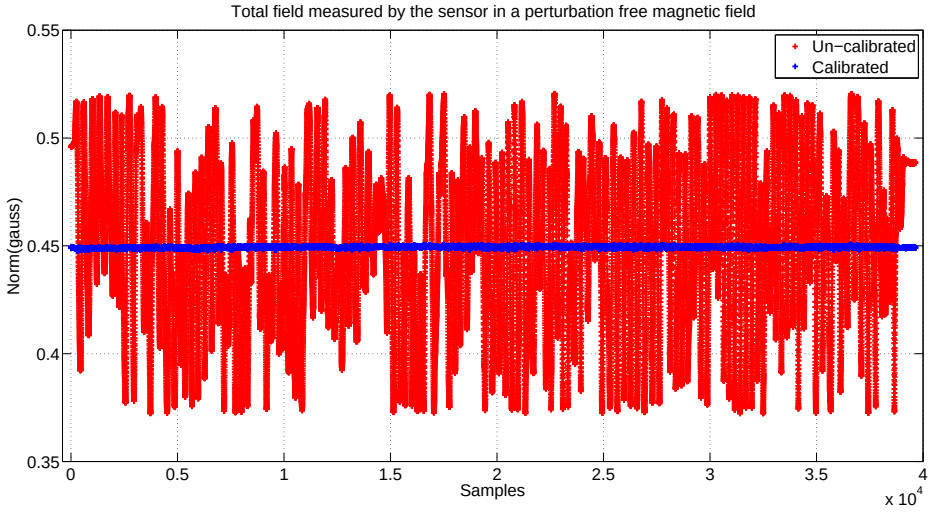

FIGURE 4.6: Norm of magnetic field sensed by the three-axis sensor (HMC100X),while it rotated in a perturbation free Earth's magnetic field. Blue color represents this norm after sensor calibration and the red color represents that for the un-calibrated sensor. Note that the norms of residuals of un-calibrated and calibrated sensor are 7.9971 and 0.07311 respectively.

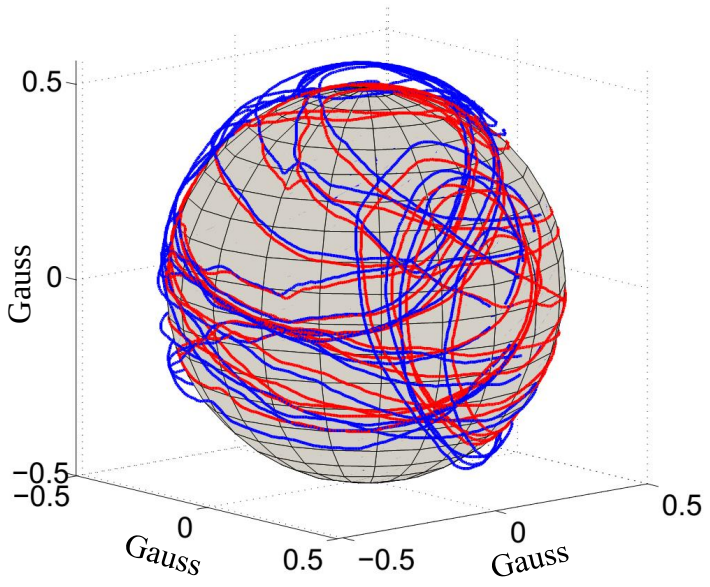

FIGURE 4.7: Spherical shape representing the surface that the magnetic field is expected to be located on it. Blue color shows the magnetic field sensed by an un-calibrated sensor and the red shows the corrected result using the calibration algorithm.

Chapter 5

Novel compensation method of the cross-axis effect

5.1 Introduction

As stated earlier in chapter 3, the cross-field effect is a nonlinear error that happens to all magnetoresistance sensors. Based on Equation (5.1) (by rewriting from Equation (3.13)), this effect can be characterized by H_x, corresponding to a perpendicular field compared to the sensitivity axis of the AMR Bridge.

$$V_{out} = a\frac{H_y}{H_k + H_x}\sqrt{1 - (\frac{H_y}{H_k + H_x})^2} \tag{5.1}$$

Furthermore, from another point of view, the cross-field depends on H_k from one side and then on the magnitude of the applied field H_y in the sensitive direction from the other side. Once H_y is zero for an AMR sensor, the cross-field is zero as well.

For the navigation applications where the magnetometer is used as an electronic compass, the cross-field effect may cause a significant error on the sensor reading. Figure 5.1 indicates simulation results based on Equation (5.1), when the sensor is rotated in the magnetic field. Since the compass needs two or three sensors orthogonal to each other, this error becomes serious when one or more axes are in minimum field condition and the other axis senses the majority of the field strength. In this figure, the red plot illustrates the error contribution of the two axis sensor reading with anisotropy field (H_k) of 8 Gauss, when it is rotated in a field of one Gauss.

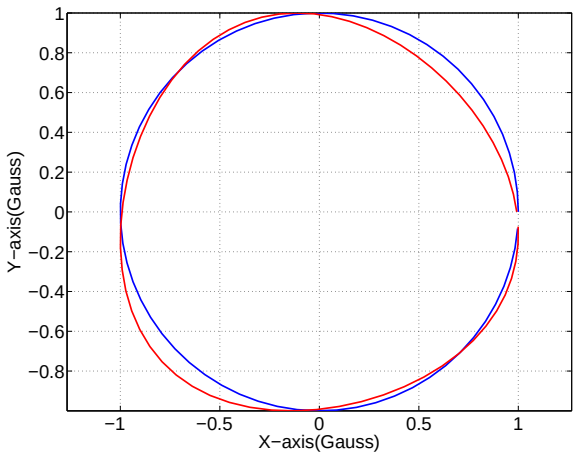

FIGURE 5.1: Simulation results of sensor rotation in 360 °. The blue color represents an expected measurement by error free sensor; and the red shows the effect of the cross-field error in the real sensor measurement..

To date various methods have been developed and introduced to compensate the cross axis effect, especially for the AMR sensor, and each has its advantages and drawbacks. Basically, these methods can be divided into three categories: those that need to have an additional electronic design and techniques [74][75][62][61][60], those that depend on the sensor fabrication process and those that are based on auxiliary measurement and numerical computation to compensate this error [76][75]. Below we detail the drawbacks and advantages of these methods.

5.1.1 Methods using additional electronic design

5.1.1.1 Flipping method

Flipping or set/reset method can be considered the most practical for effectively suppressing the cross-field error. This method has been explained in chapter 3. Recently, most of the AMR sensors have been equipped with internal packaging coils to refresh the magnetic domains and change their anisotropy direction. A low cost and simple RC circuit with the contribution of switching transistor design is able to drive enough current pulse for several AMR sensors at the same time. However, this mentioned method suffers from power consumption limitations, which increases with the frequency as well (See Figure 3.15).

5.1.1.2 Feedback loop

Let us now consider the measurement in x or (y) direction. As discussed above, the cross-field effect depends on the magnitude of the external field (H_y). To investigate this effect, Equation (5.2), which represents the variation of the sensor output due to the cross-field effect, can be written from Equation (5.1):

$$d(V_{out})/d(H_x) = -a\left(\frac{H_y^3}{(H_k+H_x)^4\left(\sqrt{\frac{H_y^2}{(H_k+H_x)^2}+1}\right)} + \frac{H_y\sqrt{\frac{H_y^2}{(H_k+H_x)^2}+1}}{(H_k+H_x)^2}\right) \tag{5.2}$$

Furthermore, Figure 5.2 illustrates the simulation results of this equation due to the different magnitude of an applied (H_y) and a perpendicular (H_x) magnetic field. According

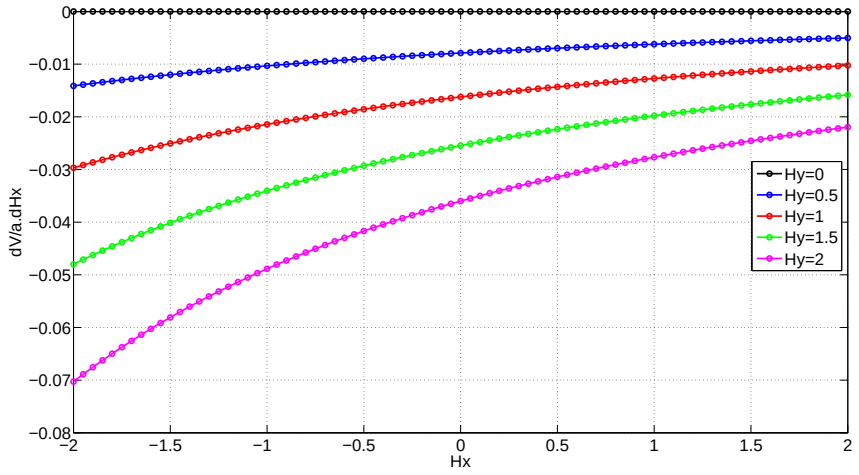

FIGURE 5.2: Sensor's output variation due to a cross-field (H_x) for different applied fields (H_y).

to these results, a greater value of H_y causes higher cross-field error on sensor measurement. Therefore, this exactly explains why the feedback loop suppresses the cross-field error. The feedback loop provides the magnetic field in a reverse direction compared to an external field; thus, the equivalent vector of the magnetic field reduces to zero or the sensor operates in more linear region of its range. Consequently, H_y can be substituted by zero, following Equation (5.1).

By considering Equation (5.1), however, compensation of the cross-field error using the feedback loop entails the drawback of dynamic power consumption as well. Meanwhile, this disadvantage also depends on the field that is generated by the offset strap as a function of the current and the resistance value. Table 5.1 in below characterizes the additional power dissipated due to the implementation of the feedback loop for some of the available sensors when they are exposed with one Gauss magnetic field.

Other problems with this approach that can be noted are: more circuit complexity, less

	Offset strap resistance	Current field applied	Power(mW)
HMC1001	1.5 Ohm	50mA/Gauss	3.8
HMC1021	8 Ohm	5mA/Gauss	0.2
KMZ51	170 Ohm	4mA/Gauss	2.7

TABLE 5.1: Power dissipated using feedback loop for different AMR sensors.

frequency response and cost.

Note that this additional power requirement is for the sensor itself, and it could be much higher with the participation of other components such as amplifiers. In this case, suppose we have an amplifier to provide the current feedback for the offset strap in its output. Thus, if this amplifier is supplied with V_{cc}, then the power dissipation is $P = V_{cc}.I_{feedback}$.

5.1.2 Sensor fabrication process

The fabrication process and sensor shape will also create different sensor specifications. Indeed, one main parameter is the anisotropy field that is created by depositing the thin film Permalloy layers in a strong magnetic field. Turning back to Equation (5.1), it is apparent that by increasing H_k, the effect of cross-field error will be reduced and the linearity response of the sensor will be improved. Although, on the other hand the sensitivity will be reduced (see Figure 5.3).

Due to this reason, several different available AMR sensors exist today for covering

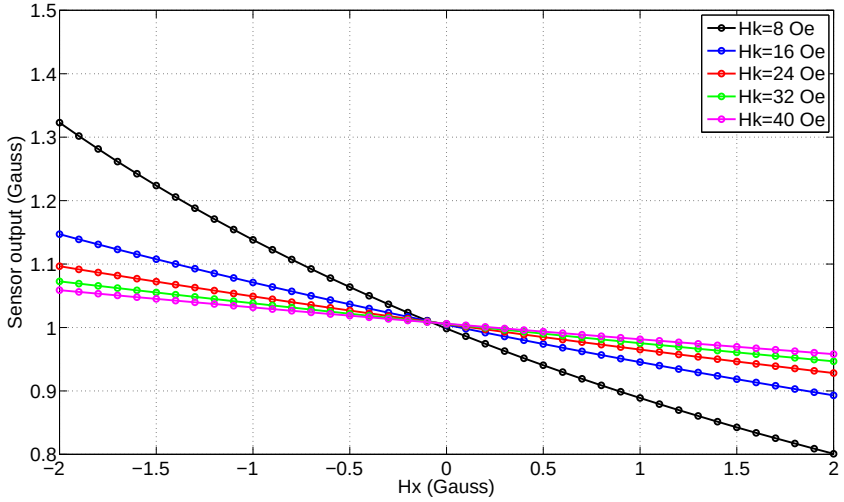

FIGURE 5.3: Error in the sensor measurement due to the cross-field effect (H_x) for different anisotropy fields. Note that applied field is one Gauss ($H_y = 1G$)

different applications. For instance, although HMC100X can be considered the most

sensitive commercially available AMR sensor to detect the Earth's magnetic field, but for low cost inertial navigation systems HMC102X and HMC1051 are a better choice because of their much better linearity response and lower cross-field errors. Note that compared to HMC1001, HMC102X and HMC105X have a bigger anisotropy field (H_k).

5.1.3 Methods using numerical computation

A considerable amount of literature has been published on the numerical compensation of the cross axis effect. These studies are based on gathering data of sensor measurement on several different points and situations.
In [57], a cross-field compensation method has been explained for two axis sensor typically by using a Helmholtz coil set and non-magnetic rotation platform (see Figure 5.4).

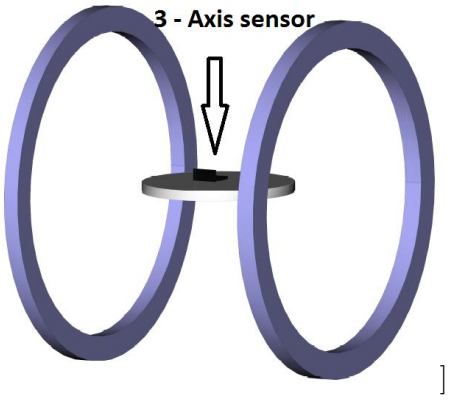

FIGURE 5.4: Schematic view of sensor putting on the non-magnetic rotation disc inside the Helmholtz coil.

In this case the sensor should be rotated in at least four different precise orientations compared to the Helmholtz coil axis to provide enough data for solving the equations that contain cross-field parameters.
Another method [77] that has been proposed to compensate the cross-field error is that of assuming that three such AMR sensors are mounted orthogonally to each other. In this case a well-known magnetic field is needed to provide and then compare with the sensor measurement. Thus, the sensor reading will be corrected numerically by using an iteration method. However, in order to use this method one needs to have a knowledge of the anisotropy field (H_k).
Another study [76] has considered analyzing a compensation method for three axis sensors when they have the orthogonality error as well. However, in this article a scalar magnetometer is used as a standard reference to compare with the AMR sensor measurement when it rotates in a non-magnetic rotation table. In addition, Newton-Raphson

iteration method is used to calculate the compensation parameters.

This chapter discusses a new method for compensating the cross axis effect. We investigate the behavior of the AMR sensors and propose an effective method to compensate for the cross-axis error for the three-axis magnetometers. This method does not depend on other instruments to provide and measure the magnetic field; it does not even use any other precision sensor. In this case, the cross-axis compensation parameter is obtained solely by rotating the sensor arbitrarily in a perturbation free Earth's magnetic field. Meanwhile, it is not important to know the magnitude of the magnetic field or the Earth's magnetic field for finding the compensation parameters.
In chapter 4, we have introduced the calibration algorithm for three axis magnetometers. This algorithm is based intrinsically on estimating the linear model of equations that are generally, so called two-step estimation algorithms. The first aspect to point out is that we can use this intrinsic specification to identify the non-linear response of the sensor such as the cross axis error.
In this study, we use the algorithm to examine the sensors for two configurations. First, we analyze the original data of the sensors without implementing flipping method and then calibrate the sensors. Next, we compare the calibration results with the compensation methods. Further, we perform this test for sensors that are used in the flipping mode. Subsequently, we show the calibration results with the proposed method.
Before any further explanation of the new compensation method, we present the simulation results of the cross-field effect on the sensor calibration norm. The simulation data has been created similar to the sensor rotation in the Earth's magnetic field (see Figure 5.5).

Now, assume there are two sensors with different anisotropy field characterizations. As mentioned before, the one that has a lower anisotropy field has better sensitivity but also a bigger error and cross-field effect on its measurement. Consequently, we chose a sensor with $H_k = 8$ Gauss, which is comparable to the one that used in our experiment in section 5.3, and the second with $H_k = 20$ Gauss. Moreover, for both sensors, the calibration norm has been computed by using the flipping method and for the normal sensor operation. These results in Figure 5.6 show that, as the cross-field effect is the non-linear error in the sensor measurement, the calibration norm has a distortion from the norm of one in case of the ideal sensor. Meanwhile the sensor that has less effect to this error, offers better residual norm of calibration. In other words, these findings suggest that the calibration norm can be considered as a criterion for evaluating the sensor performance.

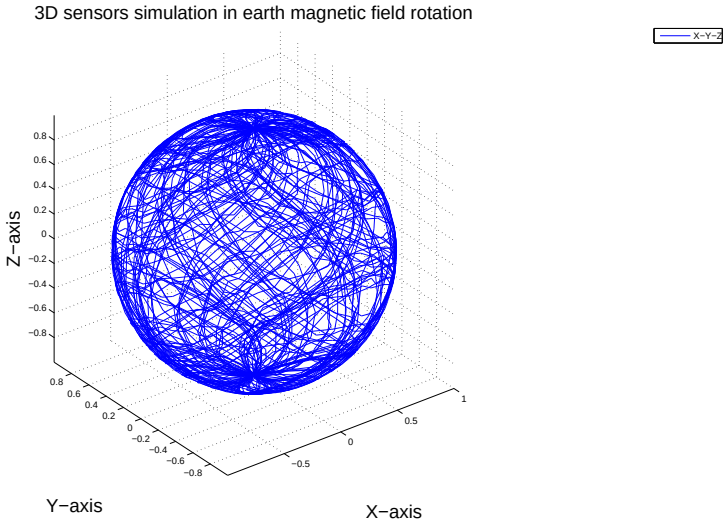

FIGURE 5.5: Three-dimensional representation of the simulation results of sensor rotation in a constant magnetic field.

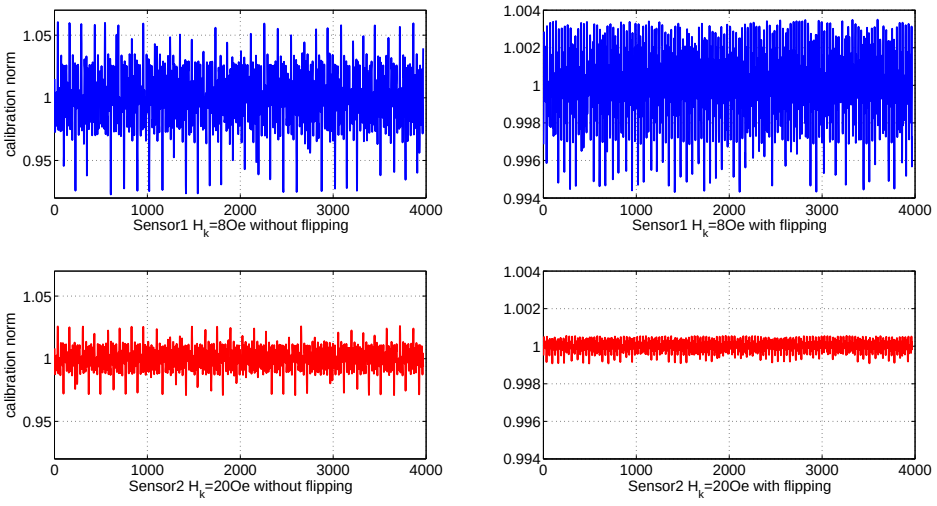

FIGURE 5.6: Simulation results of two different sensors rotated in the Earth's magnetic field. Blue color represents the calibration norm for a sensor with anisotropy field of 8 Oe in a normal operation on the left and with the flipping method on the right. The red color is similar to the blue one, except the anisotropy field is 20 Oe.

5.2 Numerical compensation method of cross axis in Earth's magnetic field.

This part attempts to obtain simple equations to compensate the cross-field errors. These new forms of equations will be proposed for use in two different situations while the AMR sensor output is modulated by the set/reset method and while it is directly used. In both cases the equations will be simplified by eliminating the parameter a, which refers to sensor sensitivity in Equation (5.1) [78].

5.2.1 Compensation method without flipping.

By assuming that

$$\Gamma = \frac{H_y}{H_k + H_x}$$

Equation (5.1) becomes

$$V_{out} = a\Gamma\sqrt{1-\Gamma^2}$$

Then also yields

$$V_{out} = a\Gamma\sqrt{1-\Gamma^4}/\sqrt{1+\Gamma^2} \tag{5.3}$$

Now, by using the following approximation [1]:

$$\sqrt{1-\Gamma^4} \approx 1$$

Thus, Equation (5.3) will be simplified, and can consequently be rewritten as follows:

$$V_{out}^2 = \frac{a^2 H_y^2}{((H_k + H_x)^2 + H_y^2)} \tag{5.4}$$

It should be noted that a and H_k are constant values. Now, let us imagine an AMR sensor without cross-axis error. This ideal AMR sensor would have an output voltage that is not dependent on the cross-field ($H_x = 0$). Therefore, Equation (5.4) changes to Equation (5.5):

$$V_{out-ideal}^2 = \frac{a^2 H_y^2}{(H_k^2 + H_y^2)} \tag{5.5}$$

Now, in order to eliminate sensitivity from Equation (5.5), a is eliminated by dividing Equation (5.5) by Equation (5.4):

$$\frac{V_{out-ideal}^2}{V_{out}^2} = \frac{a^2 H_y^2((H_k + H_x)^2 + H_y^2)}{a^2 H_y^2(H_k^2 + H_y^2)}$$

[1] instead of $\sqrt{1-\Gamma^2} \approx 1$ which is classically used.

Then:

$$V_{out-ideal} = \sqrt{\left[\frac{V_{out}^2((H_k + H_x)^2 + H_y^2)}{H_k^2 + H_y^2}\right]} \tag{5.6}$$

5.2.2 Compensation method using flipping.

When the set/reset or flipping method is implemented, the output signal (V_{outSR}) is an average value for each magnetization direction (with respect to V_{SET} and V_{RESET}).

$$V_{outSR} = \frac{V_{set} - V_{reset}}{2}$$

The linear part of Equation (5.1) has been chosen to simplify the equation, so V_{outSR} can be written by considering H_k and $-H_k$ for SET and RESET respectively.

$$V_{outSR} = \frac{aH_y}{2}\left[\left(\frac{1}{H_x + H_k}\right) - \left(\frac{1}{H_x - H_k}\right)\right] \tag{5.7}$$

Here, similar to the linear measurement of the sensor without cross-field described in the previous section, Equation (5.7) changes as follows:

$$V_{outSR-ideal} = \frac{aH_y}{2}\left[\left(\frac{1}{H_k}\right) + \left(\frac{1}{H_k}\right)\right] \tag{5.8}$$

As also similar to the previous method for finding Equation (5.6), by dividing Equations (5.7) and (5.8), the compensation value can be expressed as follows:

$$V_{outSR-ideal} = \frac{V_{outSR}(H_k^2 - H_x^2)}{H_k^2} \tag{5.9}$$

5.3 Experimental result

5.3.1 Sensor board

This section describes the manner in which the compensation method is examined in the Earth's magnetic field. An AMR sensor is used to measure the Earth's magnetic field in 3-D; thus HMC1001 and HMC1002 from Honeywell, having a resolution of 2.7 nT, sensitivity of 160 V/T and supply of 5 V are selected. HMC1001 has an appropriate size and structure for measuring the orthogonal field such as Z-axis, whereas HMC1002 is suitable for measuring the X and Y-axes. The differential output of a sensor for each bridge of sensors is amplified by a low noise instrument amplifier (Gain = 66.6) and 2.5 V is added to the output signal as reference voltage. The digital part incorporated by 3 Delta-Sigma ADCs with 16-bit resolution and the microcontroller from PIC family is

used to launch ADCs, to make the average of the signal in each period of set/reset and to transfer the data by RS232 port. The set/reset pulses are generated using an H-Bridge circuit by containing MOSFET transistors for switching a 3-A current in two opposite directions inside the flipping coil. However, the H-bridge circuit can be supplanted by half-bridge circuit and a capacitor. The duration time for each SET and RESET pulse is 8 μs, delay time for reading the analog signal using the ADCs is 100 μs, and ADC sampling rate is 125 samples per second. Figure 5.7 shows a photograph of the circuit design that is used here.

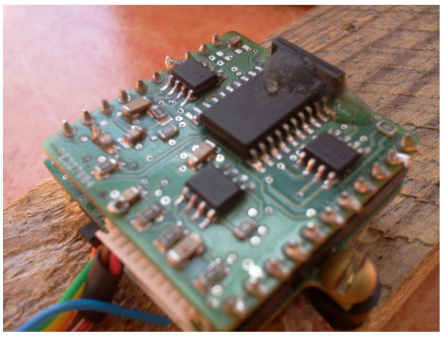

FIGURE 5.7: Three-axis magnetic sensor board (HMC1001 for Z-axis & HMC1002 for X and Y-axes).

It should be noted that the magnetization vector ($\overrightarrow{M}$) or sensitive direction of the sensor must be determined for each axis in normal sensor operation (without flipping) to identify the sign of the parameters in Equation (5.6). Figure 5.8 shows the direction of the sensitivity in a sensor's packaging (given in the datasheet [79]), although it is possible that the sensors have a reverse direction for the sensitivity. This direction is related to the last set or reset pulse that, occurred inside the flipping coil. In fact, if the sensor operating in the set/reset mode is deactivated, the vector direction depends on the last operation.

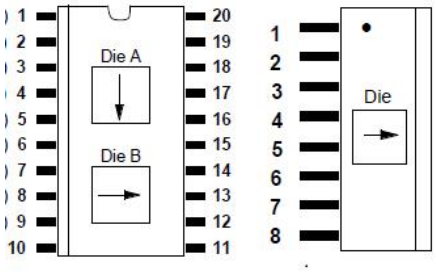

FIGURE 5.8: Package drawing for HMC1001 and 1002 showing the sensitive direction for each axis.

5.3.2 Scale factors

Equation (5.6) has been proposed to compensate the cross-axis error, but is still not in the complete form. As already mentioned for the proposed method, measuring the magnitude of the magnetic field is not necessary. The calibration algorithm, obtains the compensation parameters by comparing the norm of calibration results. In this case a parameter is required to be added to Equation (5.6) for computing the compensation magnetic field that is measured by the sensor. Scale factors α , β, and γ are defined for each axis for adapting the correction to the discrepancies between the sensors. These parameters enable us to consider slight differences in the sensitivities of each axis to orthogonal fields related to the different values of anisotropy field in the datasheet comparing with the real values for sensors X, Y and Z. Therefore, Equation (5.6) changes to Equations (5.10), (5.11) and (5.12) for a three axis sensor. The other point that should be mentioned here is to find the output of the sensor with its axis coupled with another axis. Assume that the three axis sensors are mounted orthogonally to each other, as shown in Figure 5.7. In this case the X sensor (Die A) in Figure 5.8 is mounted in the X-Y plane, Y sensor (Die B) in the Y-X plane and Z sensor (Die C) in the Z-Y plane. According to the position of each AMR bridge the output of X sensor depends on the Y field for cross-field, and respectively Y sensor depends on X field and Z sensor depends on Y field.

$$V_{out-ideal(x)} = \sqrt{\left[\frac{V_{outx}^2((H_{kx} + \alpha H_y)^2 + H_x^2)}{H_{kx}^2 + H_x^2}\right]} \tag{5.10}$$

$$V_{out-ideal(y)} = \sqrt{\left[\frac{V_{outy}^2((H_{ky} + \beta H_x)^2 + H_y^2)}{H_{ky}^2 + H_y^2}\right]} \tag{5.11}$$

$$V_{out-ideal(z)} = \sqrt{\left[\frac{V_{outz}^2((H_{kz} + \gamma H_y)^2 + H_z^2)}{H_{kz}^2 + H_z^2}\right]} \tag{5.12}$$

According to the Honeywell application note (see [77]) for HMC1001 & HMC1002, the expected anisotropy fields for each axis are

$$H_{kx} = 9Oe; H_{ky} = 8.5Oe; H_{kz} = 10Oe. \tag{5.13}$$

These values depend on the manufacturing process and are needed in the compensation equations, as explained earlier. The scale factors can be determined by including these parameters in Equations (5.10), (5.11) and (5.12).

5.3.3 Method to find scale factors

In this section, we combine a calibration algorithm with the proposed equations for compensating the cross-axis error; in addition, we also present an optimization algorithm in following part for calculating the scale factors. Then, in the result section, we indicate the improvement for compensation results.

To measure the Earth's magnetic field and to eliminate the undesirable urban and industrial magnetic fields, a simple instrument is used to measure the field in a free outdoor environment as shown in Figure 5.9.

This instrument is mainly made up of non-magnetic materials: screws, PCB connec-

FIGURE 5.9: Image of three-axis magnetometer mounted on a wooden rod for calibration with the Earth magnetic field.

tors, and a wooden rod. A 9-V supply is used for the sensors. The digital data from the micro-controller are stored on a SD cart.
Slight differences in calibration residues may arise owing to the use of different data sets and different test conditions. To prevent this in our study, we compare the residual of the same sensor by using the same data set for identifying improvements brought about by the proposed method.

Therefore, a data set of sensor measurements in the Earth's magnetic field (Figure 5.10) is used to compare the results in the subsequent section. In this case, the improvement in the residual error of the calibration norm arises solely from compensation of the cross-axis error by using the proposed equations. It is clear that the other errors, such as hard and soft iron effect, misalignment, noise and non-linearity, are identical in both cases. These results are presented in the subsequent sections.

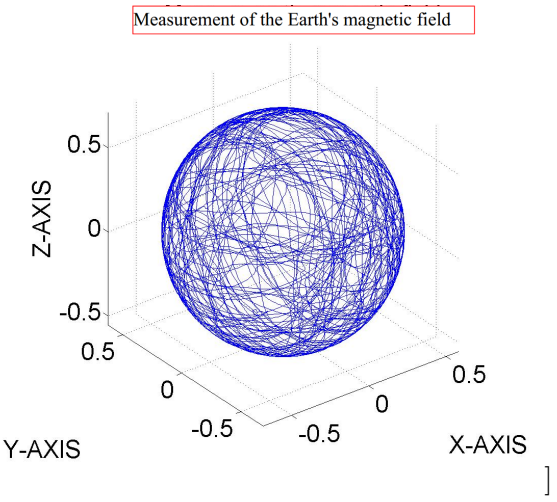

FIGURE 5.10: Three dimensional measurement of three-axes magnetic sensors in the Earth magnetic field (Gauss unit).

For evaluating our real sensor, we add Equations (5.10),(5.11) and (5.12) to the original sensor reading in the linear model (Equation (4.5)). Thus, the variations in the norm of the measured field can be used to determine the scale factors (α, β, and γ).

Optimization algorithm

In this part we describe an algorithm implemented (Figure 5.11) to determine scale factors of α, β, and γ. First, we define an initial interval containing one for each triple (α_n, β_n, γ_n) of a grid[2]. Then, by increasing n for each step these scale factors are substituted by the new values and for each step the calibration algorithm calculates the norm of the residual. As stated earlier, this residual of the error can be used to identify the non-linear error measurement of the sensor.

$$F_{\alpha_n,\beta_n,\gamma_n}(t) = \|V_{out-ideal}(t)\|$$

The norm of calibration will be then divided into several time intervals to measure the peak-to-peak value of each internal. In our case, we measured the peak-to-peak values at one-second intervals.

$$PP_{\alpha_n,\beta_n,\gamma_n}(i) = \big[\mathbf{max}_{t\in[i,i+1]}\, F_{\alpha_n,\beta_n,\gamma_n}(t) - \mathbf{min}_{t\in[i,i+1]}\, F_{\alpha_n,\beta_n,\gamma_n}(t)\big]$$

Finally, the algorithm chooses triple α, β and γ, which in turn gives the least sum S of the peak-to-peak values as follows:

[2]The reason that we use the absolute value for the intervals in Figure 5.11 is the possibility of a reverse sensitive direction as explained earlier in Figure 5.8.

algorithm1.pdf algorithm1.pdf

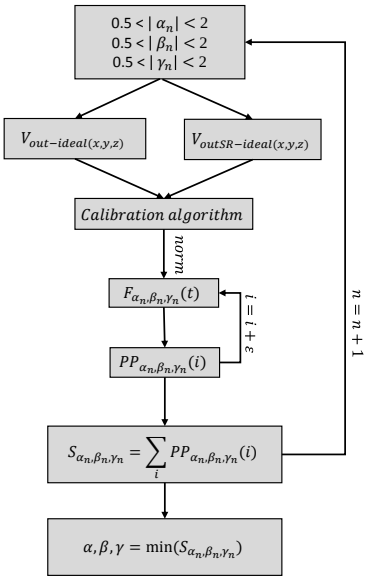

]

FIGURE 5.11: Schematic illustration of optimization calibration algorithm.

$$S_{\alpha_n,\beta_n,\gamma_n} = \sum_i PP_{\alpha_n,\beta_n,\gamma_n}(i)$$

5.3.4 Results

5.3.4.1 Non-flipped sensor

Considering to the above discussion, for the non-flipped sensor used in our experiment, the algorithm gives:

$$\alpha = 1.10; \beta = 1.06; \gamma = -0.94. \tag{5.14}$$

Figures 5.12 and 5.13 show the calibration norms of the three-axis magnetic sensors. The non-compensated data from sensors after calibration in the Earth's magnetic field are presented in blue (residuals norm = 1.193), and the result of the proposed compensation method for non-flipped sensors, is presented in red (residuals norm = 0.149). A huge difference can be observed simply by using the compensation equations by including the scale factors α, β, and γ in order to reduce the cross-axis effect. These results for the norm of the magnetic field are obtained from identical data in sensor measurement. A problem may arise from different offsets for the sensor in different calibrations. Generally, in a non-flipped sensor the offset is unstable; in fact, the quality of the magnetic domain and the sensitivity of a sensor can be changed with time. In this case, the offset should be eliminated in the calibration algorithm for computing the norm of the magnetic field.

Here, the magnetic domain is refreshed before each test by a single *set* pulse while keeping the sensors away from any field stronger than the Earth's magnetic field.

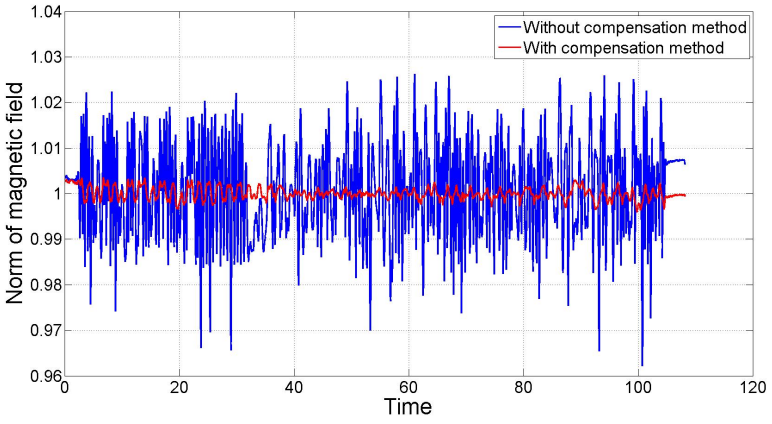

FIGURE 5.12: Comparison of calibration results with and without compensation method. Calibration results in the Earth's magnetic field are shown in blue, and the calibration results with compensation in the same sensor measurement are shown in red. Here, the set/reset mode is inactive in both cases. Note that the norms have been normalized to one.

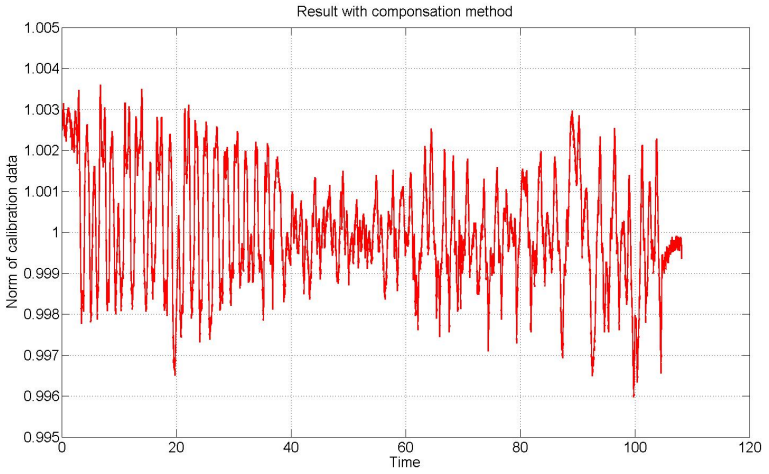

FIGURE 5.13: Calibration result with compensation method: enlargement of Figure 5.12

This approach demonstrates that by using the same three-axis sensors and the same rotation in the Earth's magnetic field, we have efficiently produced better results because of the proposed compensation method.

5.3.4.2 Flipped sensor

For the set/reset or flipping method, Equation (5.9) is expanded for three-axes and the scale factors are included.

$$V_{outSR-ideal(x)} = \frac{V_{outx}(H_{kx}^2 - \alpha^2 H_y^2)}{H_{kx}^2} \tag{5.15}$$

$$V_{outSR-ideal(y)} = \frac{V_{outy}(H_{ky}^2 - \beta^2 H_x^2)}{H_{ky}^2} \tag{5.16}$$

$$V_{outSR-ideal(z)} = \frac{V_{outz}(H_{kz}^2 - \gamma^2 H_y^2)}{H_{kz}^2} \tag{5.17}$$

The estimation of the values of the scale factors is carried out by the same test procedure that has been explained previously. After calibrating the sensor, the optimization algorithm is used to obtain the scale factors in the set/reset mode. It should be kept in mind that, the obtained parameters in Equation (5.14) and Equation (5.18) could be different from one three-axis sensor to another according to the different sensor properties.

$$\alpha = 1.79; \beta = 1.78; \gamma = 1.8 \tag{5.18}$$

The different scale factor values in Equation (5.18), compared to Equation (5.14), derive from different equation forms, and not accurate values for anisotropy fields in Equation (5.13), which are given in the application note of the sensor (see [77]). Equation (5.10) includes $(H_{kx} + \alpha H_y)^2 = H_{kx}^2 + \alpha^2 H_y^2 + 2.\alpha H_y H_{kx}$, whereas Equation (5.15), includes $H_{kx}^2 - \alpha^2 H_y^2$. Therefore, the scale factors (α, β and γ) obtained in the two equations are different.

Now it is convenient to change Equation (5.7) to the one shown below:

$$V_{outSR} = \frac{a.H_k.H_y}{H_k^2 - H_x^2} \tag{5.19}$$

On comparing the above equation with Equation (5.1) which corresponds to the non-flipping method for sensor, it is evident that the effect of cross-axis error in the flipping method is considerably lower than that in the non-flipping method by assuming

$$H_x, H_y, H_z < H_k$$

and

$$H_x^2, H_y^2, H_z^2 \ll H_k^2$$

It is expected that the error in the norm of the data after the calibration should be smaller when the set/reset method is used (see [75]). According to the datasheet of HMC1001

& 2 the cross-axis error without implementing the set/reset method is ±3%FS and that with implementing the set/reset method is 0.5%FS. Figure 5.14 shows the norm of the magnetic field using the classical calibration method in blue and that of the magnetic field using the proposed algorithm in red. Here, the linearity of the results is improved more than two-fold because of the compensation methods. As explained

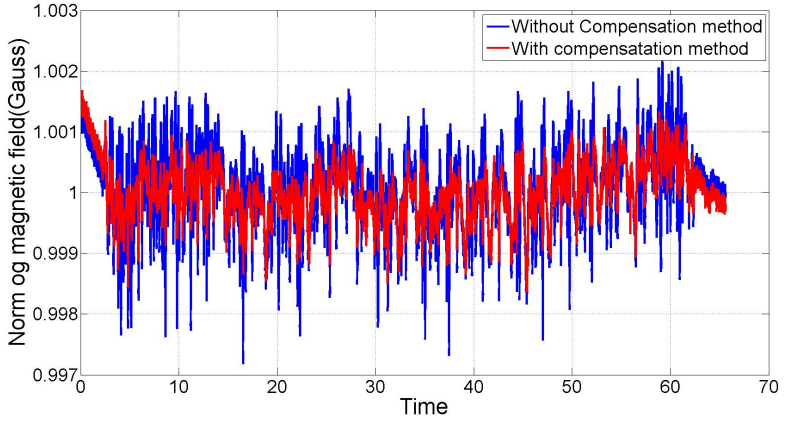

FIGURE 5.14: Comparison of the calibration results in the set/reset mode. The norm of the calibration in the Earth's magnetic field is shown in blue, and the red one is the result of the same calibration with the compensation method.

earlier, compared to previous results, the cross-axis error can be removed efficiently by using the set/reset and averaging methods. This case is demonstrated by comparing Figure 5.12 and Figure 5.14. In Figure 5.14, most of the non-linearity of the sensor is removed by using the set/reset method. Therefore, it is clear that large compensation values in the non-flipped sensor are not obtained in the set/reset method.

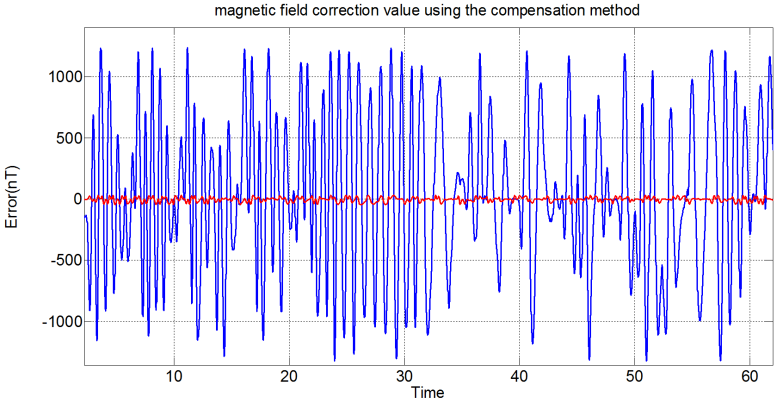

FIGURE 5.15: The blue lines show the correction value for the amplitude of the magnetic field by using the compensation method for the non-flipped sensor while rotated in the Earth's magnetic field (Figure 5.10). $(H_{out} - H_{out-ideal})$. The red lines show the correction value for the flipped sensor.

Figure 5.15 shows the error reading by the sensor for one axis during rotation in Earth's magnetic field (Figure 5.10). These results indicate a different amplitude of the magnetic

field before and after compensation, owing to the cross-axis error. From these results, we can find that the maximum correction field for a flipped sensor (HMC1001& 2) is $37nT$ and for a non-flipped sensor is $1.28\mu T$ in the Earth's magnetic field.
These results have been shown for one given sensor. However, this method can be used for each AMR sensor by replacing the anisotropy field in the equations. The scale factors in the compensation equation can also be found by rotating the sensor in a constant magnetic field, and using the proposed algorithms.

Chapter 6

Indoor calibration

In chapter 4, the error modeling of the magnetometer and calibration procedure have been described. Now, we refer back to two points that are needed for providing the data before any calibration. First, the sensor should be rotated in all possible directions and second the rotation should be performed in a perturbation free magnetic field. The perturbation of the magnetic field causes a non-constant norm of the magnetic field and consequently brings additional errors in the calibration parameters. Hence, one question that needs to be asked is how and where the magnetometer can be rotated in order to gather the appropriate data before any calibration.
One should, nevertheless, consider the problem from another angle: recently, due to the extension of the power line network, industrial zones and urban environments, it has been difficult to find the Earth's magnetic field. Therefore, the Earth's magnetic field is perturbed due either to the man-made soft iron effect for those such as vehicles and building or to due the hard iron effect such as electromagnetic devices.
To date, several literatures have proposed using different experimental instruments for magnetometer calibration [80], [81], [82], [83]. Generally, they are based on using a rotating platform with two-axis motion to uniformly cover the whole unit sphere. These apparatuses can be split into those that are rotated manually [82], and those that use motors [80] (see Figure 6.1).

Moreover, to avoid any additional errors, these rotating platforms should be made from non-magnetic materials such as aluminum and plastics. In the case of motorized platforms, it is difficult to find an appropriate motor with enough precision and non-magnetic properties. However, the non-magnetic piezoelectric motor drivers can be used for this aim, as suggested in [80]. Furthermore, one should not forget that for any precision calibration these instruments are still dependent on the quality of the magnetic field that is measured by the sensors. Data collected in an indoor area such as a laboratory could be affected by the proximity of other devices running in the background or other

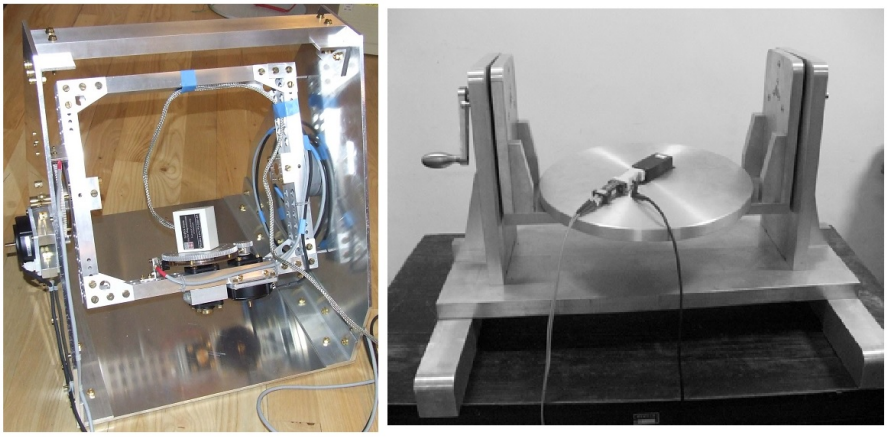

FIGURE 6.1: Photos of non-magnetic mechanical platforms. The figure on the left, depicts a motorized platform [80] and that on the right is a photograph of a non-motorized platform design [82].

factors during the calibration. In this case, the calibration results can skew from the real values. So then, the calibration process needs to be performed in another testing environment, such as the countryside.
Doubtless, for the research point of view, using these devices in an outdoor perturbation free magnetic field would be sufficient to validate the calibration results, but for the industrial point of view, which needs to calibrate a large number of products, this is not the case. As a final point, we should mention some of the drawbacks of using these rotating platforms.

- They are too large to be used inside the shielding box or the Helmholtz coils.
- Since they are constituted by mechanical parts, they need to be calibrated periodically.
- They should be used in a perturbation free magnetic field environment.

This chapter includes two parts: first we propose an indoor calibration method for the magnetometer using the three-dimensional Helmholtz coil and mu-metal box (see Figure 6.2); second, we introduce an extremely low-cost auto-calibration method for the AMR magnetometer. In this case, the implemented circuit is designed to calibrate AMR sensors using integrated coil independence of auxiliary instruments to provide the magnetic field. This method can be used for calibrating a system such as that which contains several AMR magnetometers (for instance a gradiometer) with only three wire connections.

FIGURE 6.2: Photo of the IMCS system in a laboratory environment.

6.1 Indoor magnetometer calibration system (IMCS)

6.1.1 Theory of operation

In the case of Indoor Magnetometer Calibration System (IMCS), we use a three dimensional Helmholtz coil in a different way, one that is compatible with the two-step calibration method described in Chapter 4. Instead of rotating a sensor in a constant field, we rotate a constant norm magnetic field vector around the fixed sensor inside the three-dimensional Helmholtz coil. As depicted in Figure 6.3, in both cases the sensor measurements provide the similar dataset in order to use the calibration algorithm.
For rotating a constant magnetic field vector, three separate mathematical equations need to be used for controlling the currents through the Helmholtz coils as follows:

$$\begin{cases} B_x = a.cos(\alpha)cos(\beta) \\ B_y = a.cos(\alpha)sin(\beta) \\ B_z = a.sin(\alpha) \end{cases} \tag{6.1}$$

The combinations of these equations provide a magnetic field similar to the spherical shape produced by the Helmholtz coil (see also Figure 6.14).

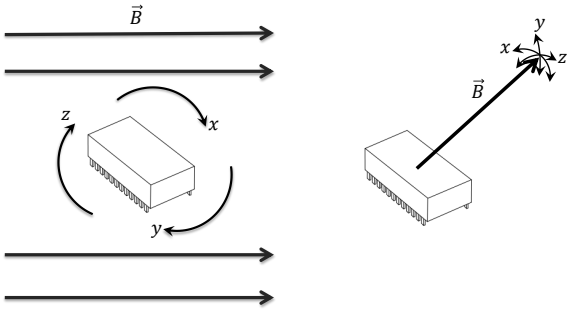

FIGURE 6.3: Left: Rotation of a magnetometer in a constant magnetic field. Right: A constant norm magnetic field vector that rotates around a three axis magnetometer.

6.1.2 Hardware Overview

6.1.2.1 Driver board

The Helmholtz coils generate a constant norm magnetic field when they are fed with an appropriate current. In order to control the current, an interface electronic board has been designed. Precision components should be used to provide analog currents that conform to Equation (6.1). Meanwhile, all three signals should be synchronized and their magnitude should be precisely known as well. Hence, three DACs (digital-to-analog converter) having a resolution of 16 bit are used; and each time they received new data from the ARM microcontroller to rotate a vector of magnetic field. In order to measure the amplitude of the signals, the output of each DAC was sampled again separately by 16-bit ADCs (analog-to-digital converter). These data can be sent back to the microcontroller to determine the current through the Helmholtz coil (4 in Figure 6.4) or it can be stored on an SD card as well (3 in Figure 6.4). Consequently, with this measurement, the bias and magnitude of the currents are measured and compared during the calibration. The advantage of this measurement technique is that we can verify the effect of the temperature on the field provided by the Helmholtz coil. Meanwhile, three temperature sensors are used close to each DAC to measure the temperature variation of each component. In Figure 6.4, this circuit is shown.
The SMB connector is used to connect the DACs output to the Helmholtz coil (1 in Figure 6.4). Since we have variation in the coil resistance due to the temperature, it is reasonable to use the current source for providing the magnetic field. However, on the

contrary, the Helmholtz coil is connected directly to the DAC output of the driver board. As mentioned earlier, in order to overcome this problem, sampling of the currents with the ADCs can be used to compensate for the effect of coil resistance variation on the sensor measurement.

The maximum magnetic field that can be generated by the driver board is close to

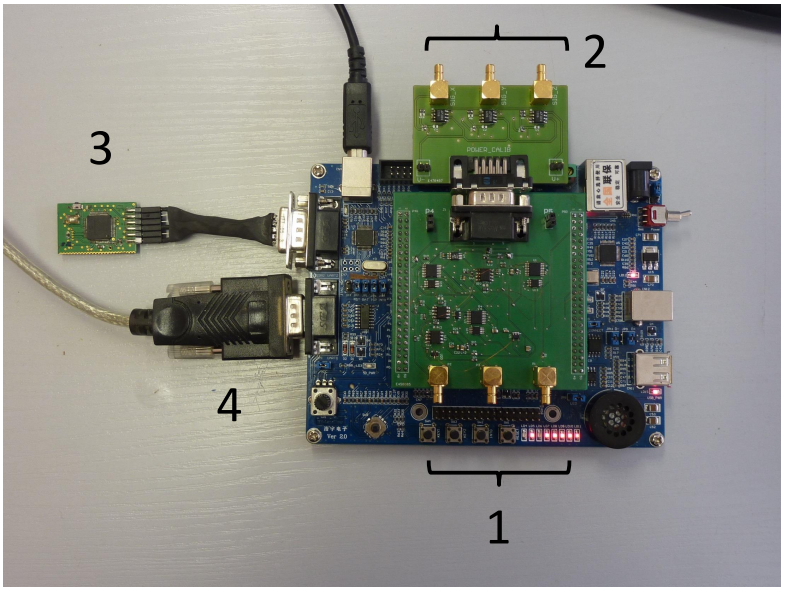

FIGURE 6.4: Photo of the driver board. 1: SMB connectors to connect the three dimensional Helmholtz coil directly to the driver board, 2: SMB connectors to connect the amplified signals after the power amplifiers to the Helmholtz coil, 3: Data logger board to store information on currents sent toward the Helmholtz coil, 4: UART interface to communicate with a PC.

$10\,\mu T$ owing to the DAC output current limitation ($20\,mA$). Hence, in order to provide a magnetic field comparable in scale to the Earth's magnetic field, an auxiliary board has been designed by using a power amplifier (2 in Figure 6.4). The low noise current feedback amplifier is used to amplify the DAC outputs by providing a current of up to $500\,mA$. Using this additional feature enables the same Helmholtz coil to generate a magnetic field of up to $200\,\mu T$.

Figure 6.5 depicts a schematic of the analog part of the driver board for one channel. The precision instrumental amplifier measures the current through the *Rsense*, which corresponds to the Helmholtz coil current as well. Note that in order to avoid the effect of the thermal variation on *Rsense*, this resistance should be chosen from the low temperature coefficient type.

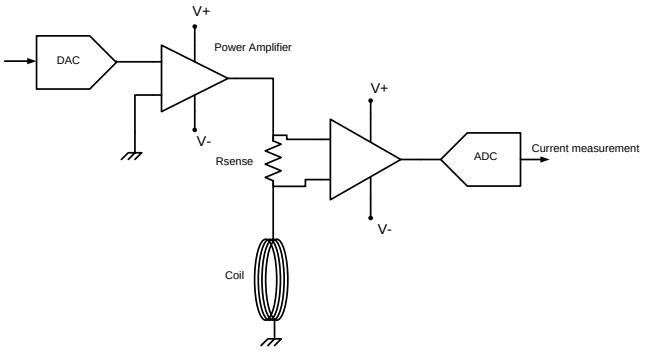

FIGURE 6.5: Schematic of the analog part of the driver board for one channel.

6.1.2.2 Study of the Helmholtz coil design

The Helmholtz coil has been found to appropriate for many applications due to its configuration for producing the uniform magnetic field. The basic design consists of two pairs of parallel coils in series with the same radius. Both coils are aligned on the same axis and are separated by the distance of the coil radius. Moreover, the current passing through the paired coils has the same direction, and thus, the magnetic fields produced by each coil add constructively to provide a uniform field.
Equation (6.2) represents a simple form of the magnetic field produced by the Helmholtz coil for any point on the common axis.

$$B = \frac{\mu_0 nI}{2R}\left(\left[1+\left(\frac{1}{2}-\frac{a}{R}\right)^2\right]^{-3/2}+\left[1+\left(\frac{1}{2}+\frac{a}{R}\right)^2\right]^{-3/2}\right) \tag{6.2}$$

where a corresponds to the distance from the center of the coil, N is the number of turns of wire on each coil, I is the current, R relates to the radius of the coil and μ_0 is the vacuum permeability.
The main goal of using the Helmholtz coil is to provide a larger uniform region of magnetic field in one or more directions, which is not the case for other coil configurations [84], [85]. From Equation 6.2, it is apparent that more regions of uniform field can be produced by the larger coil. However, a large coil faces more difficulties for fabrication and becomes greatly cumbersome. In addition, for such stringent applications that require the removal of the other source of magnetic field, shielding the large dimensional Helmholtz coil can be a serious drawback.
Adding the pair of Maxwell coils will also improve the uniformity region of the magnetic field [86], [87]. Moreover, using the square Helmholtz coil produces a higher magnetic field compared to a round one because of its longer coil length, and it also provides more

inner space for accommodating an object.
Using more coil current and a greater number of turns also leads to the generation of more power dissipation and thus heat through resistive heating. To prevent this disadvantage, a cooling mechanism such as the use of water and air should be incorporated into the coil design. Furthermore, in some cases, the stability of the magnetic field is as important as the uniformity of the field. Therefore, a constant current is required to supply the coil.
Owing to the aforementioned points, the first key issue for designing a Helmholtz coil would be reducing the dimensional size corresponding to the application areas. In this case, a desirable magnetic field will be found by decreasing the coil resistance, power requirement and thermal variation on the coil resistances.
Consequently, for calibrating the MEMS magnetometer such as an AMR, the coil's radius can be scaled from a few centimeters to one meter depending on the sensor sensitivity. In our design, we need to obtain a uniform magnetic field at least in the scale of the three-axis magnetometer (approximately 1 cm). Figure 6.6 shows the view of the Helmholtz coil. Each round coil of the Helmholtz coil has a radius of $20cm$, a resistance of 70Ω and a number of turns of 60. Meanwhile, in order to minimize the risks of perturbation of the magnetic field due to the hard iron and soft iron effect on sensor measurement, the coil structure has been made of non-magnetic material. However, even by suppressing all the suspected materials, some still remain to be considered further as a consequence of supplying wires, electrical connectors, etc.

From the previous discussion, we present in this part the simulation results of the typical Helmholtz coil that has been designed to fit our requirements and is depicted in Figure 6.6. All the numerical results were calculated with MATLAB based on Biot-Savart law.
Figure 6.7 presents a map of the magnetic field distribution produced by the Helmholtz coil when the coil carries a current of approximately 85 mA. The magnitude of the magnetic field is 46.4 μT in the center of the pair of coils. The non-uniformity of the magnetic field is 5.6% with a distance of 5 cm from the center of the Helmholtz coil.
Figure 6.8 also represents the square uniform region ($2cm^2$) of the magnetic field similar to the Earth's magnetic field produced by the Helmholtz coil. For this region the variation of the field is less than 10 nT in the center of the Helmholtz coil according to the simulation.

One should keep in mind that, for all these results, the magnetic field is provided with an ideal Helmholtz coil. However, this is not the case in reality and the uniformity of the magnetic field produced by the Helmholtz coil suffers from other limitations. The

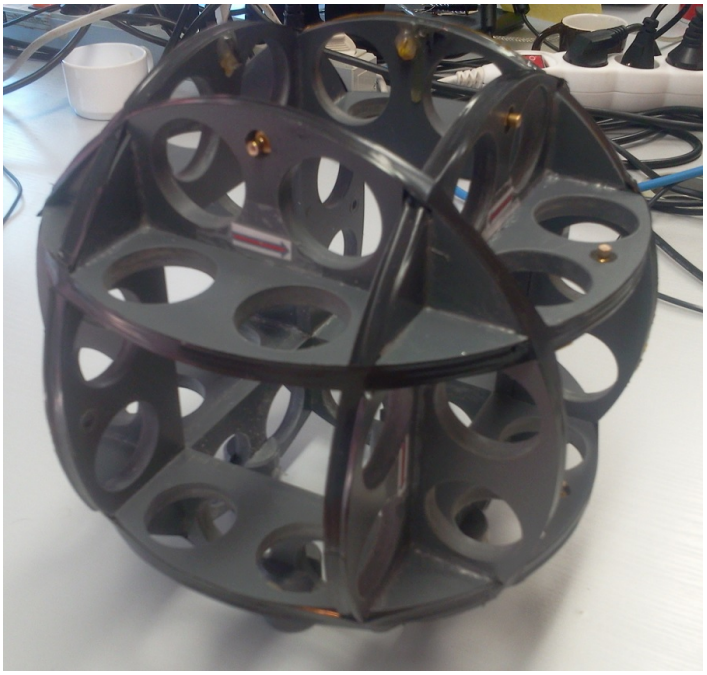

FIGURE 6.6: Photography of a three axis Helmholtz coil.

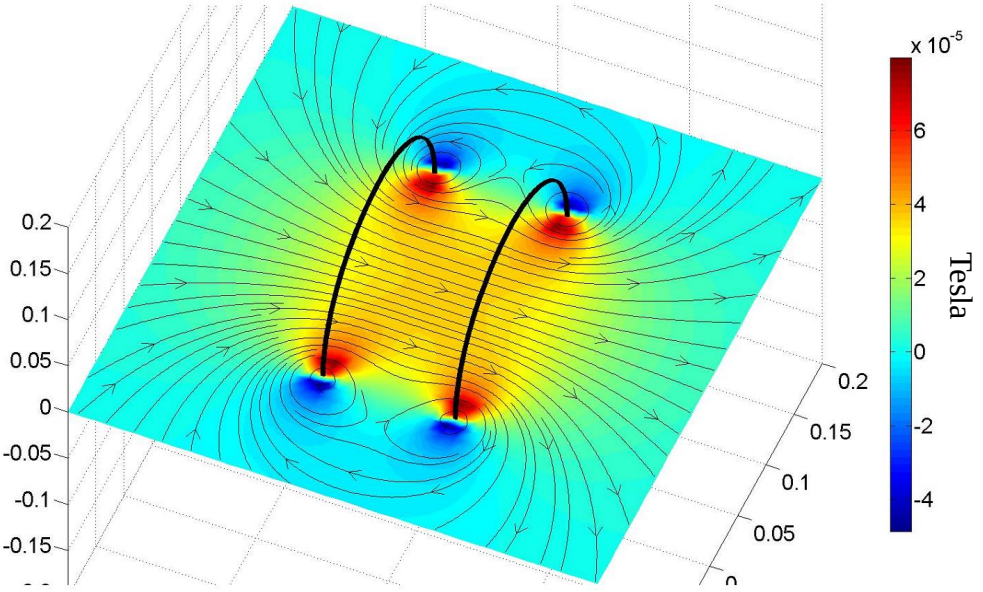

FIGURE 6.7: Magnetic field projection provided by one axis Helmholtz coil.

interested reader can refer to Appendix A for more simulation results on the angular error of the Helmholtz coil.

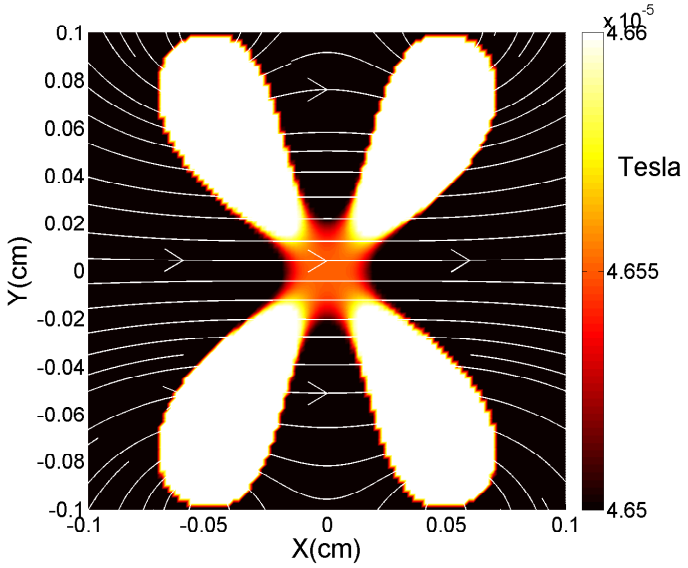

FIGURE 6.8: Represents the magnetic force map and distribution from the top view. A red square ($\sim 2cm^2$) in the center of the coil, depicts the uniform region of the magnetic field with variation of less than 10nT. White lines illustrate the two pairs of coils of the Helmholtz coil.

6.1.2.3 Mu-metal box design

In order to calibrate the bias of the magnetometer in an indoor area, the total magnetic field around the sensor should be eliminated. Thus, a shielding box is needed to isolate the external magnetic field from the field provided by the Helmholtz coil. Figure 6.9 shows the shielding box used in our experiment. It contains three layers of mu-metal materials and one from conductive material with an attenuation factor of $57dB$, approximately. The thickness of the mu-metal material is $1mm$ for all four layers and for the inner box layer the side length is $40cm$. Each layer of the shielding box is separated by $1cm$ air gaps provided by insulating spacers. Figure 6.10 presents the distribution of the magnetic field inside the mu-metal box. In this case the mu-metal is exposed to the Earth's magnetic field when it is perpendicular to one side of the box. Meanwhile, this residual of the magnetic field is plotted in Figure 6.11 among two points of a and b. These results lead us to conclude that the distribution of the magnetic field is not uniform along the length and it varies around 20 nT. In other words, even if the Helmholtz coil provides a perfectly uniform magnetic field, the non-homogeneous residual of the magnetic field may disturb the inside field in another way.
Nonetheless, using a cylinder shape of the shielding box can effectively compensate for this drawback. The various shapes of the shielding box are further studied in Appendix B.

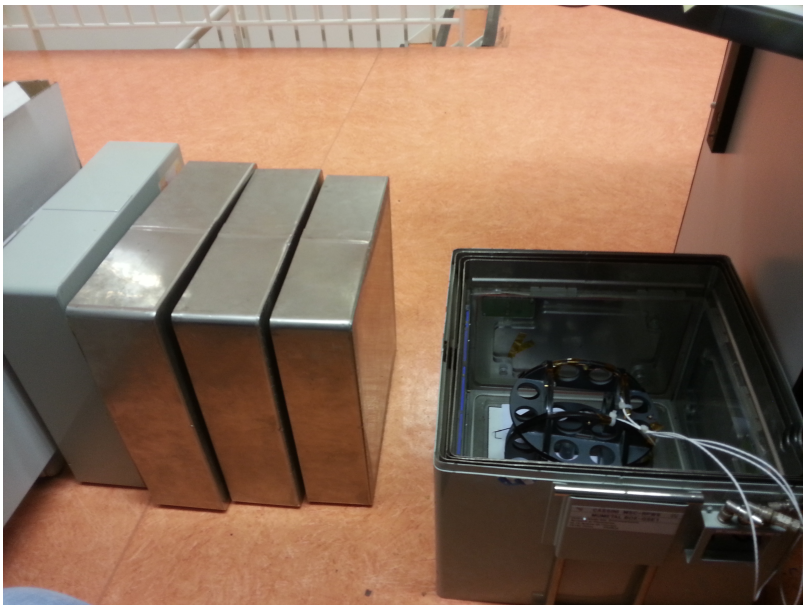

FIGURE 6.9: Photography of the mu-metal box.

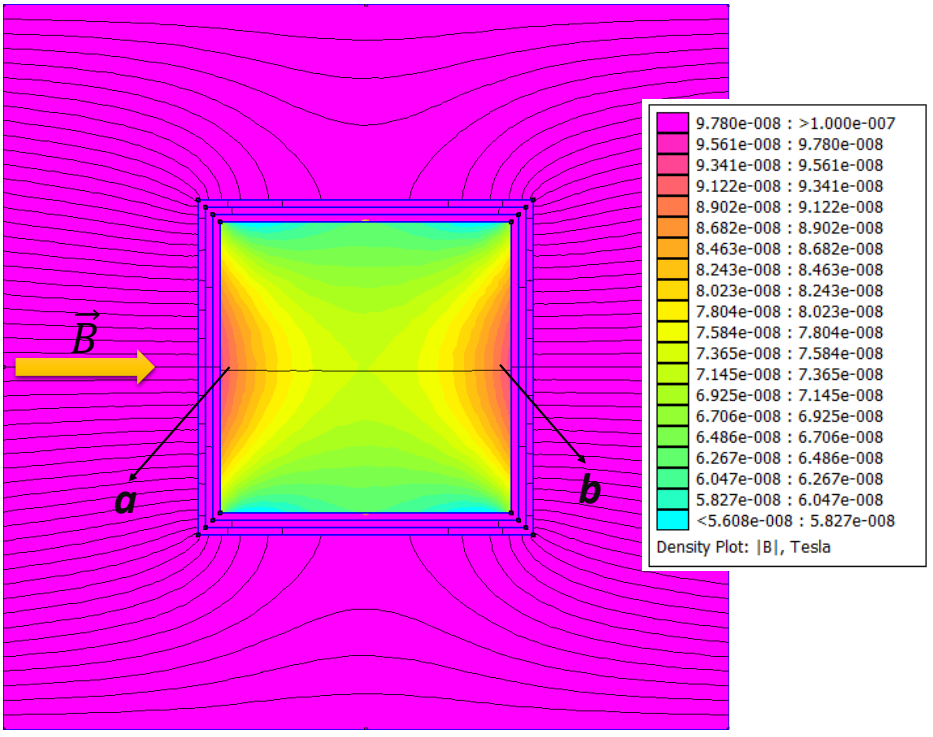

FIGURE 6.10: Simulation result of the distortion of the Earth's magnetic field lines near a high permeability ($\mu = 11000$) four-layer cubic magnetic shield set in Figure 6.9.

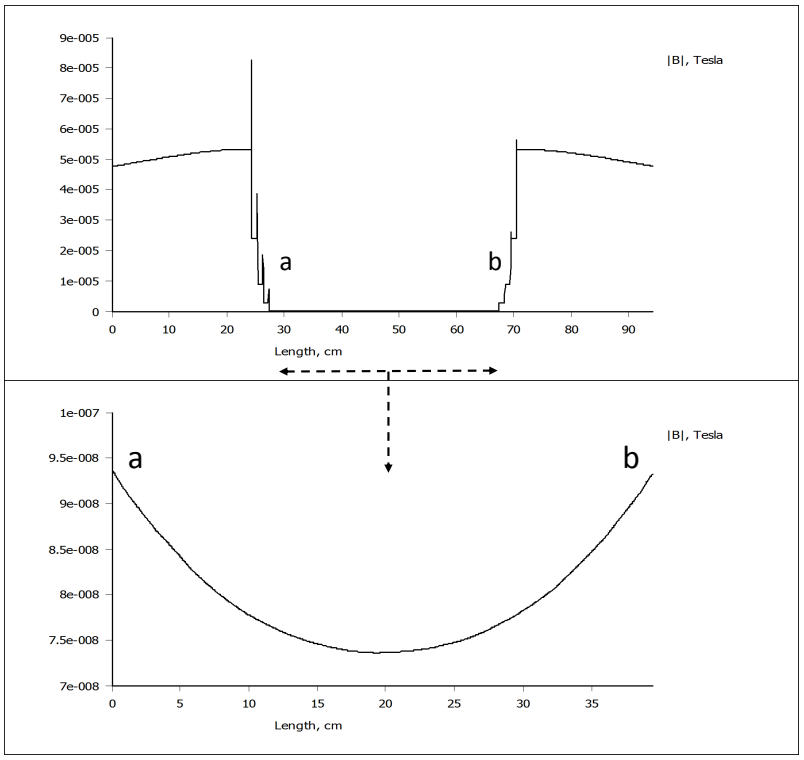

FIGURE 6.11: Simulation results of the uniformity of the magnetic field inside the aforementioned mu-metal box.

6.1.2.4 Sensor board

In this part, we describe the read-out electronic circuitry used to evaluate the performances of the IMCS method. Figure 6.12 shows a sensor board that consists of magnetometers HMC1021 (single-axis) and HMC1022 (dual-axis)[88]. The full scale linear range of the magnetometers is ± 6 Gauss with a resolution of 80 μG. The temperature sensor has been installed close to the AMR sensor package to sample the temperature. However, the temperature sensor measures the combination of other thermal sources conducted by the PCB. Hence, to measure precisely the temperature of the AMR sensor inside the packages, the AMR voltage is sampled as well. Because a current source is used for the AMR sensors, the supply voltage varies linearly with the temperature.
All the analog signals are converted to digital data with a 24-bit, eight-channel ADC. Moreover, the 32-bit microcontroller from the ARM family is used to control the sensor board. Then, the data are transferred through the UART to the Xbee module transmitter for wireless commutations. In parallel, the other board that has been designed consists of an Xbee receiver, a 16-bit microcontroller from the PIC family and the FTDI chip. This board stores the data on a micro SD-card or transfers it through USB to the PC.
Figure 6.13 depicts the overall schematic of the hardware design.

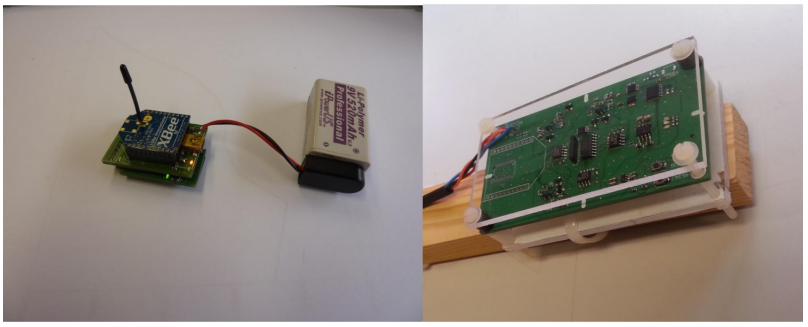

FIGURE 6.12: Photograph of the sensor board (right) and a wireless data logger (left).

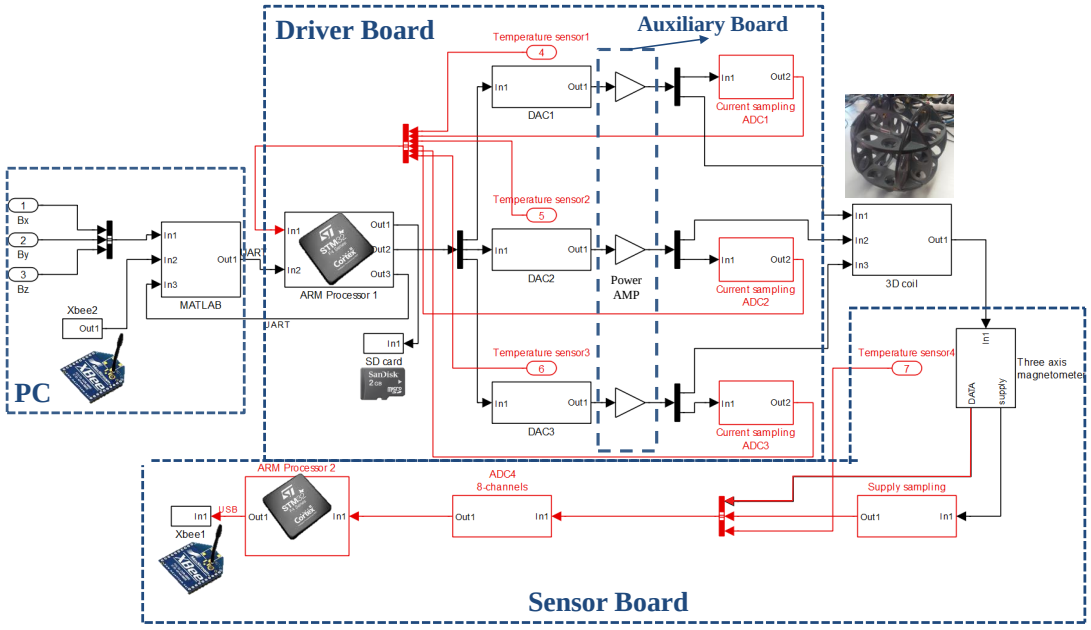

FIGURE 6.13: Schematic of the hardware design. The red lines represent the data measurement from the ADCs and sensors to the microcontrollers.

6.1.3 Experimental results

6.1.3.1 Evaluate the performance of IMCS

To perform the proposed indoor calibration method, first, we have to evaluate the quality of the magnetic field generated by the Helmholtz coil. As discussed earlier, in order to use the two-step calibration algorithm the norm of the magnetic field should be equal to the constant value. Any significant nonlinearity and noise in electronic components may give rise to an abnormal result on the calibration norm. Moreover, the sensor and

the Helmholtz coil should be shielded to eliminate any environmental DC field and perturbation.

Considering these points, we organized experiments as follows. First, the dataset of sensor measurements will be compared with MATLAB simulation while the IMCS method rotates a constant magnetic field vector. Second, the performance of the IMCS method will be compared with classical calibration in a perturbation free Earth's magnetic field. Third, we will compare all calibration parameters such as bias, scale factor and non-orthogonality between the two methods.

As discussed earlier, the Helmholtz coil provides magnetic field vector relative to Equation (6.2) rotating in all possible directions. Figure 6.14 compares the sensor measurement (in blue) when it has been fixed in the center of the Helmholtz coils with the simulation result (in red). It is apparent from these results that the sensor measurement is similar to that with sensor rotation in a constant magnetic field, even when the sensor is fixed inside the Helmholtz coil.

To investigate the IMCS performance in greater depth, an experiment can be per-

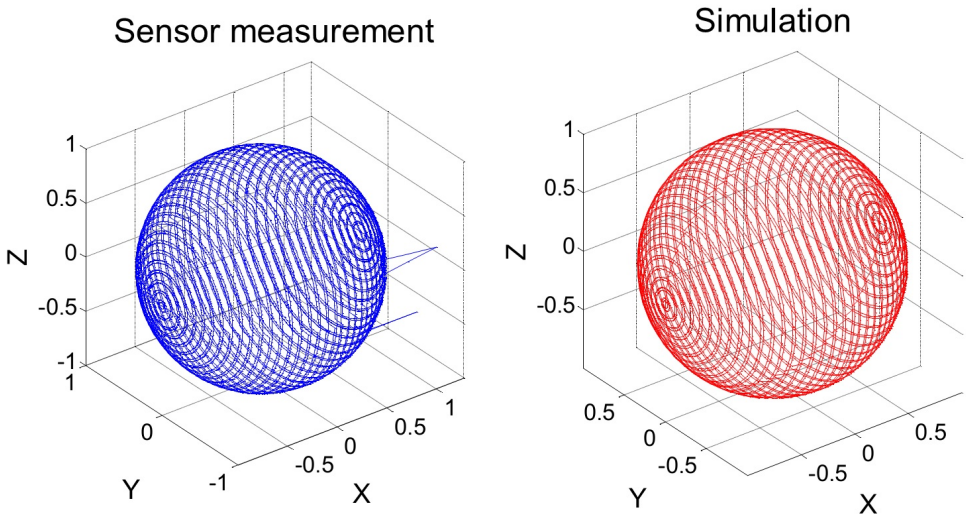

FIGURE 6.14: Red represent the simulation results of the constant vector of magnetic field. Blue represent the results of sensor measurement when the IMCS rotates a vector of magnetic field.

formed to compare the same trajectory of sensor measurement for calibration in the Earth's magnetic field and that with IMCS. To implement this, first, the sensor was rotated in the perturbation free Earth's magnetic field as depicted in Figure 6.15. We used free hand motion to rotate the sensor in all possible directions. Then, the dataset of the outdoor trajectory are processed with MATLAB to reprogram the microcontroller to provide the same trajectory with IMCS method. Figure 6.15 illustrates the experimental results with the Helmholtz coils programmed to provide the same trajectory as

that imparted by free hand sensor rotation. Here, the blue color depicts the trajectory of sensor rotation in the Earth's magnetic field and the red color represents that obtained with the IMCS method.

Furthermore, the comparison of calibration norms for this trajectory has been shown in

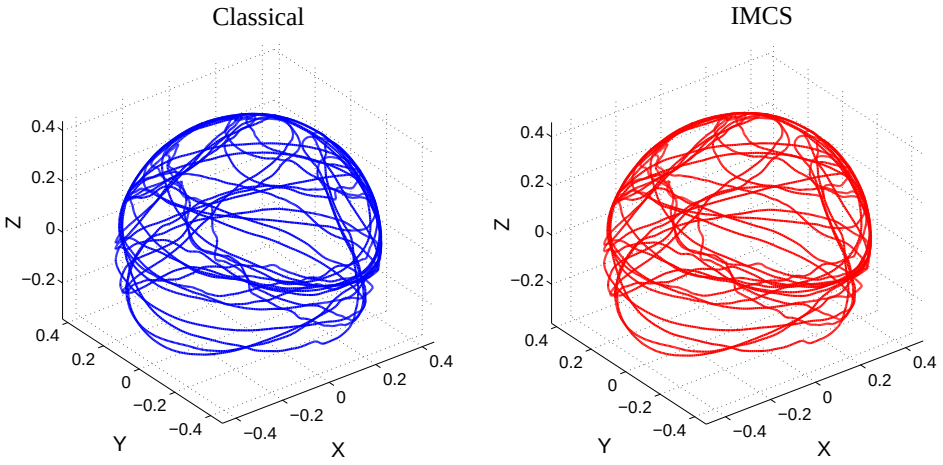

FIGURE 6.15: Blue: Trajectory of sensor rotation in the Earth's magnetic field. Red: Trajectory of the magnetic field vector when it rotated by the IMCS.

Figure 6.16, where the red and blue colors represent the calibration norms of the classical and IMCS methods, respectively. Note that the norm of residuals for the classical calibration is 0.0785 and that for calibration using the IMCS method is 0.0932. It is obvious from this figure that the quality of the magnetic field provided by the IMCS is comparable to that provided by classical calibration in a perturbation free Earth's magnetic field. One should not forget that the calibration process for the IMCS has been performed with the sensor fixed inside the Helmholtz coil and also with both inside the shielding box in an indoor area. However, higher peak-to-peak blue values in Figure 6.16 show additional electronic noise in the driver board compared to the classical calibration norm.

6.1.3.2 Calibration results

In this section, we present a comparison of calibration parameters obtained in a perturbation free Earth's magnetic field and those obtained with the IMCS method. In the case of calibration in the Earth's magnetic field, the daily variation of the magnetic field may result in different values for scale factors. In our calibration zone (latitude: $48°43'17.42"N$, longitude: $2°12'33.26"E$), the common variation of the magnetic field

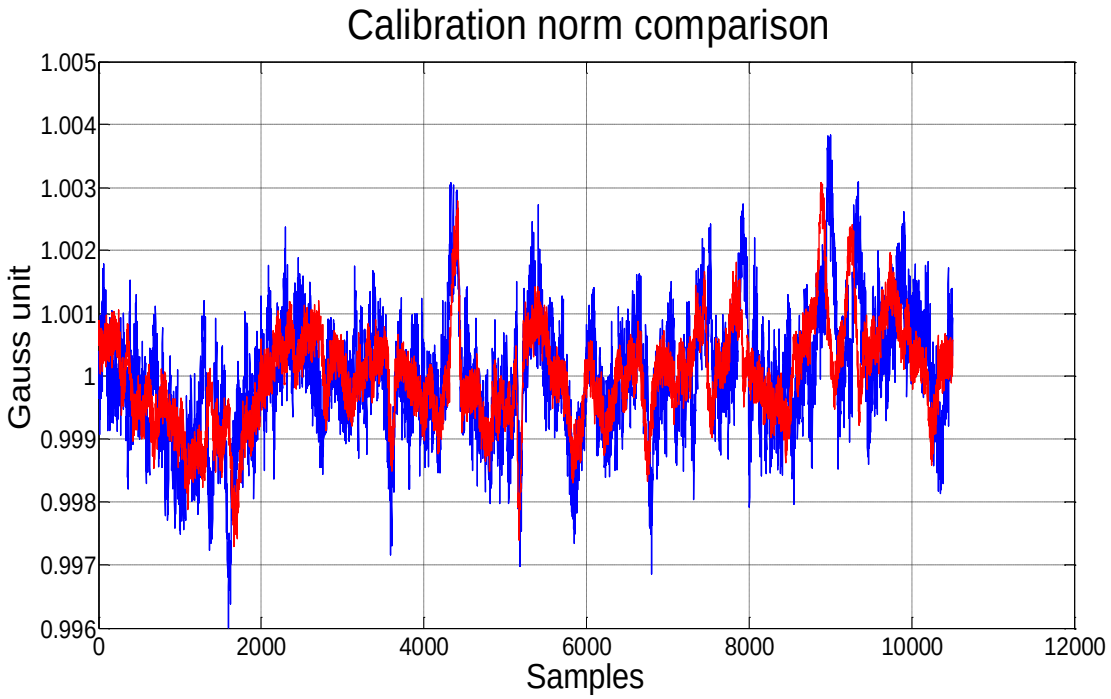

FIGURE 6.16: Calibration norm of classical calibration in the Earth's magnetic field depicted in red and that for the IMCS method represented in blue.

can be close to $40\,nT$.(see Figure 6.2, calibration zone).

In contrast, in the case of the IMCS, more efforts are needed to obtain optimal calibration parameters.

Some error sources are the following:

Perturbation on bias parameters: Obviously, the shielding box should have an appropriate attenuation factor compared to the sensor resolution for calibration. Any residual magnetic field inside the shielding box causes perturbation on the sensor bias. Moreover, the sensor platform, Helmholtz coil body, supplying wires and connectors such as Header, USB, etc, should be made from non-magnetic materials. In addition, the Helmholtz coil should have the same number of turns for two paired coils along a common axis. However, by supplying two paired coils in parallel, the different number of turns for the coils will be compensated by the different current values which are related to the coil resistance ratio.

In other words, what always remains constant is $R_1 I_1 = R_2 I_2$, where R_1, I_1 and N_1 are the parameters of the primary coil and R_2, I_2 and N_2 represent the parameters of the secondary coil.

$$\frac{R_1}{R_2} = \frac{N_1}{N_2}$$

And then consequently:

$$N_1 I_1 = N_2 I_2 \Rightarrow B_1 = B_2$$

Perturbation on scale factor parameters: These errors may be caused by soft iron effects, different amplitudes of the magnetic field of the three-dimensional Helmholtz coil, and the winding position and orthogonality error of the coil set. However, even if the three-dimensional Helmholtz coil support structure is accurately fabricated,the aforementioned errors cannot be eliminated completely.

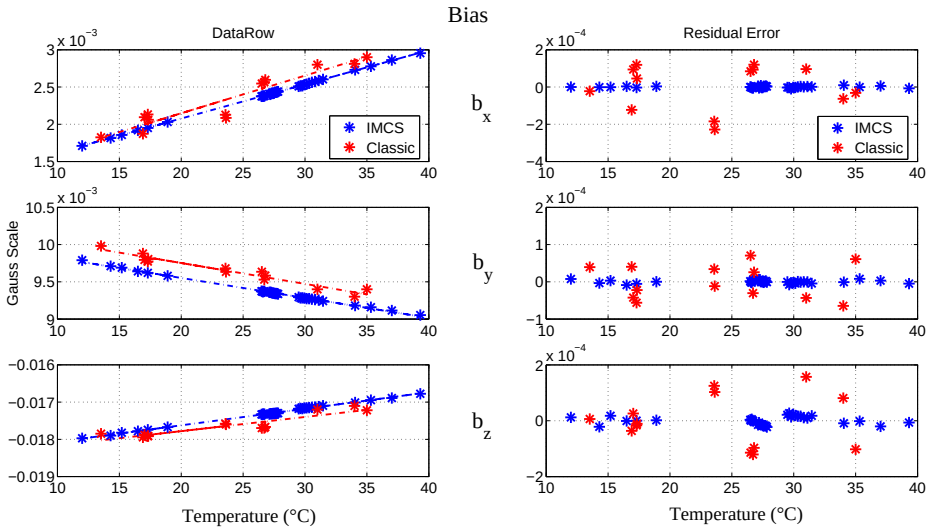

FIGURE 6.17: The left side illustrates bias elements of matrix B (Equation (4.5)) when the sensor has been calibrated at different temperatures. The right side presents the residual error compared to the quadratic fit model.

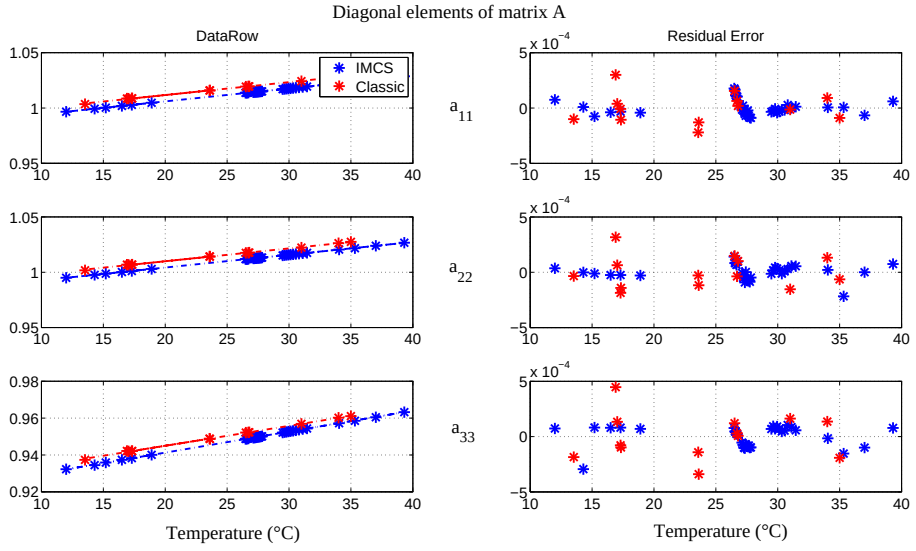

FIGURE 6.18: The left side shows the diagonal elements of the scale factor matrix Equation (4.5) with the sensor calibrated at different temperatures. The right side shows the residual error compared to the cubic fit model.

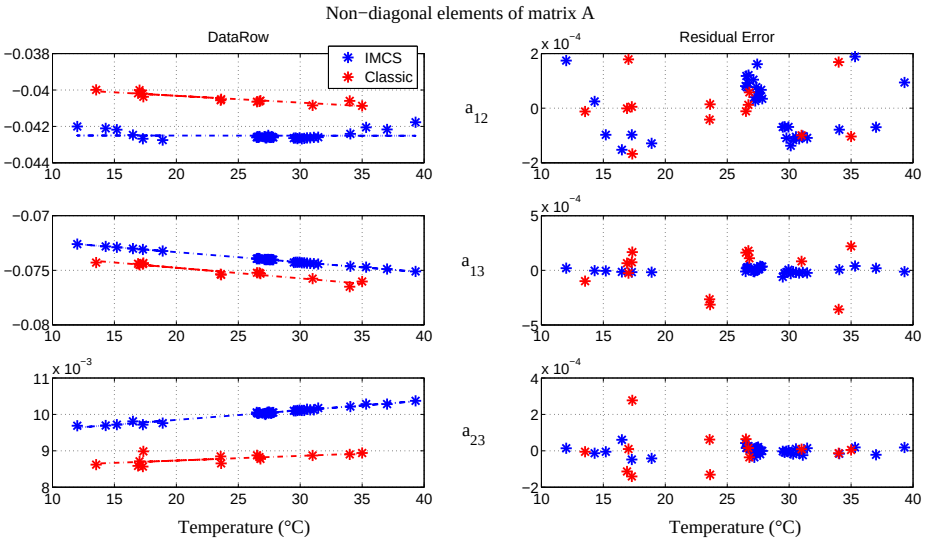

FIGURE 6.19: The left side illustrates the non-diagonal elements of the scale factor matrix (Equation (4.5)) with the sensor calibrated at different temperatures. The right side presents the residual error compared to the cubic fit model.

The results of the two calibration methods are compared in Figures 6.17, 6.18 and 6.19. It should be pointed out that the matrices A and B here correspond to those reported for calibrating the magnetometer in Equation (4.5). In both cases the sensor has been used with the same operating condition and the flipping method has been used as well to improve the sensor stability. We can find truly outstanding results for the IMCS method compared with the classical method, especially for the residual error of the bias from the model fit. The treatment results as a function of the temperature for the calibration parameters also illustrate the similarity between the two methods. Assuming that the mu-metal box is fixed and the residual magnetic field remains constant inside. Then, in this case, any different values of the diagonal parameters of the scale factors and bias can be corrected numerically by the microcontroller to add a scale factor or an offset to the DAC's output.

Note that in Figures 6.17, 6.18 and 6.19, the red and blue colors represent the classical and the IMCS calibration parameters respectively.

Each classical calibration has been performed at different temperatures by rotating the sensor in a perturbation free magnetic field. To prevent any variation in temperature during the sensor rotation in the outdoor area, the sensor was covered by polystyrene layers. Afterward, the same sensor was calibrated with the IMCS method in a noisy laboratory environment in a shielding box. Each calibration with the IMCS is performed solely by sending the command to the driver board from the PC without any other interfaces. In order to control and stabilize the temperature inside the shielding box, the hot (or cold) air was injected into the mu-metal box through the plastic pipe. Each IMCS calibration takes 3 min to rotate a vector of the magnetic field in all possible

directions (see Figure 6.14) for feeding the two-step calibration algorithm.
It should be recalled that, as already demonstrated in Figure 3.10, the sensor sensitivity decreases by the temperature increment. Consequently, considering Equation (4.5), it is obvious that the diagonal elements of matrix A increase for compensating or calibrating the sensor. In addition, the bias of each sensor axis can increase or decrease by the temperature increment, depending on the sensor bridge's connection to the amplifier. Although like any other resistance bridge configuration, the absolute value of the bridge output increases by the temperature increment.
The most striking results are presented in Table 6.1. This table is quite revealing in several ways. First, the residual error from the model fit of the scale factor matrix is slightly better for the IMCS method. Second, the residual error from the model fit of the bias parameter in the IMCS method can be improved significantly. Furthermore, the maximum difference in the bias parameters among the methods is close to 30nT.

Bias		
	Residual Error	
	Classical	IMCS
b_x	28nT	2nT
b_y	14nT	1.3nT
b_z	20nT	4.5nT
Non-diagonal parameter of scale factor		
a_{12}	360ppm	450ppm
a_{13}	470ppm	140ppm
a_{23}	370ppm	130ppm
Diagonal parameter of scale factor		
a_{11}	250ppm	250ppm
a_{22}	340ppm	350ppm
a_{33}	500ppm	220ppm

TABLE 6.1: Comparison of calibration parameters between the classical calibration and the IMCS methods.

Nevertheless, one has to accept that even after removing all the materials that have the permeability to absorb and generate a magnetic field, some elements remain. The angular error of the coil, supply wires and small mu-metal box compared to the sensor and Helmholtz coil size may account for the difference in the results.

6.1.3.3 Arbitrary position

As discussed before, in the proposed method, a vector of magnetic field is rotated by programming the Helmholtz coil. Hence, the three-axis magnetometer measures several points with different values of the magnetic field vector components along the X, Y and Z-axis on a sphere (see Figure 6.20). In the case of sensor measurement, this is equivalent to rotating the sensor in all possible directions in a constant vector of magnetic

field.

This leads us to believe that the sensor position in the center of the Helmholtz coil can

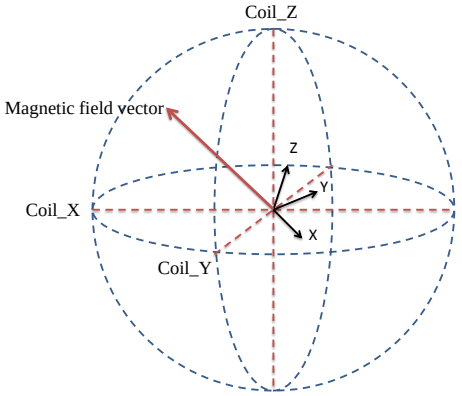

FIGURE 6.20: Scheme of the sensor positioning in the center of Helmholtz coil when a constant vector of magnetic field rotates around the sensor.

be in any arbitrary direction. Perhaps the main advantage of this method is that the maximum magnitude of the magnetic field produced by the Helmholtz coil measured by the sensor is independent of the alignment relative to the coil axis. Therefore, we can overcome any alignment problem with the Helmholtz coil axis. In order to verify this, as illustrated in Figure 6.21, the sensor has been calibrated with an angle of 33 ° to the Helmholtz coil axis. Table 6.2 compares the results obtained from the preliminary analysis. These results for the scale factor matrix confirm our expectation of the aforementioned theory.

Because of the redundancy angle, if each axis of the Helmholtz coil is used separately to calibrate the sensor, the first two diagonal elements of the scale factor matrix should be multiplied by the factor 0.839 ($cos\,33\,°$). Compared to this, we obtained almost similar results when the sensor does not exhibit any deviation with the coil axis. Small

Angle	Scale factor matrix					
	a_{11}	a_{12}	a_{13}	a_{22}	a_{23}	a_{33}
0°	1.0000	−0.0401	−0.0712	0.9980	0.0102	0.9369
33°	1.0015	−0.0390	−0.0757	0.9985	0.0086	0.9343
Angle	Bias matrix					
	B_x		B_y		B_z	
0°	0.0023		0.0096		−0.0171	
33°	0.0024		0.0098		−0.0170	

TABLE 6.2: Comparison of calibration results when the sensor has zero degree angle with the Helmholtz coil axis and when it has a deviation of 33 °.

differences, however, exist because of non-perfect Helmholtz coil errors and different positioning of the wires and connectors.

As a conclusion of this part we can write: First, to calibrate the magnetometer with

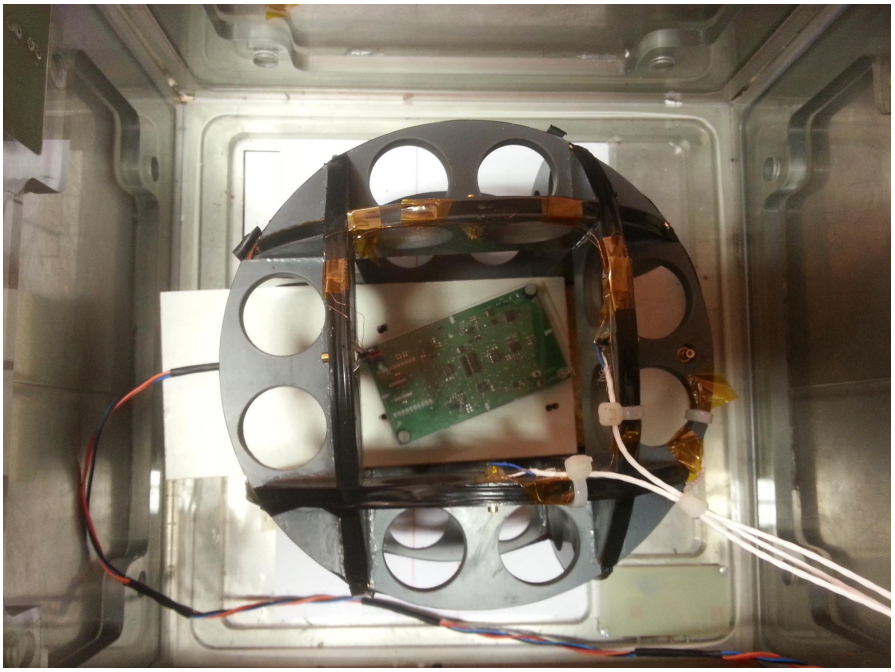

FIGURE 6.21: Sensor calibration with the IMCS method when the sensor is at angle of 33 ° on the x-axis of the Helmholtz coils.

the proposed method, the sensor can have an arbitrary position because of using the Helmholtz coil. However, the boundary of this arbitrary region depends to the Helmholtz coil dimension and the required accuracy for the calibration. Second, the magnetometer can have an arbitrary direction to the coil axis.

6.2 On-board solution (auto-calibration)

Magnetic sensors require periodic calibration to ensure data accuracy. They may change over time in terms of their ability to respond to the applied field. However, the importance of this periodic calibration depends on the sensor type and the required accuracy. AMR sensors are also not separate from this. However, they have the advantage of using the internal coil to provide flipping for the sensor. Consequently, we can assume that their bias remains constant over time by using the flipping method. Nevertheless, if using sensors in normal operation (without flipping method) or if the sensors are exposed to a strong applied magnetic field, their material property changes over time.
Calibrating the magnetic sensor usually requires a special instrument and process to produce and measure the magnetic field, and mainly depends on the experience (as discussed so far). Moreover, the calibration process needs to produce the magnetic field as a reference to extract the calibration parameters. In general, the magnetic field provided

by the Helmholtz coil is used to identify the error of the sensor. Since these instruments are large and expensive, it is not possible to implement them on the sensor board. Thus far, the AMR sensor is the most developed one for detecting the Earth's magnetic field. Typically, AMR sensors are equipped with two different coils for each axis. These coils are able to provide the magnetic field in parallel and perpendicular to the easy axis of the AMR bridge element. The so called offset coil is recommended to suppress the bias of the bridge by producing the magnetic field. Meanwhile, in some applications they are used to improve the linearity and sensor performances as a negative feedback [89].
In this section, we propose a novel use of these coils for calibrating the AMR sensors. This aspect gives us the ability to calibrate the sensor automatically within the system, whenever the sensor needs to be calibrated. In the proposed method, the sensor is shielded by a mu-metal box to eliminate the indoor perturbations of environmental magnetic fields. Given to the fact that this indoor calibration method does not depend on 3D Helmholtz coils, a rotating platform or other instruments to extract the scale factor and bias parameters of the sensor. As will be described in the following sections, a microcontroller is used to control separately three currents in the three offset coils in order to simulate a rotating vector of a magnetic field with constant magnitude.
The proposed auto-calibration method is effective for calibrating an AMR magnetic sensor for systems such as inertial measurement units (IMUs), attitude, heading reference systems (AHRSs), and smartphones.

6.2.1 Theory of operation

Offset coils (see Figure 6.22) are used here to provide a three-dimensional magnetic field like the Earth's magnetic field surrounding the three-axis sensor. Usually this coil is used to suppress the bridge offset by generating a constant field in the opposite direction (see Figure 6.22).

According to the datasheet [79] of the sensor (HMC1021 & HMC1022), the offset coils provide $\sim 21.7mT/A$, and the resistance for each axis is close to 50Ω. In order to obtain a trajectory similar to that of sensor rotation in Earth's magnetic field, the same concept is used by implementing Equation (6.1).
Variations in α and β provide the same behavior for the sensor as rotating it in the Earth's magnetic field, although the sensor is fixed in this method. The experimental setup of the proposed method after identifying matrixes A and B can be defined as follows (in the following text matrices A and B correspond to Equation (4.5) in chapter 4). First, the mu-metal box is not perfect, and secondly, the offset coil does not permit to identify all the components of matrices A and B:
Mu-metal box : the sensor should be shielded by the mu-metal box for preventing

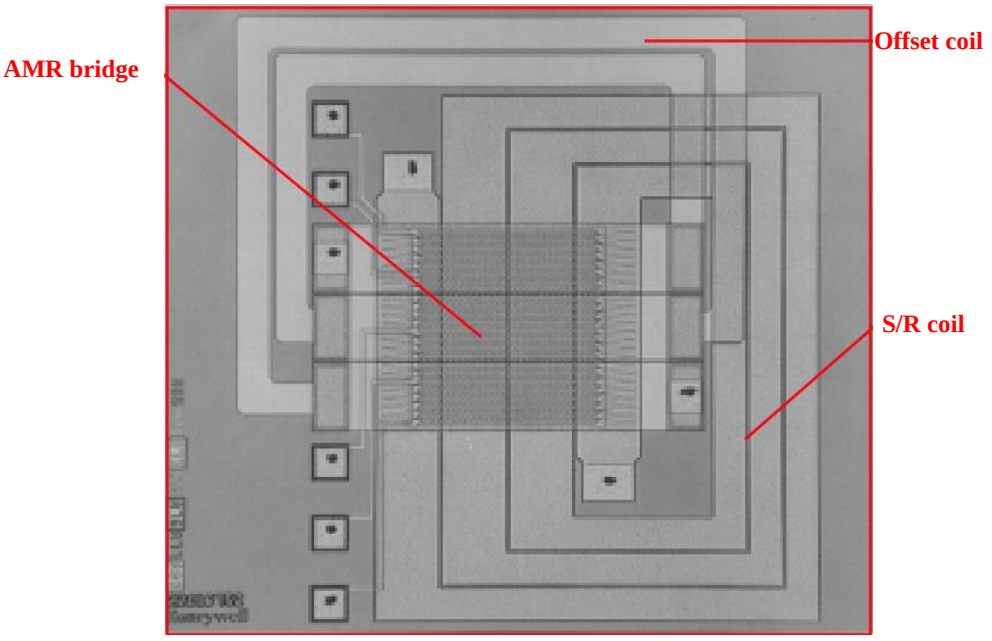

FIGURE 6.22: Image of the offset coil position inside the AMR sensor package.

the external magnetic field that may interface with the generated field. Furthermore, one advantage that can only belongs to this method is that the mu-metal box can be as small as the sensor board size. Consequently, using a low cost small type of the shielding box provides an appropriate attenuation factor due to its size (see Appendix B)

Offset coils: to identify the non-diagonal elements of matrix A, an orthogonal field is needed to stimulate for each one-axis sensor. In our case, for each sensor, this should be provided by the offset coil of another one-axis sensor. Here, due to the offset coil position and limitation inside the package, this is impossible. However, one classic or IMCS calibration procedure can be used for identifying the elements of matrix B and the non-diagonal elements of matrix A. Note that the diagonal elements of matrix A can be identified before a classical or IMCS calibration, while offset coils are calibrated with a well-known sinusoidal magnetic field generated by an auxiliary coil. Then, a similar sinusoidal field that is generated by the offsets coil with microcontroller collaboration, can be used to compare the sensor measurement and to calibrate offset coils. However, as mentioned earlier, we use one classical calibration to identify the other calibration parameters. Therefore, offset coils can be calibrated with the Earth's magnetic field, as we will explain in the following sections, and this process can be eliminated.

6.2.2 Experimental results

6.2.2.1 Evaluation of the performance of the offset coil for calibrating the AMR sensors

Schematic of the driver circuit for calibrating the three-axis sensors is shown as follows.

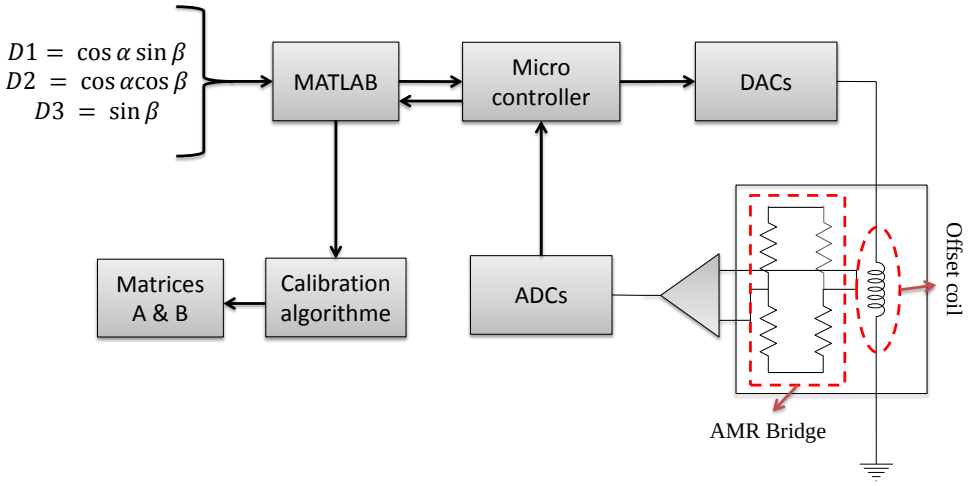

FIGURE 6.23: Schematic of auto-calibration system for calibrating the AMR sensors by using the offset coils.

In the schematic of Figure 6.23, the mentioned functions in Equation (6.1) are converted with MATLAB to the appropriate data in HEX format. Then, data for three vectors are loaded into the flash memory in the microcontroller. Three DACs having a resolution of 16 bits, non-linearity of 0.03% FS and noise parameters of $20nV/\sqrt{Hz}$ are controlled by three separate serial peripheral interfaces (SPIs). Thus, three-dimensional magnetic fields are provided by connecting the DAC outputs to the three offset coils. To generate a magnetic field identical to the Earth's magnetic field, series resistance is used to regulate the current (see Equation (6.23)). Three ADCs having a resolution of 16 bits are used by the microcontroller to read the sensor measurement during calibration.

We present the following results to evaluate the performance of the auto-calibration system using the offset coils. Furthermore, we compare these results with the result of the classic calibration of the same sensor in a free perturbation outdoor magnetic field.

Figure 6.24 illustrates the trajectory of the sensor measurement by using the offset coil in red, and by rotating the sensor in the Earth's magnetic field in blue.

Figure 6.25 depicts the comparison of residual error of the calibration norms. In

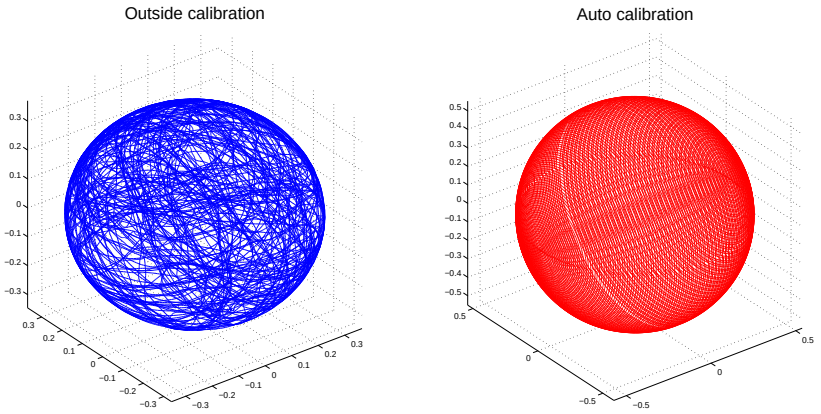

FIGURE 6.24: Trajectory of sensor rotation in the Earth's magnetic field plotted in blue, and the trajectory of sensor calibration by using the offset coil plotted in red (Gauss unit).

this case, the blue plot presents the results while the sensor was rotated in the Earth's magnetic field, and the red plot shows the result using the offset coil for calibrating the sensor in an indoor area. According to these results, the residual error of the calibration norm using the offset coil is homologous compared to the free outdoor calibration in the Earth's magnetic field. This means that, as well as rotating the sensor in a perturbation free Earth's magnetic field, the perturbation of the magnetic field provided by the offset coils has the same performance in the mu-metal box. Note that an ideal sensor (error free) would provide a constant norm without any deviation. However, in reality, for low cost sensor this norm has deviations and residual errors from a constant value for two reasons: first, because of sensor errors (non-linearity, cross-field, noise, etc.) and second, perturbation on the magnetic field that the sensor measures. Therefore, by using the same sensor due to the mentioned errors, Figure (6.25) demonstrates that the magnetic field generated by the offset coil is comparable in case of perturbation with the Earth's magnetic field.

6.2.2.2 Results

The main objective of this section is to illustrate the stability of the parameters while the sensor is calibrated indoors using the proposed method. This experiment is performed for several calibrations, and the results are shown in Table 6.26. In this case, in order to stabilize the temperature of the sensor ($32°C$), the calibration is done after two

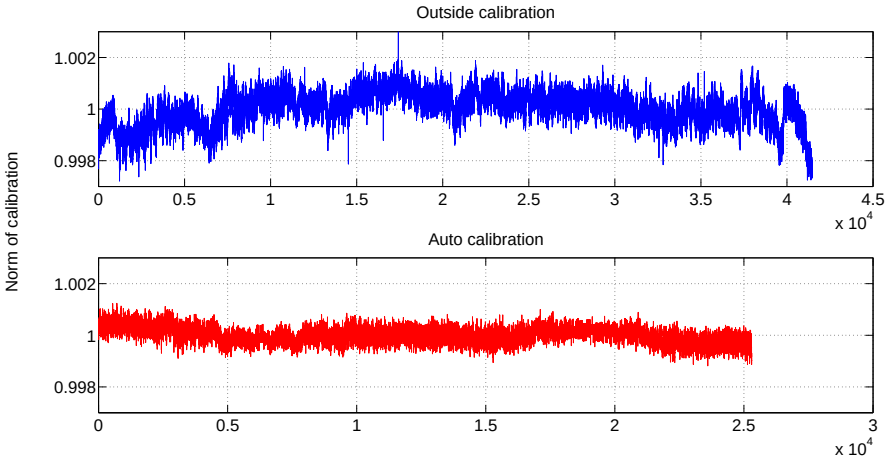

FIGURE 6.25: Comparison of the calibration results. The norm of the calibration in the Earth's magnetic field is shown in blue, and the red one is the result of the same sensor by using the offset coil for calibration.

days' sensor operation. According to these results, the variation of the scale factor is less than $30ppm$, and that for the bias is $5ppm$. However, the variation of these parameters depends on the attenuation factor of the mu-metal box against low-frequency or static magnetic fields and the magnitude of the external field surrounding it. As

test	1	2	3	4	5	6	7	8	9	10
a_{11}	1,00002	1,00003	1,00004	1,00002	1,00004	1,00003	1,00003	1,00003	1,00003	1,00002
a_{22}	1	1,00001	1	1	1	1	1	1	0,99998	0,99999
a_{33}	1,00002	1,00001	1,00002	1,00003	1,00002	1,00002	1,00003	1,00003	1,00004	1,00004
a_{12}	-0,00048	-0,00048	-0,00049	-0,00048	-0,00048	-0,00047	-0,00049	-0,00048	-0,00047	-0,00048
a_{13}	-0,00093	-0,00091	-0,00092	-0,00091	-0,00091	-0,00093	-0,00091	-0,00092	-0,00091	-0,00092
a_{23}	0,0006	0,00058	0,0006	0,0006	0,0006	0,00059	0,00059	0,00059	0,00059	0,00059
b_{11}	0,00869	0,00869	0,00869	0,00868	0,00868	0,00869	0,00869	0,00868	0,00868	0,00869
b_{21}	0,03287	0,03287	0,03286	0,03286	0,03286	0,03286	0,03287	0,03287	0,03287	0,03287
b_{31}	0,02732	0,02732	0,02732	0,02732	0,02732	0,02733	0,02733	0,02734	0,02733	0,02733

FIGURE 6.26: Results of ten time calibrations for matrices and using the auto-calibration method (biases in Gauss).

discussed earlier, the proposed method only provides the diagonal term of the matrix . Consequently, one classic calibration should be performed to identify the non-diagonal elements of matrix A. Matrices A' and B' present the parameters of classic calibration in the Earth's magnetic field.

$$A' = \begin{pmatrix} 0.9947 & 0.0012 & 0.0515 \\ 0 & 0.9948 & -0.0304 \\ 0 & 0 & 0.9956 \end{pmatrix} \tag{6.3}$$

$$B' = \begin{pmatrix} 0.0034 \\ 0.0385 \\ 0.0276 \end{pmatrix} \tag{6.4}$$

Matrices A and B can be also rewritten as follows from Test 1 in Table.1, in order to compare these results with outdoor calibration.

$$A = \begin{pmatrix} 1.00002 & -0.00048 & -0.00093 \\ 0 & 1 & -0.0006 \\ 0 & 0 & 1.00002 \end{pmatrix} \tag{6.5}$$

$$B = \begin{pmatrix} 0.00869 \\ 0.03287 \\ 0.02732 \end{pmatrix} \tag{6.6}$$

These results illustrate that the diagonal elements of matrix A and the elements of matrix B are approximately similar in both methods even before the last step of auto-calibration. However, small differences come from uncalibrated offset coils and parameters of the electronic circuit such as mismatch resistance, gain error, etc. Now, to compensate for the parameters of indoor calibration due to the outdoor calibration parameters, we can expand the calibration model for the last step of auto-calibration from Equation (4.5) to:

$$H = (S_c\sigma_c).A.h + B + B_c \tag{6.7}$$

where B_c is a 3×1 matrix, in order to compensate for the electronic bias compared to calibrating the sensor in the Earth's magnetic field.

$$B_c = \begin{pmatrix} -0.00529 \\ 0.00563 \\ 0.00028 \end{pmatrix} \tag{6.8}$$

S_c corresponds to the diagonal scale factor that originates from the gain error in electronic, un-calibrated offset coils, and σ_c is that for the misalignment and soft iron effects.

$$S_c\sigma_c = A'/A \begin{pmatrix} 0.9947 & 0.0017 & 0.0524 \\ 0 & 0.9948 & -0.0298 \\ 0 & 0 & 0.9956 \end{pmatrix} \tag{6.9}$$

However, we should assume that the compensation parameters do not change with temperature, ageing, etc.

Now in order to calibrate the system, the microcontroller in Figure 6.23 should be reprogrammed by considering these compensation values in Equation (6.7). This step

completes the calibration process by combining the compensation parameters with the auto-calibration system. Then, the auto-calibration system, calibrates the sensor only by shielding that on the mu-metal box and without any dependency on the more outdoor or classical calibration. It should be mentioned that the non-diagonal parameters of matrix A are only valid if we assume that these errors are only proportional to the applied external field. In other words, if we add or replace a ferromagnetic material on the sensor board, another calibration in a constant magnetic field is needed.
We can now summarize the main features of the auto-calibration method:

1. Obtain the auto-calibration parameters with the offset coils while the sensor is inside the mu-metal box. In this step, the parameters are not fully calibrated (matrices A and B).

2. Calibrate the sensor only once with the classical method in the perturbation free Earth's magnetic field or the IMCS method (matrices A' and B').

3. Expand Equation (4.5) to Equation (6.7) and obtain the compensation parameter for the auto-calibration method.

4. Reprogram the microcontroller with new parameters in Equation (6.7), in order to complete the calibration process.

Chapter 7

Conclusion

The following conclusions can be drawn on, basis of the theoretical and experimental results obtained in the previous chapters:

- So far for the low cost strapdown inertial navigation systems, the AMR sensors are reliable to use in terms of cost, size and performances. However, their performances could be acceptable when they are used with auxiliary methods such as flipping. The associated errors of the AMR sensor were described especially for the INS, for detecting the Earth's magnetic field. Basically, where power consumption is not the major concern, using the flipping method can significantly reduce the cross field error, sensor noise and the effect of temperature on sensor measurements. Moreover, to improve the linear response of the sensor, the negative feedback loop can be implemented to reduce the total magnetic field sensed by the AMR sensor bridge. In addition, to obtain a linear response of the sensor over the temperature variation, the AMR sensor should be driven by the current source supply. This configuration helps greatly to find the linear model of sensor measurement as a function of temperature. Meanwhile, different low cost read out electronic designs were proposed with an appropriate performance for the sensor.

- A new method was proposed for improving the linearity of AMR magnetic sensors by reducing the cross-axis error. Interestingly, in this method we did not need to compare the error with that in a more accurate magnetometer, nor did we need to know the magnitude of the magnetic field for compensating the cross-axis error. We demonstrated the efficiency of this method by using HMC1001 and HMC1002 from Honeywell. The compensation method was described under two circumstances of sensor performance, with the set/reset mode and without it. The results confirmed that for testing the sensor without the set/reset mode, we obtained very effective results when the compensation method was used; we demonstrated that

the calibration result was improved by a factor of 8. The compensation method was also proposed with the set/reset mode and showed an improvement by a factor of 2 in the calibration results. We can also say that according to the results, we can use the AMR sensors without implementing the set/reset mode by obtaining a performance similar to the performance in the set/reset mode. This result is interesting in systems that have critical points in power consumption and that use the set/reset pulses. For instance, the space application can be considered as a candidate to implement the proposed method. In general, for this application the magnetometers should be small, accurate, light and low power. Several types of the AMR sensors have already been used in several small satellites [90]. Therefore, using this method can improve the sensor performances when it operates at the minimum power requirement.

- The IMCS method was described for calibrating the magnetometer in an indoor area. This method employs no rotating mechanical parts and is thus robust enough to use for the long duration needed to calibrate the magnetometers, and is also compliant with industrial requirements for large a volume of magnetometers flow production. Because a constant magnetic field vector with the Helmholtz coil is rotated around the sensor, the proposed method is compatible with the two-step calibration algorithm to extract the calibration parameters. Meanwhile, the sensor can be calibrated regardless of the deviation from the Helmholtz coil axis, and it can be located anywhere in the homogeneous magnetic field area of the Helmholtz coil.

  The experimental test was performed for two methods of calibration, by rotating the sensor in a perturbation free Earth's magnetic field (the classic method) and by using the proposed method in a noisy laboratory environment. According to the obtained results, the IMCS method provides better residual error for sensor bias calibration and closely comparable results for sensitivity and orthogonality parameters of sensor calibration.

  In chapter 4, a method was proposed that uses a calibration algorithm to verify and compensate numerically for the sensor nonlinearity error by rotation in the Earth's magnetic field. Since the IMCS method can provide all arbitrary trajectories of sensor rotation in an indoor area, this advantage can be exploited by more facilities to analyze magnetometers errors such as the cross field effect, etc.

- A novel on board calibration method was presented for AMR magnetic sensors. We used offset coils to calibrate AMR sensors, which are already included in most AMR sensor packages. Repeatability tests first showed that the method provides stable scale factor and bias parameters. Then, a comparison with the classic

calibration procedure showed good agreement between the scale factor and the bias matrices. A method to compensate for the lack of observability of the non-diagonal elements of the matrix and the bias was proposed. One should keep in mind that the main benefit of the proposed calibration algorithm is that it can be conducted in a disturbed magnetic field. Moreover, this method can be significantly helpful to calibrate the gradiometer where several sensors are spaced on a board and calibrating them by the Helmholtz coil or other instruments raises several difficulties. Using the proposed method also causes more simplification in obtaining the thermal calibration model for the sensors.

Appendix A

Helmholtz coil

In chapter 6, we presented the simulation results to find an appropriate uniform region produced with the Helmholtz coil. However, in previous results we assumed that there is no angular alignment error between the paired coils. Although, this is not the case in reality and unwanted errors may arise from the fabrication process, especially for the three-axis Helmholtz coil, when the coils need to be overlapped (Figure 6.6). In order to remedy the non-uniformity field due to the mentioned error, one possible solution is to use a larger Helmholtz coil. It is apparent that for the same region in the center of the two Helmholtz coils with the same alignment error, the larger one produces better magnetic field uniformity. In this appendix, we outline in greater detail the effect of this error on the uniformity of the magnetic field. Moreover, we characterize an appropriate Helmholtz coil size with the requirement magnetic field uniformity due to the coil alignment error.

Up to now, several authors have studied the uniformity of the magnetic field provided by the Helmholtz coil systems or other type of design [91], [92] and [93]. Sasada and Nakashima in [94] proposed a method by using three pairs of coils to improve the uniformity of the magnetic field with error of less than 0.01%. The investigation of the uniformity of the field has been proposed in [95] as a function of coil spacing for a round coil pair and a single square coil pair. Meanwhile, some information leading to an understanding of the size of the uniform field region for an increased size of the Helmholtz coil has been provided in [96].

Our objective here is to identify the errors that may affect the calibration process by using the IMCS method. One should note here that, the coil alignment error not only changes the direction of the magnetic field but also changes the uniformity of the magnetic field. However, the deviation of the magnetic field in the center of the Helmholtz

coil can not be compensated by calibrating the Helmholtz coil.

A.1 Magnetic field provided by a current loop.

Based on the Biot-Savart law, the magnetic field for any point of A surrounding the current loop can be calculated by adding up the magnetic field contributions. Moreover, the loop of current can be divided into the small segments as a vector quantity in the current direction. This law considers each segment as a current element that is multiplied by the distance. The magnetic field contribution can be calculated as follows:

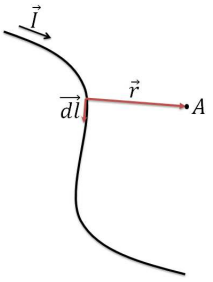

FIGURE A.1: Magnetic field computation at observation point A with Biot-Savart law.

$$d\overrightarrow{B} = \frac{I\mu_0}{4\pi}.\frac{d\overrightarrow{l} \times \widehat{r}}{r^2} = \frac{I\mu_0}{4\pi}.\frac{d\overrightarrow{l} \times \overrightarrow{r}}{r^3} \tag{A.1}$$

Where $\widehat{r}$ corresponds to the unit vector $(\frac{\overrightarrow{r}}{|r|})$, $d\overrightarrow{l}$ corresponds to a small segment and $\mu_0 = 4\pi 10^{-7}$ T.m/A is the permeability of free space.
Thus, the magnetic field of current loop can be written as:

$$\overrightarrow{B} = \oint d\overrightarrow{B} = \frac{I\mu_0}{4\pi} \oint \frac{d\overrightarrow{l} \times \widehat{r}}{r^2} \tag{A.2}$$

Consider the typical loop of current that is presented in Figure A.2. In this case, A represents the magnetic field for any point around the loop in the x-y plane; $\overrightarrow{D_1}$ and $\overrightarrow{D_2}$, are defined as vectors that relate to the distance from the loop center to the current elements and the point A, respectively. In addition, $\overrightarrow{D_3}$ represents the distance between the current elements and point A. Now, in order to calculate the magnetic field in the x-y plane, for any segments of current loop we can write:

$$\overrightarrow{D_3} = \overrightarrow{D_2} - \overrightarrow{D_1}$$

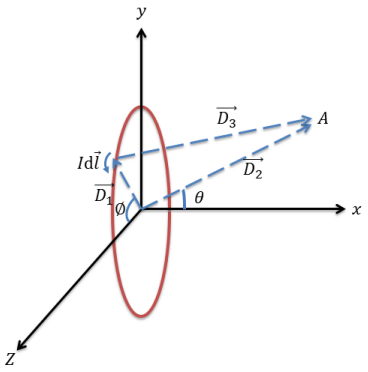

FIGURE A.2: Off-axis magnetic field at any point of A on $x-y$ plane.

for any coordination in the xy plane,

$$\overrightarrow{D_2} = x_0.\overrightarrow{i} + y_0.\overrightarrow{j}$$

for any coordination in the current loop,

$$\overrightarrow{D_1} = R.\cos\phi.\overrightarrow{k} + R.\sin\phi.\overrightarrow{j}$$

and therefore,

$$\overrightarrow{D_3} = x_0.\overrightarrow{i} - R.\cos\phi.\overrightarrow{k} + (y_0 - R.\sin\phi).\overrightarrow{j}$$

Moreover, as a consequence of $d\overrightarrow{l} = d\overrightarrow{D_1}$,

$$d\overrightarrow{l} = \frac{d\overrightarrow{D_1}.d\phi}{d\phi} = R(\cos\phi.\overrightarrow{j} - \sin\phi.\overrightarrow{k})$$

Consider the Equation (A.1),

$$d\overrightarrow{l} \times \overrightarrow{D_3} = R(\cos\phi.\overrightarrow{j} - \sin\phi.\overrightarrow{k}) \times (x_0.\overrightarrow{i} - R.\cos\phi.\overrightarrow{k} + (y_0 - R.\sin\phi).\overrightarrow{j})$$

$$= -Rx_0\cos\phi.\overrightarrow{k} - Rx_0\sin\phi.\overrightarrow{j} + Ry_0\sin\phi\overrightarrow{j} - R^2.\overrightarrow{i}$$

and,

$$|\overrightarrow{D_3}| = (x_0^2 + y_0^2 + R^2 - 2y_0R\sin\phi)^{3/2}$$

Consequently, the magnetic field produced by the current loop can be expressed as:

$$\overrightarrow{B} = \frac{IR\mu_0}{4\pi}\oint \frac{-x_0\cos\phi.\overrightarrow{k} - x_0\sin\phi.\overrightarrow{j} + y_0\sin\phi.\overrightarrow{i} - R\overrightarrow{i}}{(x_0^2 + y_0^2 + R^2 - 2y_0R\sin\phi)^{3/2}}$$

$$\overrightarrow{B_1} = \overrightarrow{B_{1x}} + \overrightarrow{B_{1y}} + \overrightarrow{B_{1z}}$$

Note that $\overrightarrow{B_z}$ is equal to zero for any point in the $x-y$ plane

$$\overrightarrow{B_{1z}} = \oint \frac{-x_0 \cos\phi . \overrightarrow{k}}{(x_0^2 + y_0^2 + R^2 - 2y_0 R \sin\phi)^{3/2}} = 0$$

$$\overrightarrow{B_1} = \overrightarrow{B_{1x}} + \overrightarrow{B_{1y}} = \frac{IR\mu_0}{4\pi} . \left[\oint \frac{(y_0 \sin\phi - R)}{(x_0^2 + y_0^2 + R^2 - 2y_0 R \sin\phi)^{3/2}} . \overrightarrow{i} - \oint \frac{x_0 \sin\phi}{(x_0^2 + y_0^2 + R^2 - 2y_0 R \sin\phi)^{3/2}} \overrightarrow{j} \right] \tag{A.3}$$

Figure A.3 shows the simulation results of the magnetic field provided by a coil in MATLAB. The unit vectors illustrate the direction of the magnetic field for any point on the $x-y$ plane corresponding to Equation (A.4).

$$\widehat{B} = \frac{\overrightarrow{B_{1x}} + \overrightarrow{B_{1y}}}{|B|} \tag{A.4}$$

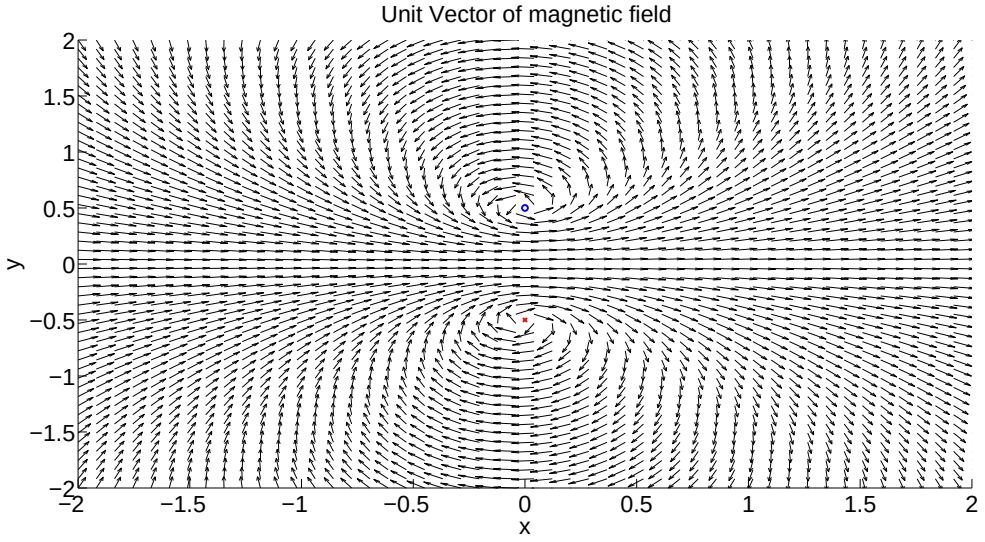

FIGURE A.3: Unit vector of magnetic field provided by a coil.

A.2 Magnetic field provided by a combination of two coils

Suppose we have two coils with analogous radius, turns of wire and currents. One should not forget that using this configuration leads to the same segments of the current elements $Id\overrightarrow{l}$ for both coils. In this case, the center of the second coil can be located arbitrary in the x coordinate (x_1). Similar to what is stated above we define $\overrightarrow{D_4}$, $\overrightarrow{D_5}$

and $\overrightarrow{D_6}$.

Then, the magnetic field produced solely by the second coil for any point of A can be written as below (See Figure A.4): .

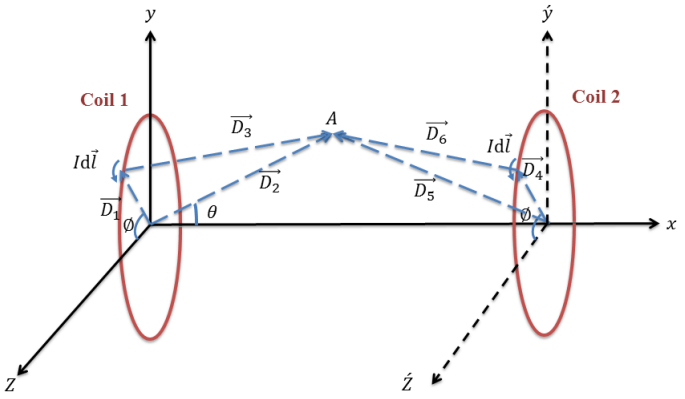

FIGURE A.4: Magnetic field combination provided by two coils at any point of A on the $x-y$ plane.

$$\overrightarrow{D_6} = \overrightarrow{D_5} - \overrightarrow{D_4}$$

Note that both coils are parallel to the $y-z$ plane. As a result, there is no change in z and y coordinates.

$$\overrightarrow{D_5} = (x_1 - x_0).\overrightarrow{i} + y_0.\overrightarrow{j}$$

$$\overrightarrow{D_4} = R.\cos\phi.\overrightarrow{k} + R.\sin\phi.\overrightarrow{j}$$

$$\overrightarrow{D_6} = (x_1 - x_0).\overrightarrow{i} - R.\cos\phi.\overrightarrow{k} + (y_0 - R.\sin\phi).\overrightarrow{j}$$

Here also, $\overrightarrow{B_z}$ can be considered as a zero value and two remnant components of the magnetic field can be written as follows:

$$\overrightarrow{B_2} = \overrightarrow{B_{2x}} + \overrightarrow{B_{2y}} = \frac{IR\mu_0}{4\pi}.\left[\oint \frac{(y_0\sin\phi - R)}{(x_1-x_0)^2 + y_0^2 + R^2 - 2y_0R\sin\phi)^{3/2}}.\overrightarrow{i} - \oint \frac{(x_1-x_0)\sin\phi}{((x_1-x_0)^2 + y_0^2 + R^2 - 2y_0R\sin\phi)^{3/2}}\overrightarrow{j}\right] \quad \text{(A.5)}$$

Finally, for any point on the $x-y$ plane the magnetic field will be computed by summing up the magnetic field vectors produced by each coil.

$$\overrightarrow{B} = \overrightarrow{B_1} + \overrightarrow{B_2}$$

Figure A.5 presents the simulation result in MATLAB using the aforementioned equations.

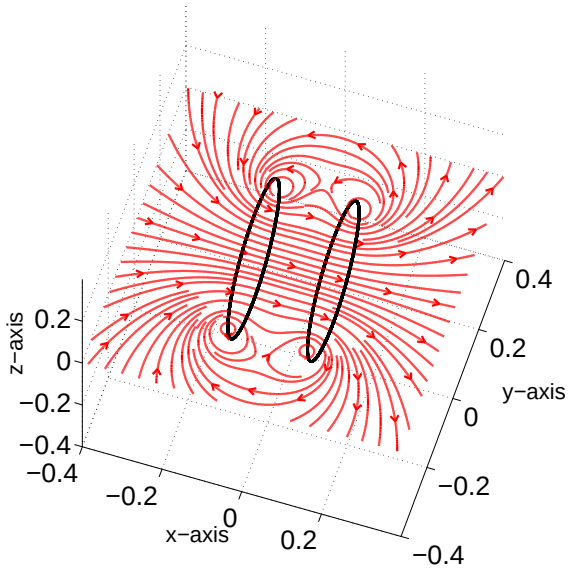

FIGURE A.5: Magnetic field projection provided by the two coils.

A.3 Simulating the effect of an angular error of one coil on the uniformity of the magnetic field of two coil combinations.

The results of this part indicate the impact of the angular error between two coils on the uniformity of the magnetic field. Unfortunately, as stated earlier, this error is common for three-axis Helmholtz coil.

In the case of calibration of magnetometers with three-axis Helmholtz coil, the calibration parameters may deviate from the real value caused by this type of error. Moreover, as a result of this effect, the advantage of using the Helmholtz coil to provide the uniform region of the magnetic field may be reduced a lot. To give an example (see Figure A.7), assume the Helmholtz coil has a radius of $10cm$ and an angular error of 45° between the paired coils (which is certainly a strong exaggeration, and is chosen only to provide a better view of the results). Figure A.6 depicts our simulation results corresponding to this configuration in MATLAB.

Here, the blue vectors represent the magnetic field produced by the Helmholtz coil in a region of $4cm^2$ when the paired coils are perfectly parallel and the red vectors represent that with 45° deviation. Due to this result, it is necessary to point out two

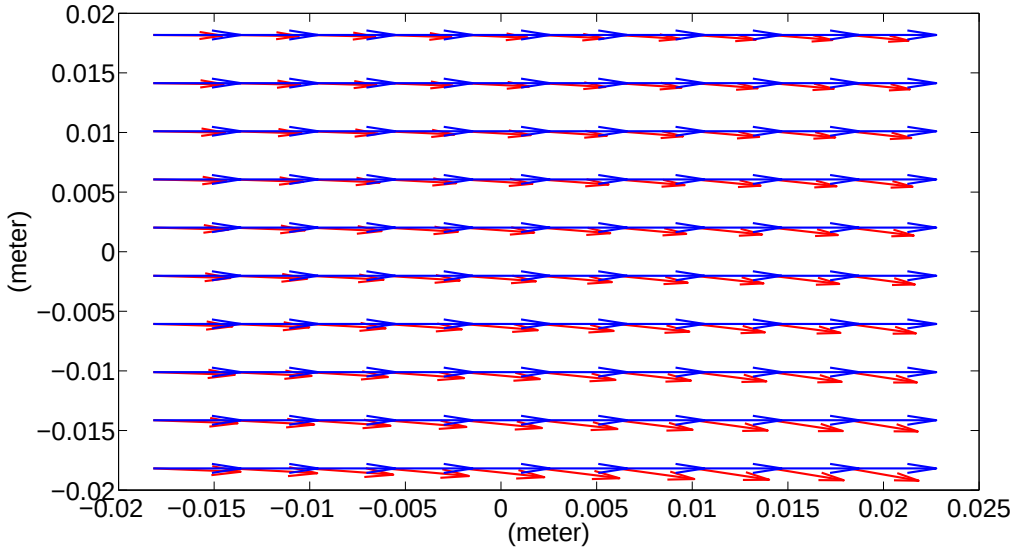

FIGURE A.6: Magnetic field deviation at the center of the Helmholtz coil ($2cm \times 2cm$).

important aspects regarding the aforementioned region that we need to calibrate the magnetometers. First, the direction of the magnetic fields changes as well as their magnitude. Second, this deviation is not identical for all parts of the region. In other words, the non-uniformity of the magnetic field can not be compensated completely by using another pair of coils of the three axis Helmholtz coil to produce an orthogonal field.

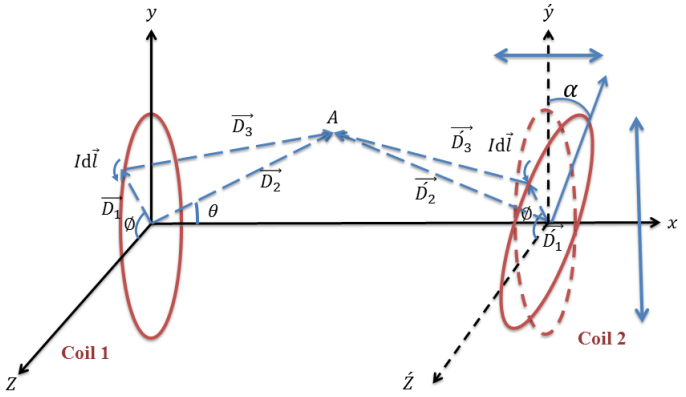

FIGURE A.7: Calculating the magnetic field combination at point A with α angular error.

Being aware of this limitation, we need to verify the uniformity of the magnetic field and its relation by the size of the Helmholtz coil. To achieve this aim, first the equations have to be changed accordingly. Hence, as depicted in Figure A.7 one of the coil bodies

needs to be rotated by an angle α around the z-axis. Now, considering Figure A.4, we can write:

$$\overrightarrow{D_2'} = \overrightarrow{D_5} = (x_1 - x_0).\overrightarrow{i} + y_0.\overrightarrow{j}$$

then, $\overrightarrow{D_1'}$ has to be rotated based on the vector rotation method. This vector is defined by $\overrightarrow{D_1''}$

$$\overrightarrow{D_1''} = R(\alpha)\overrightarrow{D_1'}$$

where $R(\alpha)$ is defined by

$$R(\alpha) = \begin{bmatrix} cos(\alpha) & sin(\alpha) & 0 \\ -sin(\alpha) & cos(\alpha) & 0 \\ 0 & 0 & 1 \end{bmatrix}$$

Consequently

$$\overrightarrow{D_1''} = Rsin(\phi)sin(\alpha)\overrightarrow{i} + Rsin(\phi)cos(\alpha)\overrightarrow{j} + Rcos(\phi)\overrightarrow{k} \tag{A.6}$$

and

$$\overrightarrow{D_3'} = \overrightarrow{D_2'} - \overrightarrow{D_1''}$$

Similarly, the computation can be accomplished following the previous process. Figure A.8 represents the projection of the magnetic field when an angular error of 45° exists between the paired coils.

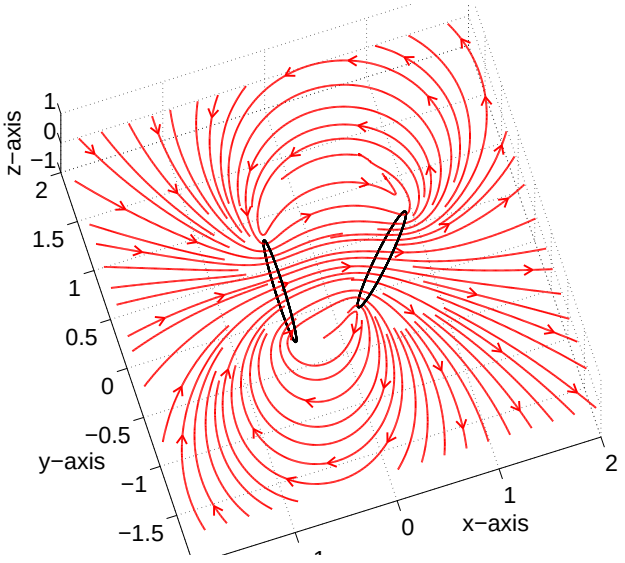

FIGURE A.8: Projection of magnetic field of two coils combination with 45 degree deviation.

Given the above, we can now verify the effect of the typical angular error of the Helmholtz coil in the region that required for calibration the magnetometer. Furthermore, we can

characterize the Helmholtz coil size based on the estimated geometry errors that are commonly given by the manufacturer. As a result, Figure A.9 shows the map of the magnetic field that is confined to the region of $2cm$ by $2cm$ with the different angular error in the center of the Helmholtz coil. Moreover, Figure A.10 also shows the uniformity of the magnetic field with 1° angular error but for the different diameter sizes.

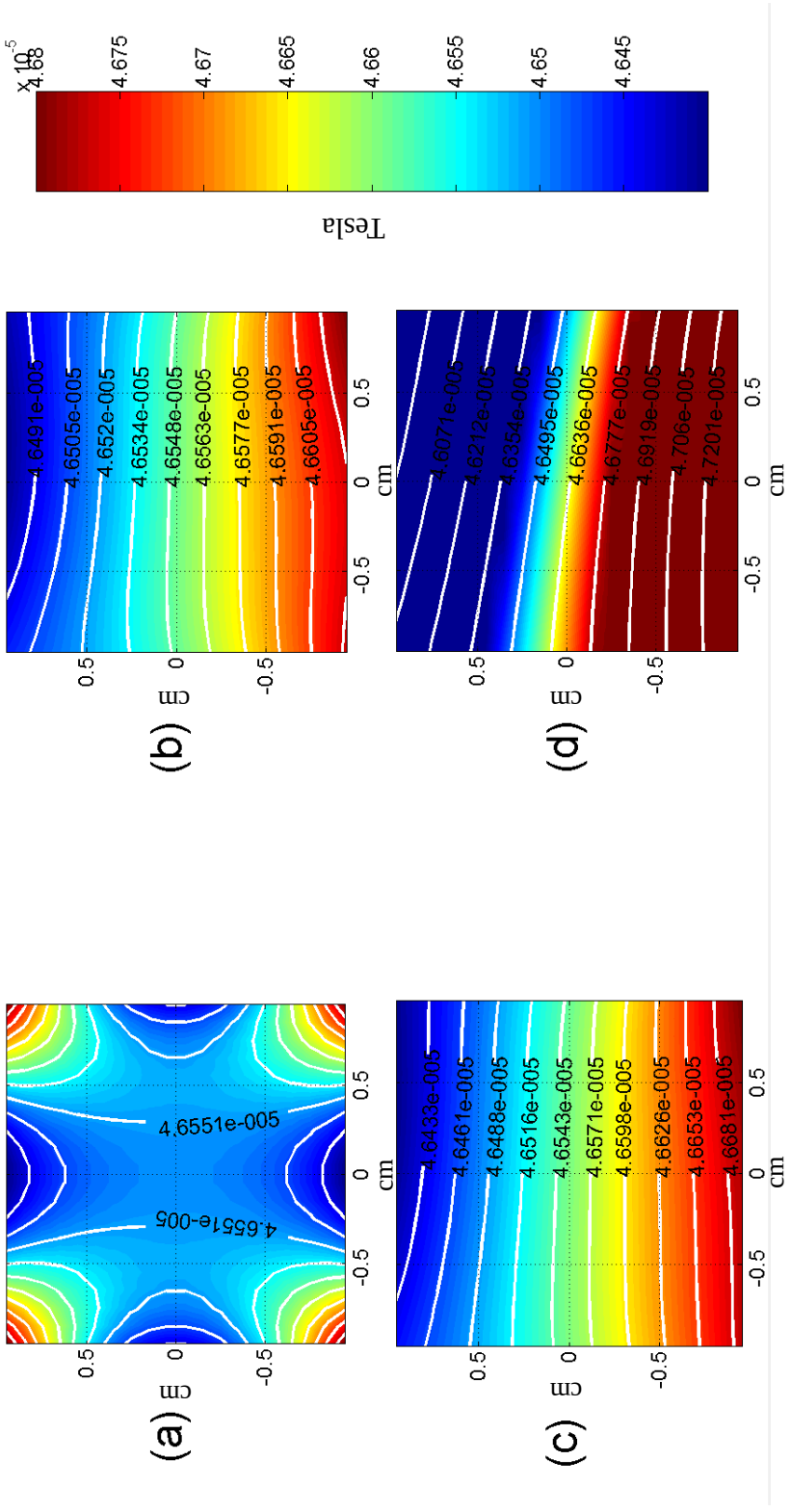

FIGURE A.9: Two-dimensional map of the magnetic field in a region of 2cm by 2cm in the center of the Helmholtz coil with different angular error. The magnetic field is given in Tesla units and the Helmholtz coil has a radius of 10 cm. (a) zero degree error, (b) 0.5 degree error, (c) 1 degree and (d) 10 degree error.

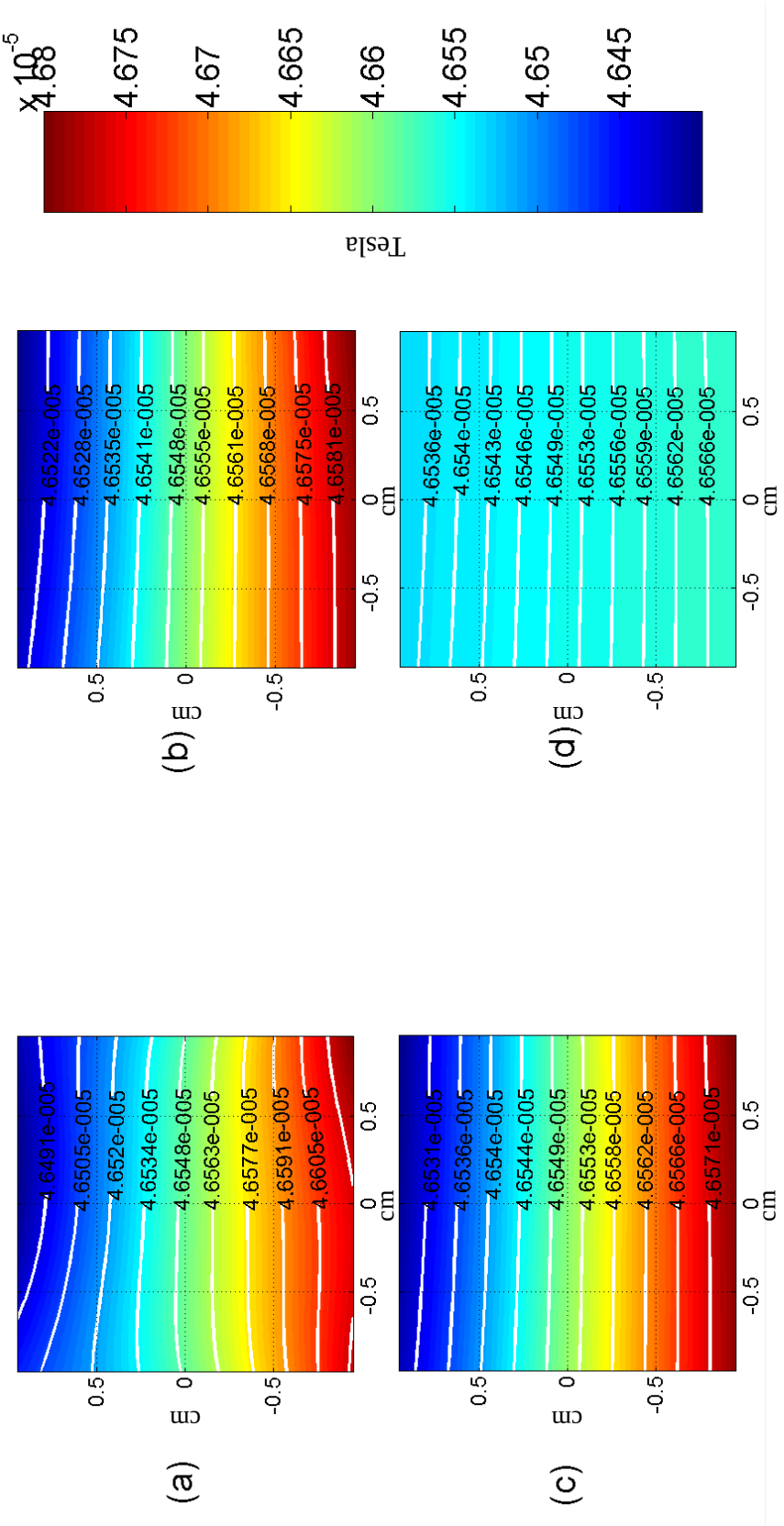

FIGURE A.10: Same as Figure A.9 with one degree angular error but different coil size. (a) 10cm, (b) 20cm, (c) 30cm and (d) 40cm.

Appendix B

Mu-metal box

In this part, we focus our attention on finding the optimal shape and size of the mu - metal box based on simulation results. Magnetic shielding and the difficulties with it have been discussed since the 19th century. In general, a closed structure of the high permeability materials is used to create a magnetically isolated region from the environmental magnetic field. These special materials work as a barrier to attenuate the external magnetic field by attracting the magnetic field lines to their surface. Then, the ratio of the magnetic field straight outside the shielding area compared to that in the shield area is the so called attenuation or shielding factor.
The shielding factor depends on several parameters such as the permeability of the materials, the thickness of the material, and the shielding diameter. In addition, the permeability itself also depends on shield geometry, material composition and the intensity of the external magnetic field [97]. Using a multi-layer shielding structure helps a great deal in obtaining a desirable shielding factor for precision measurement [98][99]. For an open-ended cylindrical magnetic shield extensive work has been done by I. Sasada, E. Paperno and co-workers in [100][101][102][103][104]. However, there is no simple and unique equation to calculate the shielding factor achieved by the different shape multi-layer shielding box. In general, these equations consist of unknown parameters that should be verified before any calculation due to the aforementioned effects. Note that here we do not take into account remanence or remanent magnetization which might change the shielding factor of the mu-metal box [105]. In this case, if the mu-metal material is subjected to a large magnetic field, the magnetization left behind in a material after removing the external field is called remanence or remanent magnetization. However, in our case we can assume that the mu-metal box is always fixed in the Earth's magnetic field. Moreover, the field that is provided by the Helmholtz coil inside the mu-metal box is also a kind of sinusoidal. Considering these two points, we can expect that the shielding factor will not be changed by the remanence magnetization.

In 1916, E. Wilson and J.W. Nicholson reported the way to calculate the shielding factor of a multi-layer spherical shield area [106]. After that in 1935, T. E Sterne presented a similar method but for computing the exact attenuation factor of multi-layer cylinders by considering n coaxial cylinders placed in a uniform magnetic field [107]. However, the proposed equation has a recursion relation of many different parts to calculate the exact value of attenuation ration, but he also presented a simple form of equation by assuming that μ (material permeability) is large when the thickness of high permeability material is much smaller than the diameter of the shielding box.
In order to calculate the attenuation factor, we follow what he discussed in his paper. First, assume a multi-layer cylinder as shown in Figure B.1. Then, the first set of pa-

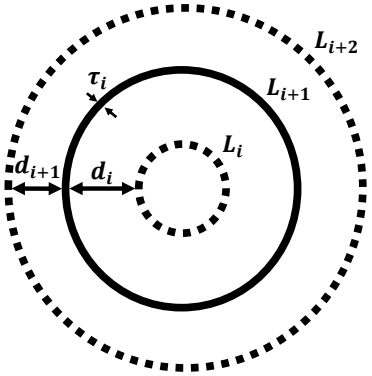

FIGURE B.1: Schema of n layers cylinder magnetic shield. For each shell, i, τ and d represent the number of layers, thickness and the distance between the shells respectively.

rameters is calculated as follows, where τ is the thickness of each layer, d is the distance between the layers and b is the external radius of each layer.

$$\begin{cases} \epsilon_i = \frac{\tau_i}{b_i}\left(1 - \frac{\tau_i}{2b_i}\right) \\ \epsilon_{i,i+1} = \frac{d_i}{(b_i + d_{i+1})}\left(1 - \frac{d_i}{2(b_i + d_{i+1})}\right) \end{cases} \tag{B.1}$$

After that, the second set of parameters can be calculated from the previous equations and the known values of μ as follows:

$$\begin{cases} \alpha_i = 1 - \epsilon_i - \epsilon_{i,i+1} + \mu\epsilon_i\epsilon_{i,i+1} \\ \beta_i = \epsilon_{i,i+1} \\ \gamma_i = \mu\epsilon_i \\ \delta_i = 1 - \epsilon_i - \epsilon_{i,i+1} \end{cases} \tag{B.2}$$

The next step allocated to computing the following equation by considering an initial value for u_1 and v_1. $(u_1 = v_1 = 1)$.

$$\begin{cases} u_{i+1} = \alpha_i u_i + \beta_i v_i \\ v_{i+1} = \gamma_i u_i + \delta_i v_i \end{cases} \tag{B.3}$$

Finally, the attenuation factor that is defined by F will be calculated as follows:

$$F = \frac{1}{2}(u_{n+1} + v_{n+1}) \tag{B.4}$$

B.1 Shape

Using the spherical shields provides a better performance due to their symmetric shape and the effect of external magnetic fields on their surfaces.
The exact attenuation factor of the spherical shell can be calculated by the simple equation [108].

$$S = \frac{1}{9\mu}\left[(2\mu+1)(\mu+2) - 2\frac{\nu}{V}(\mu-1)^2\right] \tag{B.5}$$

Where ν is the volume contained by the inner surface and V is that for the outer surface. μ is the permeability of the material.
However, this geometry shape is hard to fabricate, especially when we deal with multi-layered spherical shells. Usually, the most practical geometric shape would be a cylinder. In Figure B.2, we present the simulation results of four layers cylindrical geometry. The diagonal of the inner circle is the same as the side length of the previous simulation results in Figure 6.10. Moreover, both structures have the same material thickness and the same distance between the shielding layers.
This result highlights the fact that the attenuation factor of this geometric shape can be improved by a factor of 3 compared to that in Figure 6.10.
In addition, the other aspect to point out is that the uniformity of the magnetic field inside the shielded area will be ameliorated as well. According to obtained results (see Figure B.3), the variation of the magnetic field inside the box is reduced to around 10pT.

B.2 Size

It is important to add that the ratio of material thickness to the radius of the cylinder plays an important role to improve the attenuation factor. According to the equations described earlier, the increment of the material thickness leads to an improvement of the attenuation factor as well as the decline of the radius of the layer. From these facts,

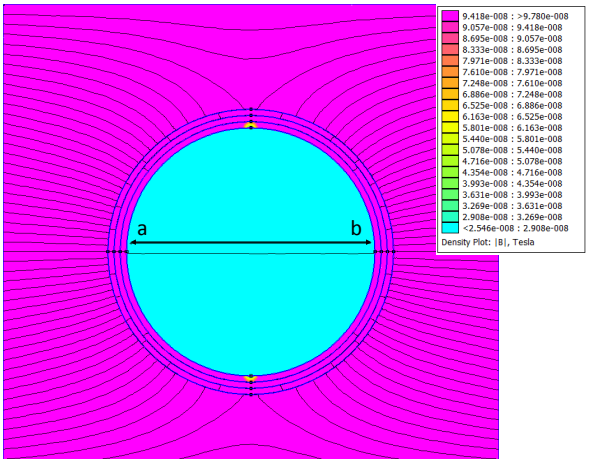

FIGURE B.2: The distortion of the Earth's magnetic field lines near a high permeability ($\mu = 11000$) four-layer cylindrical magnetic shield set. The radius of the inner shell is 20cm, the thickness of the high permeability material is 1mm and the distance between the layers is 10mm.

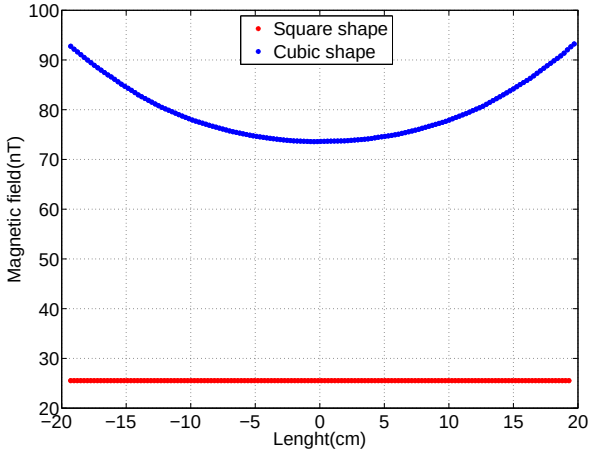

FIGURE B.3: Comparison of the cubical geometry with the cylindrical geometry both for the magnitude and uniformity of the magnetic field between points a and b in Figure B.2.

one may conclude that choosing the appropriate size of magnetic shields due to the requirement area helps great deal in cost saving and fabrication difficulties.

To give an example, consider a geometric shape as presented in Figure B.2, but two times smaller. However, we keep the same material thickness (1mm) and the space (1cm) between the layers based on Equation (B.4). Table B.1 illustrates the calculated parameters for each attenuation factor. It would also be interesting to refer to Figure B.4, which shows the attenuation factor as a function of inner radius size.

	Radius = 20cm			Radius = 10cm		
Layer	u_i	v_i	F_i	u_i	v_i	F_i
1	3.5453	0.0558*e3	0.0297*e3	0.0105*e3	0.011*e3	0.06*e3
2	14.0799	0.2383*e3	0.1262*e3	0.1017*e3	0.1145*e3	0.623*e3
3	53.4292	0.9295*e3	0.4915*e3	0.865*e3	1.0338*e3	5.602*e3
4	192.967	3.4373*e3	1.8151*e3	6.5327*e3	8.2457*e3	44.95*e3

TABLE B.1: Numerical computation of attenuation factor for four layers cylindrical shape with different radius.

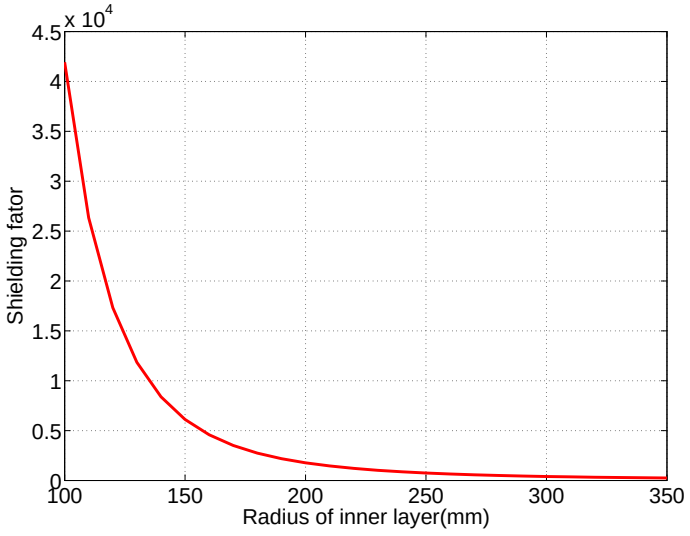

FIGURE B.4: Shielding factor of four-layer cylindrical magnetic shield as a function of the radius of the inner layer. $\mu = 11000$, thickness = 1mm, the space between the layers = 10mm.

B.3 Distance between the layers

Using more space between the shielding layers is an other way to increase the attenuation factor. In this case, each layer separately provides better shielding performances as a consequence of the larger space between the layers. Figure B.5, shows the numerical computation of the magnetic field distribution inside the shielded area when they have a similar radius for inner layer and thickness. Nevertheless, for the magnetic shield that is shown on the left, the layers are separated by 30mm while the right one has 10mm spacing between the layers. The effect of larger spacing has apparently appeared between the two first inner layers.

The functionality of the shielding factor with the different distances between the layers is depicted in Figure B.6. This result demonstrates almost linear behavior for 4 layers of cylindrical geometry with a range of distances between 1mm and 5cm.

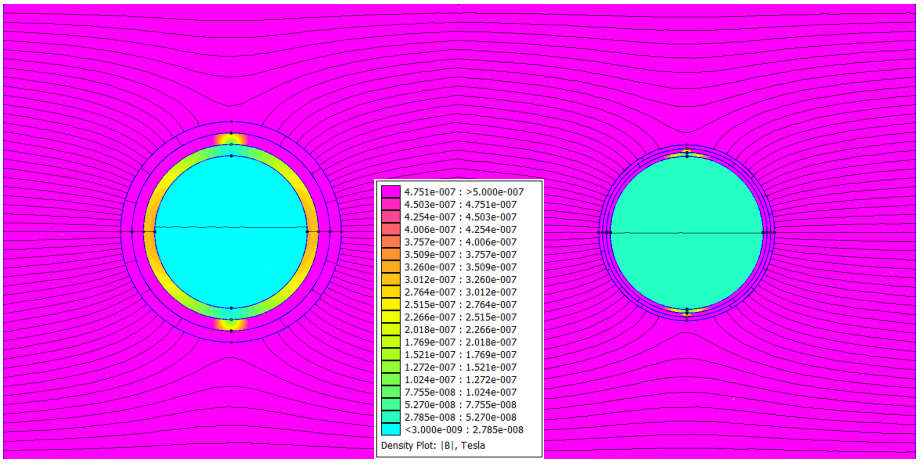

FIGURE B.5: Evaluation of residual of the Earth's magnetic field among the layers. Both magnetic shields consist of four layers and the inner layer of each has the same radius. However, for the left shape, the layers are separated by 30mm and for the right shape the layers are separated by 10mm ($\mu = 11000$, thickness = 1mm).

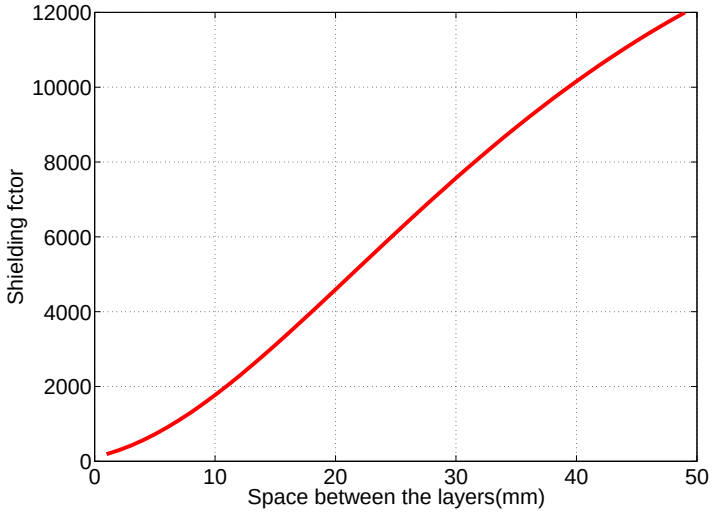

FIGURE B.6: Attenuation factor as a function of the distance between the layers.

B.4 Number of layers

Adding more layers improves the shielding performance where there is a limitation to reduce the geometrical size. Although, it will increase the fabrication cost as well. Figure B.7 compares the simulation results for the aforementioned geometrical size in Figure B.2 with different numbers of layers and material thickness.

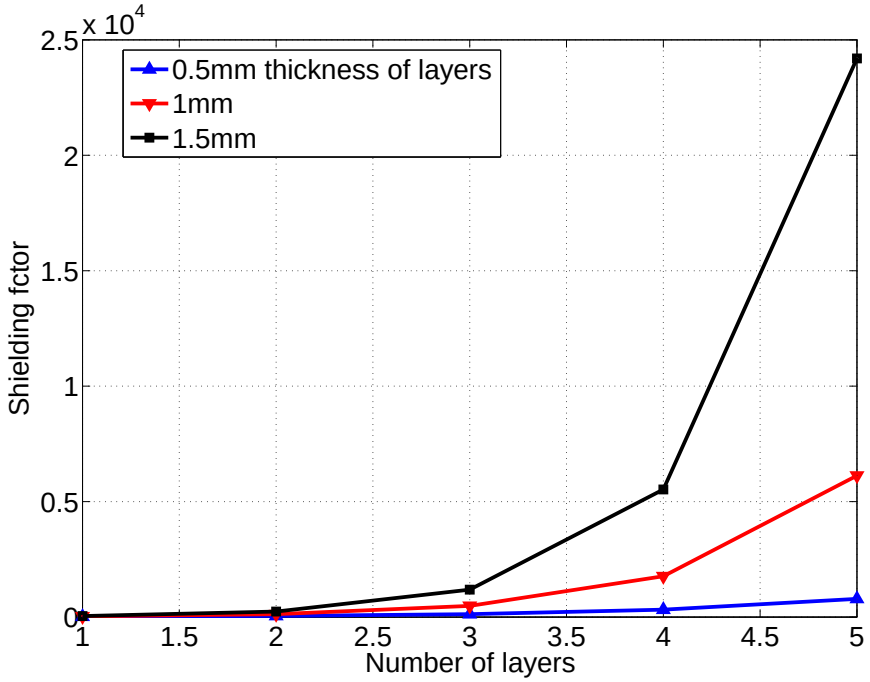

FIGURE B.7: Attenuation factor as a function of thickness and number of layers. ($\mu = 11000$, spacing between layers = 1cm)

Bibliography

[1] Joseph Needham. *Science and Civilisation in China: Sections 8-18.-History of Scientific Thought*. Cambridge University Press, 1962.

[2] Ronald T Merrill, Michael W McElhinny, and Phillip L McFadden. *Magnetic Field of the Earth*, volume 63. Academic Press, 1996.

[3] Matthew R Walker and Andrew Jackson. Robust modelling of the earth's magnetic field. *Geophysical Journal International*, 143(3):799–808, 2000.

[4] Harold W.; Karsky Dick Jasumback, Anthony E.; Thistle. Two decades of development and evaluation of gps technology for natural resource applications: Missoula technology and development center. 1999.

[5] Alonzo Kelly. Modern inertial and satellite navigation systems. Technical report, DTIC Document, 1994.

[6] David Titterton and John Weston. Strapdown inertial navigation technology. 2-nd edition. *The Institution of Electronical Engineers, Reston USA*, 2004.

[7] Oliver J Woodman. An introduction to inertial navigation. *University of Cambridge, Computer Laboratory, Tech. Rep. UCAMCL-TR-696*, 2007.

[8] David Vissiere, Alain Pierre Martin, Nicolas Petit, et al. Using magnetic disturbances to improve imu-based position estimation. In *Proceedings of the European Control Conference 2007*, pages 2853–2858, 2007.

[9] Eric Dorveaux. *Magneto-Inertial Navigation Principles and application to an indoor pedometer*. PhD thesis, École Nationale Supérieure des Mines de Paris, 2011.

[10] Nicolas Praly, Nicolas Petit, Julien Laurent-Varin, et al. Using distributed magnetometry in navigation of heavy launchers and space vehicles. In *4TH EUROPEAN CONFERENCE FOR AEROSPACE SCIENCES (EUCASS)*, 2011.

[11] James E Lenz. A review of magnetic sensors. *Proceedings of the IEEE*, 78(6): 973–989, 1990.

[12] Richard Boll and Kenneth J Overshott. *Sensors, Magnetic Sensors*, volume 5. Wiley-VCH, 2008.

[13] Pavel Ripka et al. *Magnetic sensors and magnetometers*, volume 8. Artech house Boston, 2001.

[14] Slawomir Tumanski. *Thin film magnetoresistive sensors*. Taylor & Francis, 2010.

[15] Isaak D Mayergoyz and Göran Engdahl. *Handbook of giant magnetostrictive materials*. Academic Press, 1999.

[16] L_V Panina, K Mohri, K Bushida, and M Noda. Giant magneto-impedance and magneto-inductive effects in amorphous alloys. *Journal of Applied Physics*, 76(10): 6198–6203, 1994.

[17] Manh-Huong Phan and Hua-Xin Peng. Giant magnetoimpedance materials: Fundamentals and applications. *Progress in Materials Science*, 53(2):323–420, 2008.

[18] Radivoje S Popović. *Hall effect devices*. Taylor & Francis, 2004.

[19] Paul Leroy, Christophe Coillot, Alain F Roux, and Gérard M Chanteur. High magnetic field amplification for improving the sensitivity of hall sensors. *Sensors Journal, IEEE*, 6(3):707–713, 2006.

[20] P. Coillot, C. Leroy. Induction magnetometers principle, modeling and ways of improvement.

[21] Pavel Ripka. Advances in fluxgate sensors. *Sensors and Actuators A: Physical*, 106(1):8–14, 2003.

[22] Mario Norberto Baibich, JM Broto, Albert Fert, F Nguyen Van Dau, F Petroff, P Etienne, G Creuzet, A Friederich, and J Chazelas. Giant magnetoresistance of (001) fe/(001) cr magnetic superlattices. *Physical Review Letters*, 61(21):2472, 1988.

[23] Seok Soo Yoon, Pratap Kollu, Dong Young Kim, Gun Woo Kim, Yongjun Cha, and CheolGi Kim. Magnetic sensor system using asymmetric giant magnetoimpedance head. *Magnetics, IEEE Transactions on*, 45(6):2727–2729, 2009.

[24] J Moutoussamy, C Coillot, G Chanteur, and F Alves. Various coiled magnetoimpedance based on differential magnetic permeability variation. *Sensor Letters*, 11(1):40–43, 2013.

[25] Ce-Wen Nan, MI Bichurin, Shuxiang Dong, D Viehland, and G Srinivasan. Multiferroic magnetoelectric composites: Historical perspective, status, and future directions. *Journal of Applied Physics*, 103(3):031101–031101, 2008.

[26] Junyi Zhai, Zengping Xing, Shuxiang Dong, Jiefang Li, and D Viehland. Detection of pico-tesla magnetic fields using magneto-electric sensors at room temperature. *Applied physics letters*, 88(6):062510–062510, 2006.

[27] Robert Racz, Christian Schott, and Samuel Huber. Electronic compass sensor. In *Sensors, 2004. Proceedings of IEEE*, pages 1446–1449. IEEE, 2004.

[28] James E Lenz. A review of magnetic sensors. *Proceedings of the IEEE*, 78(6): 973–989, 1990.

[29] J Čižmár. Magnetic correction of aircraft navigation instruments.

[30] Jorge Lobo, Paulo Lucas, Jorge Dias, and A Traca de Almeida. Inertial navigation system for mobile land vehicles. In *Industrial Electronics, 1995. ISIE'95., Proceedings of the IEEE International Symposium on*, volume 2, pages 843–848. IEEE, 1995.

[31] Mario H Acuña. Space-based magnetometers. *Review of scientific instruments*, 73 (11):3717–3736, 2002.

[32] Hae-Seok Park, Jun-Sik Hwang, Won-Youl Choi, Dong-Sik Shim, Kyoung-Won Na, and Sang-On Choi. Development of micro-fluxgate sensors with electroplated magnetic cores for electronic compass. *Sensors and Actuators A: Physical*, 114(2): 224–229, 2004.

[33] Laurent Chiesi, Pavel Kejik, Balazs Janossy, and RS Popovic. Cmos planar 2d micro-fluxgate sensor. *Sensors and Actuators A: Physical*, 82(1):174–180, 2000.

[34] HC Seran and P Fergeau. An optimized low-frequency three-axis search coil magnetometer for space research. *Review of scientific instruments*, 76(4):044502–044502, 2005.

[35] A Roux, Olivier Le Contel, Christophe Coillot, Abdel Bouabdellah, Bertrand De La Porte, Dominique Alison, Sébastien Ruocco, and Marie-Cécile Vassal. The search coil magnetometer for themis. *Space Science Reviews*, 141(1-4):265–275, 2008.

[36] David A Robinson. A method of measuring eye movemnent using a scieral search coil in a magnetic field. *Bio-medical Electronics, IEEE Transactions on*, 10(4): 137–145, 1963.

[37] Ronald S Remmel. An inexpensive eye movement monitor using the scleral search coil technique. *Biomedical Engineering, IEEE Transactions on*, (4):388–390, 1984.

[38] Tianxiang Nan, Yu Hui, Matteo Rinaldi, and Nian X Sun. Self-biased 215mhz magnetoelectric nems resonator for ultra-sensitive dc magnetic field detection. *Scientific reports*, 3, 2013.

[39] G Srinivasan, ET Rasmussen, J Gallegos, R Srinivasan, Yu I Bokhan, and VM Laletin. Magnetoelectric bilayer and multilayer structures of magnetostrictive and piezoelectric oxides. *Physical Review B*, 64(21):214408, 2001.

[40] Shuxiang Dong, Junyi Zhai, Zhengping Xing, Jie-Fang Li, and D Viehland. Extremely low frequency response of magnetoelectric multilayer composites. *Applied Physics Letters*, 86(10):102901–102901, 2005.

[41] Pavel Ripka and Michal Janosek. Advances in magnetic field sensors. *Sensors Journal, IEEE*, 10(6):1108–1116, 2010.

[42] Jiang Yanwei, Fang Jiancheng, Huang Xuegong, and Song Yujun. Design of gmi micro-magnetic sensor and its application for geomagnetic navigation. In *Systems and Control in Aerospace and Astronautics, 2008. ISSCAA 2008. 2nd International Symposium on*, pages 1–6. IEEE, 2008.

[43] GV Kurlyandskaya, ML Sanchez, B Hernando, VM Prida, P Gorria, and M Tejedor. Giant-magnetoimpedance-based sensitive element as a model for biosensors. *Applied physics letters*, 82(18):3053–3055, 2003.

[44] Galina V Kurlyandskaya and Vanessa Fal Miyar. Surface modified amorphous ribbon based magnetoimpedance biosensor. *Biosensors and Bioelectronics*, 22(9): 2341–2345, 2007.

[45] K-MH Lenssen, HW Van Kesteren, Th GSM Rijks, JCS Kools, MC de Nooijer, R Coehoorn, and W Folkerts. Giant magnetoresistance and its application in recording heads. *Sensors and Actuators A: Physical*, 60(1):90–97, 1997.

[46] MD Michelena, W Oelschlagel, I Arruego, RP Del Real, JAD Mateos, and JM Merayo. Magnetic giant magnetoresistance commercial off the shelf for space applications. *Journal of Applied Physics*, 103(7):07E912–07E912, 2008.

[47] www.nve.com.

[48] Giant room-temperature magnetoresistance in single-crystal fe/mgo/fe magnetic tunnel junctions, author=Yuasa, Shinji and Nagahama, Taro and Fukushima, Akio and Suzuki, Yoshishige and Ando, Koji, journal=Nature materials, volume=3, number=12, pages=868–871, year=2004, publisher=Nature Publishing Group. .

[49] Stuart SP Parkin, Christian Kaiser, Alex Panchula, Philip M Rice, Brian Hughes, Mahesh Samant, and See-Hun Yang. Giant tunnelling magnetoresistance at room temperature with mgo (100) tunnel barriers. *Nature materials*, 3(12):862–867, 2004.

[50] Hiroshi Yamazaki, Hiraku Hirabayashi, Nobuya Oyama, and Masanori Sakai. B8. 4-characterisitics of tmr angle sensors. *Proceedings SENSOR 2011*, pages 361–365, 2011.

[51] http://www.nve.com/2009prs/mar312009-aat.htm. .

[52] Ruy Sanz, Ana B Fernández, Jose A Dominguez, Boris Martín, and Marina D Michelena. Gamma irradiation of magnetoresistive sensors for planetary exploration. *Sensors*, 12(4):4447–4465, 2012.

[53] Edmund C Stoner and EP Wohlfarth. A mechanism of magnetic hysteresis in heterogeneous alloys. *Philosophical Transactions of the Royal Society of London. Series A. Mathematical and Physical Sciences*, pages 599–642, 1948.

[54] DISCRETE SEMICONDUCTORS. Magnetic field sensors. *Philips Semiconductors, SC17*, 20, 1998.

[55] I Mateos, M Diaz-Aguiló, F Gibert, I Lloro, A Lobo, M Nofrarias, and J Ramos-Castro. Temperature coefficient improvement for low noise magnetic measurements in lisa. In *Journal of Physics: Conference Series*, volume 363, page 012051. IOP Publishing, 2012.

[56] DF He, M Tachiki, and H Itozaki. Highly sensitive anisotropic magnetoresistance magnetometer for eddy-current nondestructive evaluation. *Review of Scientific Instruments*, 80(3):036102–036102, 2009.

[57] Cross axis effect for amr magnetic sensor, honeywell application note (an-215). *www.magneticsensors.com*, .

[58] JHJ Fluitman. The influence of sample geometry on the magnetoresistance of ni-fe films. *Thin Solid Films*, 16(3):269–276, 1973.

[59] George S Ahnasi. Magnetoresistpye sensing device for de-tection of magnetic fields having a shape anisotropy field and uniaxial anisotropy field which are perpendicular, February 13 1973. US Patent 3,716,781.

[60] Set/reset function for magnetic sensors. *www.magneticsensors.com*, .

[61] Set/reset pulse circuits for magnetic sensors. *www.magneticsensors.com*, .

[62] Mike Caruso. Set/reset pulse circuits for hmc1021/22. *www.magneticsensors.com*.

[63] Jannik Hammel Nielsen and Erik Bruun. A cmos low-noise instrumentation amplifier using chopper modulation. *Analog Integrated Circuits and Signal Processing*, 42(1):65–76, 2004.

[64] Egon Zimmermann, Arre Verweerd, Walter Glaas, Axel Tillmann, and Andreas Kemna. An amr sensor-based measurement system for magnetoelectrical resistivity tomography. *Sensors Journal, IEEE*, 5(2):233–241, 2005.

[65] Zhitian Wu, Yuanxin Wu, Xiaoping Hu, and Meiping Wu. Calibration of three-axis strapdown magnetometers using particle swarm optimization algorithm. In *Robotic and Sensors Environments (ROSE), 2011 IEEE International Symposium on*, pages 160–165. IEEE, 2011.

[66] Xiaoming Zhang and Lizhen Gao. A novel auto-calibration method of the vector magnetometer. In *Electronic Measurement & Instruments, 2009. ICEMI'09. 9th International Conference on*, pages 1–145. IEEE, 2009.

[67] Demoz Gebre-Egziabher, GH Elkaim, J David Powell, and BW Parkinson. A non-linear, two-step estimation algorithm for calibrating solid-state strapdown magnetometers. In *8th International St. Petersburg Conference on Navigation Systems (IEEE/AIAA)*, 2001.

[68] Eunghyun Kim and Hyo-Choong Bang. Bias estimation of magnetometer using genetic algorithm. In *Control, Automation and Systems, 2007. ICCAS'07. International Conference on*, pages 195–198. IEEE, 2007.

[69] John L Crassidis, Kok-Lam Lai, and Richard R Harman. Real-time attitude-independent three-axis magnetometer calibration. *Journal of Guidance, Control, and Dynamics*, 28(1):115–120, 2005.

[70] AL Bloom, DJ Innes, RC Rempel, and KA Ruddock. Octagonal coil systems for canceling the earth's magnetic field. *Journal of Applied Physics*, 36(8):2560–2565, 1965.

[71] LR Newitt, M Mandea, LA McKee, and J-J Orgeval. Recent acceleration of the north magnetic pole linked to magnetic jerks. *Eos, Transactions American Geophysical Union*, 83(35):381–389, 2002.

[72] Qingde Li and John G Griffiths. Least squares ellipsoid specific fitting. In *Geometric Modeling and Processing, 2004. Proceedings*, pages 335–340. IEEE, 2004.

[73] Eric Dorveaux, David Vissière, A-P Martin, and Nicolas Petit. Iterative calibration method for inertial and magnetic sensors. In *Decision and Control, 2009 held*

jointly with the 2009 28th Chinese Control Conference. CDC/CCC 2009. Proceedings of the 48th IEEE Conference on, pages 8296–8303. IEEE, 2009.

[74] J Včelák, P Ripka, A Platil, J Kubik, and P Kašpar. Errors of amr compass and methods of their compensation. *Sensors and Actuators A: Physical*, 129(1):53–57, 2006.

[75] Pavel Ripka, Michal Janosek, and Mattia Butta. Crossfield sensitivity in amr sensors. *Magnetics, IEEE Transactions on*, 45(10):4514–4517, 2009.

[76] Jun Ouyang, Shi Chen, Lei Yu, Chao Zuo, Xinguo Chen, Shaobing Wu, and Xiaofei Yang. Compensation method of cross-axis effect for amr sensor. In *Electrical and Control Engineering (ICECE), 2010 International Conference on*, pages 603–606. IEEE, 2010.

[77] B Bharat and Mike Caruso. Magnetic sensor cross-axis effect, honeywell application note (an-205). *www.magneticsensors.com*.

[78] Kaveh Mohamadabadi, Christophe Coillot, and Mathieu Hillion. New compensation method for cross-axis effect for three-axis amr sensors. 2013.

[79] 1-and 2-axis magnetic sensors (hmc1001/1002/1021/1022). *www.magneticsensors.com*.

[80] Vojtech Petrucha, Petr Kaspar, Pavel Ripka, and Jose MG Merayo. Automated system for the calibration of magnetometers. *Journal of Applied Physics*, 105(7): 07E704–07E704, 2009.

[81] J Včelák, P Ripka, J Kubik, A Platil, and P Kašpar. Amr navigation systems and methods of their calibration. *Sensors and Actuators A: Physical*, 123:122–128, 2005.

[82] Lei Yu, Shi Chen, Jun Ouyang, Chao Zuo, Xinguo Chen, Shaobin Wu, and Xiaofei Yang. Error compensation and implementation of embedded high-precision. In *Electrical and Control Engineering (ICECE), 2010 International Conference on*, pages 911–914. IEEE, 2010.

[83] Wenguang Feng, Shibin Liu, Shiwei Liu, and Shanglin Yang. A calibration method of three-axis magnetic sensor based on ellipsoid fitting.

[84] RK Cacak and JR Craig. Magnetic field uniformity around near-helmholtz coil configurations. *Review of Scientific Instruments*, 40(11):1468–1470, 1969.

[85] Jian Wang, Shouxian She, and Sijiong Zhang. An improved helmholtz coil and analysis of its magnetic field homogeneity. *Review of scientific instruments*, 73(5): 2175–2179, 2002.

[86] Yong H Ha, Byung H Han, and Soo Y Lee. Magnetic propulsion of a magnetic device using three square-helmholtz coils and a square-maxwell coil. *Medical & biological engineering & computing*, 48(2):139–145, 2010.

[87] Quanliang Cao, Xiaotao Han, Bo Zhang, and Liang Li. Analysis and optimal design of magnetic navigation system using helmholtz and maxwell coils. *Applied Superconductivity, IEEE Transactions on*, 22(3):4401504–4401504, 2012.

[88] 1 and 2 axis magnetic sensorshmc1001/hmc1002/hmc1021/hmc1022. 2003.

[89] P Brown, T Beek, C Carr, H OBrien, E Cupido, T Oddy, and TS Horbury. Magnetoresistive magnetometer for space science applications. *Measurement Science and Technology*, 23(2):025902, 2012.

[90] Werner Magnes and Marina Diaz-Michelena. Future directions for magnetic sensors for space applications. *Magnetics, IEEE Transactions on*, 45(10):4493–4498, 2009.

[91] Jian Wang, Shouxian She, and Sijiong Zhang. An improved helmholtz coil and analysis of its magnetic field homogeneity. *Review of scientific instruments*, 73(5): 2175–2179, 2002.

[92] Yong H Ha, Byung H Han, and Soo Y Lee. Magnetic propulsion of a magnetic device using three square-helmholtz coils and a square-maxwell coil. *Medical & biological engineering & computing*, 48(2):139–145, 2010.

[93] Edward R Javor and Theodore Anderson. Design of a helmholtz coil for low frequency magnetic field susceptibility testing. In *Electromagnetic Compatibility, 1998. 1998 IEEE International Symposium on*, volume 2, pages 912–917. IEEE, 1998.

[94] I Sasada and Y Nakashima. Planar coil system consisting of three coil pairs for producing a uniform magnetic field. *Journal of applied physics*, 99(8):08D904–08D904, 2006.

[95] RK Cacak and JR Craig. Magnetic field uniformity around near-helmholtz coil configurations. *Review of Scientific Instruments*, 40(11):1468–1470, 1969.

[96] Edwin L Bronaugh. Helmholtz coils for emi immunity testing: stretching the uniform field area. In *Electromagnetic Compatibility, 1990. Seventh International Conference on*, pages 169–172. IET, 1990.

[97] JF Hoburg. Principles of quasistatic magnetic shielding with cylindrical and spherical shields. *Electromagnetic Compatibility, IEEE Transactions on*, 37(4):574–579, 1995.

[98] M Hakan Oktem and Birsen Saka. Design of multilayered cylindrical shields using a genetic algorithm. *Electromagnetic Compatibility, IEEE Transactions on*, 43(2): 170–176, 2001.

[99] J Bork, HD Hahlbohm, R Klein, and A Schnabel. The 8-layered magnetically shielded room of the ptb: Design and construction. In *Biomag2000, Proc. 12th Int. Conf. on Biomagnetism*, pages 970–73. Espoo, Finland, 2001.

[100] Ichiro Sasada, Eugene Paperno, and Hiroyuki Koide. Design of a large-scale vertical open-structure cylindrical shield employing magnetic shaking. *Journal of Applied Physics*, 87(9):5962–5964, 2000.

[101] Eugene Paperno, Hiroyuki Koide, and Ichiro Sasada. A new estimation of the axial shielding factors for multishell cylindrical shields. *Journal of Applied Physics*, 87 (9):5959–5961, 2000.

[102] Eugene Paperno, Ichiro Sasada, and Kunihisa Tashiro. Experimental correction of the axial shielding equation. *Magnetics, IEEE Transactions on*, 38(5):3324–3326, 2002.

[103] E Paperno, I Sasada, and H Naka. Self-compensation of the residual field gradient in double-shell open-ended cylindrical axial magnetic shields. *Magnetics, IEEE Transactions on*, 35(5):3943–3945, 1999.

[104] K Oshita, I Sasada, H Naka, and E Paperno. Method for expanding the uniformly shielded area in a short-length open-ended cylindrical magnetic shield. *Journal of applied physics*, 85(8):4642–4644, 1999.

[105] A Mager. The berlin magnetically shielded room (bmsr), section a: design and construction. *Biomagnetism, Berlin: Walter de Gruyter*, pages 51–78, 1981.

[106] Ernest Wilson and JW Nicholson. On the magnetic shielding of large spaces, and its experimental measurement. *Proceedings of the Royal Society of London. Series A*, 92(644):529–549, 1916.

[107] TE Sterne. Multi-lamellar cylindrical magnetic shields. *Review of Scientific Instruments*, 6:324, 1935.

[108] Alan K Thomas. Magnetic shielded enclosure design in the dc and vlf region. *Electromagnetic Compatibility, IEEE Transactions on*, (1):142–152, 1968.